Large-scale Interseismic Strain Mapping of the NE Tibetan Plateau from Sentinel-1 Interferometry

Qi Ou[1], Simon Daout[2], Jonathan Weiss[3], Lin Shen[4], Milan Lazecky[4], Tim J. Wright[4], and Barry E. Parsons[5]

[1]Earth Sciences Department
[2]Department of Earth Sciences, University of Oxford
[3]NOAA/NWS Pacific Tsunami Warning Center
[4]University of Leeds
[5]University of Oxford

November 22, 2022

Abstract

The launches of the Sentinel-1 synthetic aperture radar satellites in 2014 and 2016 started a new era of high-resolution velocity and strain rate mapping for the continents. However, multiple challenges exist in tying independently processed velocity data sets to a common reference frame and producing high-resolution strain rate fields. We analyse Sentinel-1 data acquired between 2014 and 2019 over the northeast Tibetan Plateau, and develop new methods to derive east and vertical velocities with ˜100 m resolution and ˜1 mm/yr accuracy across an area of 440,000 km^2. By implementing a new method of combining horizontal gradients of filtered east and interpolated north velocities, we derive the first ˜1 km resolution strain rate field for this tectonically active region. The strain rate fields show concentrated shear strain along the Haiyuan and East Kunlun Faults, and local contractional strain on fault junctions, within the Qilianshan thrusts, and around the Longyangxia Reservoir. The Laohushan-Jingtai creeping section of the Haiyuan Fault is highlighted in our data set by extremely rapid strain rates. Strain across unknown portions of the Haiyuan Fault system, including shear on the eastern extension of the Dabanshan Fault and contraction at the western flank of the Quwushan, highlight unmapped tectonic structures. In addition to the uplift across most of the lowlands, the vertical velocities also contain climatic, hydrological or anthropogenic-related deformation signals. We demonstrate the enhanced view of large-scale active tectonic processes provided by high-resolution velocities and strain rates derived from Sentinel-1 data and highlight associated wide-ranging research applications.

Large-scale Interseismic Strain Mapping of the NE Tibetan Plateau from Sentinel-1 Interferometry

Q. Ou[1], S. Daout[1,4], J.R. Weiss[2,3,5], L. Shen[2], M. Lazecký[2], T.J. Wright[2], B.E. Parsons[1]

[1]COMET, Department of Earth Sciences, University of Oxford, South Parks Road, Oxford, United Kingdom
[2]COMET, School of Earth and Environment, University of Leeds, Leeds, , United Kingdom
[3]Institute of Geosciences, University of Potsdam, Karl-Liebknecht-Strasse 24, Potsdam, Germany

Key Points:

- We present new methods to mosaic line-of-sight velocity frames, derive Cartesian velocities, and produce high-resolution strain-rate maps.
- We construct 440,000 km^2 maps of east-west, vertical velocities, and strain rates over NE Tibet from Sentinel-1 interferometry.
- We quantify strain partitioning, measure creep rate, identify unmapped structures and climatic, hydrological and anthropogenic signals.

[4] now at Université de Lorraine - CNRS, UMR 7358, rue N. D. des Pauvres, 54501 Vandœuvre les Nancy, France
[5] now at NOAA/NWS Pacific Tsunami Warning Center, 1845 Wasp Boulevard, Honolulu, Hawaii, USA

Corresponding author: Qi Ou, `qi.ou@earth.ox.ac.uk`

Abstract

The launches of the Sentinel-1 synthetic aperture radar satellites in 2014 and 2016 started a new era of high-resolution velocity and strain rate mapping for the continents. However, multiple challenges exist in tying independently processed velocity data sets to a common reference frame and producing high-resolution strain rate fields. We analyse Sentinel-1 data acquired between 2014 and 2019 over the northeast Tibetan Plateau, and develop new methods to derive east and vertical velocities with ∼100 m resolution and ∼1 mm/yr accuracy across an area of 440,000 km^2. By implementing a new method of combining horizontal gradients of filtered east and interpolated north velocities, we derive the first ∼1 km resolution strain rate field for this tectonically active region. The strain rate fields show concentrated shear strain along the Haiyuan and East Kunlun Faults, and local contractional strain on fault junctions, within the Qilianshan thrusts, and around the Longyangxia Reservoir. The Laohushan-Jingtai creeping section of the Haiyuan Fault is highlighted in our data set by extremely rapid strain rates. Strain across unknown portions of the Haiyuan Fault system, including shear on the eastern extension of the Dabanshan Fault and contraction at the western flank of the Quwushan, highlight unmapped tectonic structures. In addition to the uplift across most of the lowlands, the vertical velocities also contain climatic, hydrological or anthropogenic-related deformation signals. We demonstrate the enhanced view of large-scale active tectonic processes provided by high-resolution velocities and strain rates derived from Sentinel-1 data and highlight associated wide-ranging research applications.

Plain Language Summary

The new-generation radar satellites permit the derivation of crustal velocities in fine resolution over continental scales. With the technical advancements developed in this study, we reveal unseen details of the crustal deformation over the earthquake-prone Hexi Corridor in the northeast corner of the Tibetan Plateau. In particular, we observe concentrated elastic loading along, and at branch points of, major earthquake-generating faults. The ability to monitor such phenomena is important for understanding future seismic hazard as such geometrical complexities along faults are often associated with earthquake triggering and termination. We also draw attention to previously unknown structures that are rapidly deforming. This new and enhanced view of the local tectonic setting could improve local seismic hazard assessment. Last but not least, we observe climatic, hydrological and anthropogenic signals in the vertical velocity field, which are related to permafrost thawing, blocked river drainage, mining, damming and the extraction of groundwater for farming. Overall, we demonstrate the wealth of information that can be derived from the rapidly growing space-born Earth observation data, which are destined to play an important role in shaping a more resilient world for the future.

1 Introduction

Over recent decades, Interferometric Synthetic Aperture Radar (InSAR) has emerged as a powerful geodetic tool for imaging crustal deformation on the continents (e.g. Burgmann et al., 2000; Elliott et al., 2016). Numerous studies have demonstrated InSAR's ability to reveal unknown faults (e.g. Wicks et al., 2013; Daout et al., 2019), highlight strain concentration (Weiss et al., 2020), identify creeping sections of faults (Cavalié et al., 2008; Jolivet et al., 2012; Rousset et al., 2016), and constrain slip parameters and frictional properties of faults (Jolivet et al., 2013, 2015; Zhou et al., 2018). This information is fundamental to seismic hazard assessment and understanding crustal dynamics.

The global coverage and the regular and frequent acquisition of SAR measurements provided by the Sentinel-1A and Sentinel-1B satellites, launched by the European Space Agency in April 2014 and April 2016 respectively, opened the prospect of mapping high-resolution crustal velocities and strain rates worldwide. Various processing systems have

been developed to produce interferograms and time series from the continuously growing SAR data sets, such as NASA Jet Propulsion Laboratory's Advanced Rapid Imaging and Analysis (ARIA) (Bekaert et al., 2020), COMET's Looking Into Continents from Space with Synthetic Aperture Radar (LiCSAR) and LiCSBAS suites (Lazecký et al., 2020; Morishita et al., 2020) and ForM@Ter Solid Earth data and services center's ForM@Ter LArge-scale multi-Temporal Sentinel-1 InterferoMetry (FLATSIM) (Thollard et al., 2021).

Automatic data processing for large-scale high-resolution velocity mapping projects often requires subdividing the target area into smaller patches for batch processing. In the case of LiCSAR, acquisitions are organised into $\sim$250$\times$250 km^2 frame units. Yet, multiple challenges exist in combining the independently-processed velocity frames into large-scale velocity fields and producing high-resolution strain rate fields from the velocities. Mosaiced line-of-sight (LOS) velocities can have large mismatches between frames along and across track (Weiss et al., 2020). The high-resolution velocity data has to be downsampled for Cartesian velocity decomposition and strain rate calculation (H. Wang & Wright, 2012; Xu et al., 2021). The resultant strain rate fields can appear overly smooth (Song et al., 2019; Weiss et al., 2020). This study aims to tackle these technical challenges in order to derive large-scale high-resolution velocity and strain rate results without compromising the high quality of the Sentinel-1 data.

We investigate the rapidly deforming NE Tibetan Plateau (Fig 1a), at the leading edge of the northward expansion of the Tibetan Plateau driven by the ongoing collision of India with Eurasia (Molnar & Tapponnier, 1975; England & Houseman, 1985; Pichon et al., 1992; England & Molnar, 1997; Tapponnier et al., 2001; Flesch et al., 2001; Yuan et al., 2013). This area hosted 20 $M_W > 6.5$ earthquakes in the past century, including the M_W7.9 1920 Haiyuan Earthquake (Deng et al., 1986; Institute of Geology, 1990; Ren et al., 2016; Xu et al., 2019; Ou et al., 2020). Extensive research has been carried out to study the kinematics (P. Zhang et al., 1988; W. Zheng et al., 2013), mechanics (Deng et al., 1984; Gaudemer et al., 1995), and seismic hazard (Xiong et al., 2010; Liu-zeng et al., 2015) of the major faults in the region, such as the Haiyuan, Kunlun and West Qinling Faults and the Qilianshan thrusts. However, how strain, the prerequisite for earthquakes, partitions between the major and minor faults, and off-fault areas remains unclear. Geological slip rates have mostly been estimated for the fast-slipping major faults (Kirby et al., 2007; C. Li et al., 2009; J. Li et al., 2016; Yao et al., 2019; Shao et al., 2020). The GNSS network in the area is too sparse to resolve the degree of strain localisation (Gan et al., 2007; Liang et al., 2013; G. Zheng et al., 2017; M. Wang & Shen, 2020). Previous InSAR studies in the area had limited spatial coverage (Cavalié et al., 2008; Jolivet et al., 2012; Daout et al., 2016; Song et al., 2019; Qiao et al., 2021).

We aim to provide the first high-resolution regional overview of present-day deformation of the NE Tibetan Plateau. The large-scale InSAR velocity and strain rate fields resulting from this study provide the fundamental data sets for studying strain partitioning, crustal rheology, and seismic hazard, for testing competing theories about how the continental lithosphere deforms, and for monitoring climatic, hydrological, and anthropogenic processes.

In the following sections, we first describe the processing workflow for generating LOS velocity and uncertainty maps for each frame (Section 2). Then, we introduce new methods for mosaicing and georeferencing the frame maps using GNSS data (Section 3), decomposing the LOS velocity tracks into regional east (V_E) and vertical (V_U) velocity maps (Section 4) and producing low-noise, high-resolution strain rate maps (Section 5). Finally, we highlight the main features observed in the resultant V_E, V_U and strain rate maps, and discuss the implications for regional tectonics, fault mechanics and seismic hazard (Section 6).

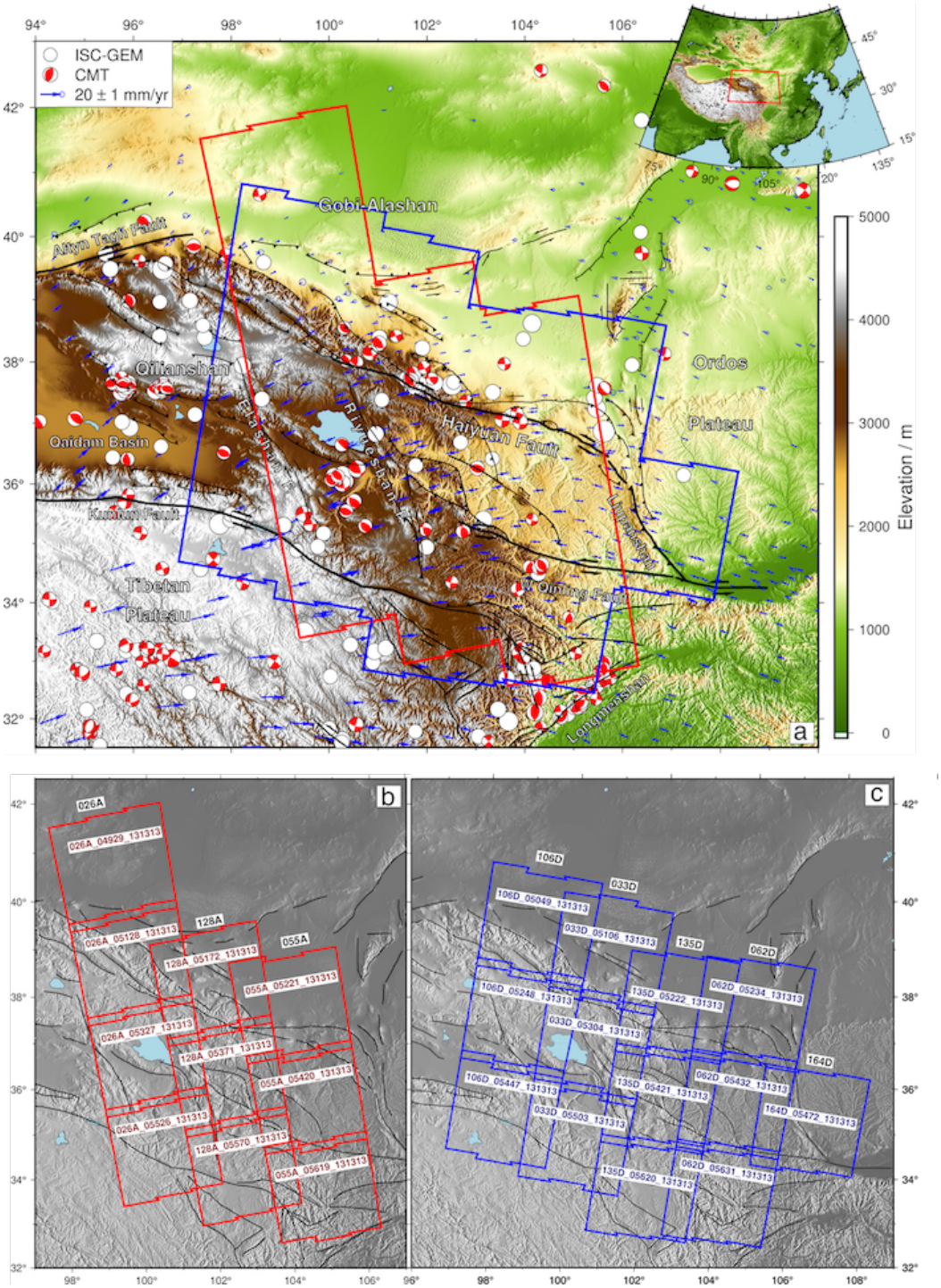

Figure 1. (a) Seismo-tectonic map of the NE Tibetan Plateau with seismicity from ISC-GEM (ISC, 2019) and GCMT (Dziewonski et al., 1981; Ekström et al., 2012) catalogues, GPS velocity vectors from M. Wang and Shen (2020), topography from the 30-arcsecond SRTM digital elevation model (Farr et al., 2007) and faults adapted from Yuan et al. (2013) W. Zheng et al. (2016) and H. Li et al. (2020). Red and blue polygons are the outlines of areas covered by ascending and descending Sentinel-1 InSAR frames, respectively. (b) and (c) show the locations of ascending and descending frames respectively, with COMET-LICSAR frame names labelled.

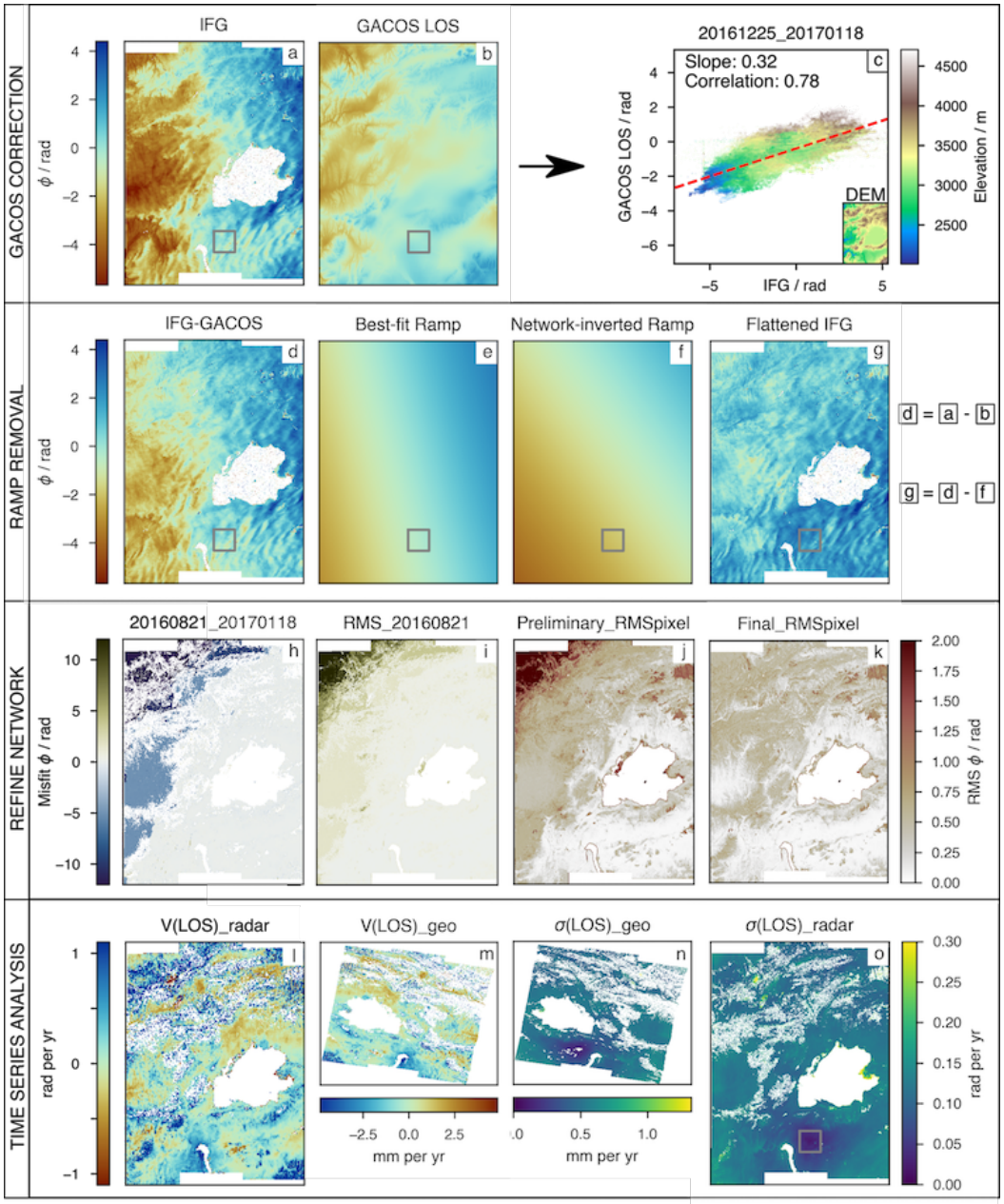

Figure 2. (a-g) Atmospheric delay and ramp removal for an example of an unwrapped interferogram generated by LiCSAR between epochs 20161225 and 20170118 from the frame 033D_05304_131313. The grey boxes in panels (a-g) outline the reference window manually chosen in a stable non-deforming region. The mean value in the reference windows are subtracted from both (a) the unwrapped interferogram and (b) the Generic Atmospheric Correction Online Service (GACOS) atmosphere model back-projected to the line-of-sight (LOS) direction. (c) Scatter plot between corresponding pixel values in (a) and (b) to calculate the slope of the best-fit red dashed line and the correlation of the interferogram and GACOS model for statistical analysis (Fig S3-S4). (e) The best-fit ramp, estimated from (d) the residual after GACOS correction, can be different from (f) the final ramp subtracted from (d) to give (g) the flattened interferogram because the ramp in (f) is obtained through a network inversion to ensure phase closure around interferogram loops. (h,i) Unwrapping mistakes revealed by (h) the error map generated between input and reconstructed interferograms 20160821_20170118, (i) the root-mean-squared (RMS) errors averaged across all interferograms associated with epoch 20160821 and (j) the RMS errors averaged across the preliminary network. All interferograms associated with epoch 20160821 were found to contain unwrapping mistakes and were removed from the network. (k) Improved global error map after network refinement. (l,m) LOS velocities and (o,n) uncertainties in radar and geographical coordinates, respectively, with grey box in (o) highlighting low uncertainties around the reference window.

2 InSAR Data Processing and Time Series Analysis

2.1 Data

Sentinel-1 images over the NE Tibetan plateau were acquired on ascending and descending passes every 24 days from late 2014, and every 12 days from January 2017. We processed 10 ascending frames and 13 descending frames (as defined by LiCSAR, Fig 1b,c) of Sentinel-1A and 1B level-1 Single Look Complex (SLC) products acquired between October 2014 and December 2019. The frames have 65-110 (average 95) acquisition epochs over time spans of 3.2-5.2 (average 4.6) years (Fig S1-S2). Based on statistical reduction of noise, the uncertainty of the LOS velocities derived from time series data, σ_v, is expected to be given by:

$$\sigma_v \simeq \frac{2\sqrt{3}\sigma_e}{\sqrt{N}T} \tag{1}$$

where σ_e is the uncertainty of cumulative displacement per epoch, N is the number of epochs and T is the time span in years (J. Zhang et al., 1997; Morishita et al., 2020). Assuming σ_e ∼10 mm as in Morishita et al. (2020) obtained from a comparison of InSAR and GNSS time series, the number of epochs and lengths of the time span of data we process would theoretically give an approximate lower bound on uncertainty, σ_v, of 0.77 mm/yr in the final velocity maps.

2.2 Interferogram Generation

The interferograms were generated with the LiCSAR automatic processing package (Lazecký et al., 2020). By default, LiCSAR generates interferograms between each epoch and three consecutive epochs both forwards and backwards in time. We changed the limit to six consecutive epochs to create greater redundancy, and added interferograms with six-month and nine-month temporal baselines to provide further connections and hence reduce the impact of the potential biases from the short temporal baseline interferograms (Ansari et al., 2020; Daout et al., 2020). This gave an average of 540 interferograms for each frame (total of 12,480). Interferograms were filtered and unwrapped using version 2 of the statistical-cost, network-flow phase-unwrapping (SNAPHU) algorithm (C. W. Chen & Zebker, 2002), as described in Lazecký et al. (2020). The 23 frames have on average 86% of pixels unwrapped (Fig S1-S2), as expected from the high coherence of the data aided by the stable orbital control of the Sentinel satellites and short temporal baselines. Subsequent processing was carried out with the interferograms in radar coordinates.

2.3 Atmospheric Correction

We used the Generic Atmospheric Correction Online Service (GACOS) models to correct for tropospheric delays in the unwrapped interferograms (Yu et al., 2018). The GACOS models per epoch were converted to radar coordinates, back-projected to the line-of-sight (LOS) direction, and differenced in the same order as the interferometric pairs, before being subtracted from the unwrapped interferograms (Fig 2a,b,d).

The reference area was chosen manually for each frame in an area that is expected to be temporally stable and away from active faults, vegetation, agriculture and desert. The reference window size was set to be 400×400 pixels^2, which is ∼30×30 km^2. This size is small enough to avoid tectonic signals and large enough to average over high-frequency turbulent atmospheric noise. The average pixel value in the reference window is subtracted from the interferograms and their corresponding GACOS models, so that both data sets have the same local reference.

We evaluated the effectiveness of the GACOS correction using both the best-fit slope and Pearson correlation coefficient of the scatter plots between GACOS and interferogram phases (Fig 2c). The 23 frames have correlations between 0.50-0.78 and slopes be-

tween 0.37-0.71 (Fig S3-S4), suggesting that GACOS is better at predicting the spatial pattern of the tropospheric effect than predicting its amplitude (Shen et al., 2019). Interferograms with larger amplitude ranges tend to have slopes and correlations closer to 1 (Fig S3-S4), suggesting the most significant atmospheric delays in the large-amplitude interferograms have been the most effectively corrected.

2.4 Ramp Removal

A planar ramp was then removed from each interferogram by solving for a correction term for each epoch using a network approach following Biggs et al. (2007) and Maubant et al. (2020) (Fig 2e-g, Text S1). This step reduces any remaining long-wavelength signals that might be associated with unmodelled tropospheric delays, ionospheric phases (Gomba et al., 2017), orbital inaccuracies (Fattahi & Amelung, 2014), solid earth tide (Xu & Sandwell, 2020) and any long wavelength tectonics.

2.5 Network Refinement

Time series analysis was performed using the NSBAS program developed by López-Quiroz et al. (2009) and Doin et al. (2015). We used the misfit maps per interferogram (Fig 2h), per epoch (Fig 2i) and their root-mean-squared (RMS) values, $\phi_{RMS_{IFG}}$ and $\phi_{RMS_{epoch}}$ to identify interferograms with unwrapping mistakes. Regions of high values in the $\phi_{RMS_{pixel}}$ map for the entire network (Fig 2j) also indicate the presence of interferograms with unwrapping mistakes. These erroneous interferograms were discarded during the preliminary inversion, which was performed at low resolution and without temporal smoothing or automatic corrections. If the resulting network becomes poorly connected, we made additional interferograms with longer temporal baselines using LiCSAR to build up the network for another preliminary inversion. This process was repeated until all the interferograms in a well-connected network (with at least 3 interferograms linking every epoch) have $\phi_{RMS_{IFG}}$ lower than $\sim$2 rad, and no more clear unwrapping mistakes appear in the overall $\phi_{RMS_{pixel}}$ map.

Then, we remove all 12-day interferograms from the networks for the final time series inversion to mitigate the potential bias from interferograms with short temporal baselines (Ansari et al., 2020). As the 12-day interferograms are only present in the post-2017 time series, removing them means the entire network from 2014 to 2019 is now made of interferograms with temporal baseline of 24 days and above. Removing them only before the final inversion allows us to capitalise on the coherent pixels in those 12-day interferograms for better ramp removal and error identification in the preliminary inversions. The final networks remain connected and have an average of 430 interferograms per frame (Fig S1-S2). Similar to Daout et al. (2020) and Weiss et al. (2020), we find the bias caused by the short-period (12 and 24 days) interferograms negligible when the network is well-connected and contains many long-period (3 and 6 months) interferograms.

2.6 Time Series Analysis

The final network was then inverted in full resolution with temporal smoothing and automatic correction (López-Quiroz et al., 2009) (Text S2). The resultant $\phi_{RMS_{pixel}}$ map was visually checked to confirm there are no remaining unwrapping mistakes (Fig 2k). We inverted a linear velocity, $V(LOS)$, from the time series using weights derived from $\phi_{RMS_{epoch}}$, deviation of each cumulative displacement map from a plane, and deviation of the time series of each pixel from a linear velocity model (Daout et al., 2017, 2018) (Fig 2l,o, Text S3). The uncertainty, $\sigma(LOS)$, takes into account the misfit, the model variance (Tarantola, 2005) and the degree of freedom of the velocity inversion (Daout et al., 2017). The resultant linear velocity and uncertainty maps were then cleaned with the $\phi_{RMS_{pixel}}$ map with a threshold of 0.5 radian to only retain the highest quality pix-

els. Fig 2m and Fig 2n show the geocoded $V(LOS)$ (positive towards the satellite) and $\sigma(LOS)$ maps with their units converted to mm/yr.

3 Frame Mosaicing

The resultant 23 LOS velocity frames are locally referenced. As such, when they are placed in the same regional map, frame and track boundaries are discernible in many places (Fig S5). Following the method of Hussain et al. (2018), Weiss et al. (2020) applied a second-order polynomial to fit the InSAR LOS to the interpolated GNSS LOS. The resultant offsets between frame overlaps along- and across-track had standard deviations between 3.08-3.72 mm/yr (Weiss et al., 2020). These values are significantly larger than the ∼1 mm/yr level (0.77 $\times\sqrt{2}$; see Section 2.1) expected from a 5-year time series. For frame offsets along track, the standard deviation should be even smaller given the largely shared atmospheric noise at the frame overlaps (zero if the networks are identical).

3.1 Joint Inversion of InSAR Frame Overlaps and GNSS Data Points

We aim to develop a method that minimises the LOS differences between frame overlaps along track without using interpolated GNSS velocities for frame tying. As our preliminary tests deramping the frame offsets did not show compelling evidence for the need of higher order adjustments, and considering that higher-order ramps could potentially remove tectonic signals, we invert for a planar ramp per frame to minimise alteration of the InSAR data.

Our method stems from a more advanced method developed by Shen (2020) to mosaic 12 ascending and descending LOS velocity tracks with limited GNSS data. We have more (23) velocities frames to mosaic, thus more (69) ramp parameters to invert for. However, we benefit from a better distribution of GNSS velocities, which allow us to mosaic frames track by track. Our joint inversion is constructed as follows to invert for a planar ramp per frame that fits the LOS differences both between overlapping InSAR frames and between InSAR and GNSS points (Fig S6):

$$\begin{bmatrix} \frac{1}{\sqrt{\sigma_{i1}^2+\sigma_{i2}^2}}(i1-i2) \\ \vdots \\ \frac{1}{\sqrt{\sigma_{i2}^2+\sigma_{i3}^2}}(i2-i3) \\ \vdots \\ \frac{\sqrt{g/h}}{\sqrt{\sigma_{I1}^2+\sigma_{G1}^2}}(I1-G1) \\ \vdots \\ \frac{\sqrt{g/h}}{\sqrt{\sigma_{I2}^2+\sigma_{G2}^2}}(I2-G2) \\ \vdots \\ \frac{\sqrt{g/h}}{\sqrt{\sigma_{I3}^2+\sigma_{G3}^2)}}(I3-G3) \end{bmatrix} = \begin{bmatrix} \frac{1}{\sqrt{\sigma_{i1}^2+\sigma_{i2}^2}}(x_{12} & y_{12} & 1 & -x_{12} & -y_{12} & -1 & 0 & 0 & 0) \\ \vdots \\ \frac{1}{\sqrt{\sigma_{i2}^2+\sigma_{i3}^2}}(0 & 0 & 0 & x_{23} & y_{23} & 1 & -x_{23} & -y_{23} & -1) \\ \vdots \\ \frac{\sqrt{g/h}}{\sqrt{\sigma_{I1}^2+\sigma_{G1}^2}}(x_1 & y_1 & 1 & 0 & 0 & 0 & 0 & 0 & 0) \\ \vdots \\ \frac{\sqrt{g/h}}{\sqrt{\sigma_{I2}^2+\sigma_{G2}^2}}(0 & 0 & 0 & x_2 & y_2 & 1 & 0 & 0 & 0) \\ \vdots \\ \frac{\sqrt{g/h}}{\sqrt{\sigma_{I3}^2+\sigma_{G3}^2}}(0 & 0 & 0 & 0 & 0 & 0 & x_3 & y_3 & 1) \end{bmatrix} \begin{bmatrix} a_1 \\ b_1 \\ c_1 \\ a_2 \\ b_2 \\ c_2 \\ a_3 \\ b_3 \\ c_3 \end{bmatrix} \tag{2}$$

where l in 1, 2 and 3 represents successive InSAR frames along track, il are InSAR LOS from the lth frame in the frame overlap with uncertainties σ_{il}, Il are InSAR LOS in the lth frame at GNSS locations with uncertainties σ_{Il}, Gl are GNSS velocities projected into the line of sight in the lth frame with uncertainties σ_{Gl}; a_l, b_l, c_l are the ramp parameters to be inverted for each frame; x and y are the coordinates of the corresponding pixels in the track, with subscripts 12 and 23 indicating overlaps between frames 1

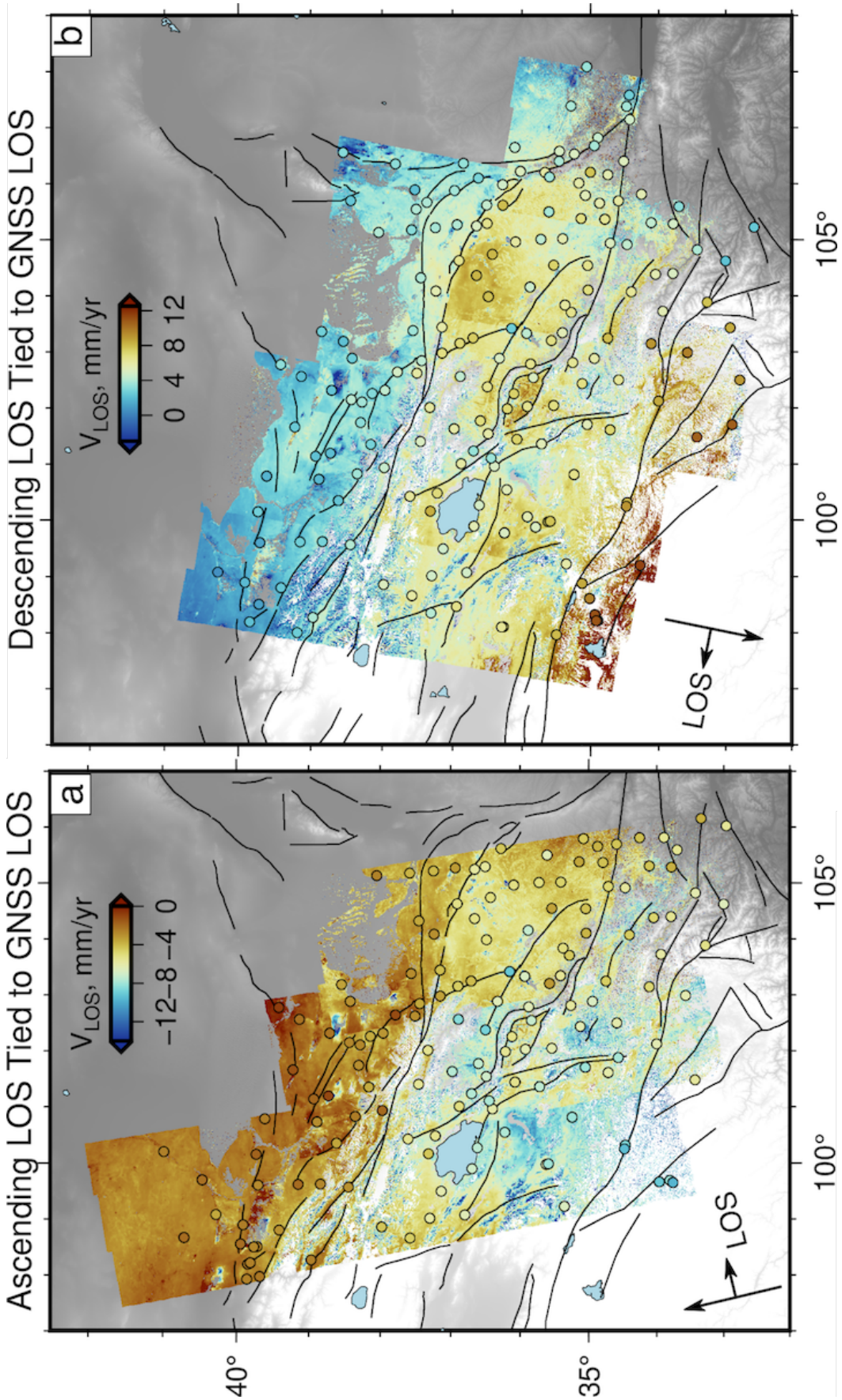

Figure 3. (a) Ascending and (b) descending LOS velocity tracks in the reference frame provided by the GNSS velocities (Liang et al., 2013; M. Wang & Shen, 2020). GNSS LOS are shown in coloured dots

and 2 and between frames 2 and 3, respectively, x_l and y_l indicate coordinates of the GNSS points in the lth frame; g is the total number of InSAR-InSAR offsets from all frame overlaps, and h is the total number of InSAR-GNSS overlaps from all frames.

For the top two rows representing InSAR frame overlap differences, the InSAR LOS values (il) are taken from the $V(LOS)$ maps (Fig 2m) and the σ_{il} are taken from the $\sigma(LOS)$ maps (Fig 2n). For the bottom three rows representing InSAR-GNSS offsets, the InSAR LOS velocities (Il) are chosen to be the weighted average InSAR LOS velocity in a window surrounding the GNSS location, using $\sigma(LOS)$ as weights. This is designed to handle local InSAR variability and avoid wasting GNSS points at empty InSAR pixels. We initialised the size of the window as a 5×5 grid, and let it grow in steps of 2 until it finds at least 10 non-empty pixels from InSAR. All stations found enough InSAR pixels within a window size of 61×61, which is equivalent to an area of $\sim 4.3\times 4.3$ km^2, smaller in dimension than that over which short wavelength tectonic motions like creep would typically occur. The uncertainty associated with this weighted mean is set to be the standard deviation of InSAR LOS pixels in the window.

The GNSS LOS velocities, Gl, and their associated uncertainties, σ_{Gl}, are calculated as:

$$Gl = -V_E cos(\phi) sin(\theta) + V_N sin(\phi) sin(\theta) + V_U cos(\theta) \tag{3}$$

$$\sigma_{Gl} = \sqrt{(\sigma_E cos(\phi) sin(\theta))^2 + (\sigma_N sin(\phi) sin(\theta))^2 + (\sigma_U cos(\theta))^2} \tag{4}$$

where V_E, V_N and V_U are the GNSS velocity components in the east, north and vertical directions, and σ_E, σ_N and σ_U are their associated uncertainties. The horizontal GNSS velocities are in a fixed-Eurasia reference frame (M. Wang & Shen, 2020) and the vertical GNSS velocities are in a stable northern neighbours reference frame (Liang et al., 2013), both transformed from velocities in the IRTF2008 reference frame (Text S4). For both ascending and descending tracks, the heading angle, ϕ, is defined as positive clockwise from north, and the incidence angle, θ, is defined as the angle between the LOS and the vertical (Fig S7).

To strike a balance between quality and abundance of GNSS data points, we used only 3D stations (with east, north and vertical components, Fig S5) when there are more than ten of them in a frame. For three frames with fewer 3D stations, we included 2D stations (with only east and north components, Fig S5), assuming zero vertical velocities (V_U=0) at these stations. Given the near zero mean of the contribution to LOS from V_U estimated at the 3D sites and their almost equivalent-in-magnitude uncertainties, this is a reasonable assumption. To reflect the lack of information on V_U at the 2D stations, we set the uncertainty in the vertical component, σ_U, to be the largest absolute value of the available V_U in the frame. As such, the magnitude of uncertainties associated with the GNSS LOS are comparable to that of the InSAR LOS, both at the ∼1 mm/yr level. This means the combined uncertainties of InSAR-InSAR offsets and that of InSAR-GNSS offsets are also of similar magnitudes. Therefore, we only needed to prevent the joint inversion from being dominated by the much greater number of InSAR-InSAR offsets relative to the InSAR-GNSS offsets ($g \gg h$). To do so, we weight the bottom three lines (i.e., lines involving GNSS) in Equation 2 by $\sqrt{g/h}$, so that the sum of the mean-squared misfits from these two data sets is minimised.

3.2 Effectiveness of Joint Inversion

After mosaicing the InSAR LOS frames using the method described above, the stitched InSAR LOS tracks no longer show along-track frame boundaries (Fig 3). Instead, the track boundaries become more obvious, reflecting the across-track change in incidence angle. From north to south, the ascending LOS velocities become increasingly negative and the descending LOS velocities become increasingly positive, as expected from the increasing east-component velocities (Fig 1a). The remaining LOS changes are well-aligned

with mapped faults, especially along the single-strand portions of the Haiyuan and East Kunlun Faults.

Statistically, the resultant along-track frame overlap residuals have standard deviations that range between 0.3–2.1 mm/yr and average to 0.87 mm/yr (Fig S8). Overlaps with larger residuals are associated with frames impacted by desert in the northeast, and vegetation and loess in the southeast. The histograms of these frame overlap residuals also follow Gaussian distributions centered near zero (average mode of -0.02 mm/yr), characteristic of random noise. The InSAR-GNSS LOS residuals, with on average 45 GNSS points per track, have an average mode of 0.04 mm/yr and an average standard deviation of 1.27 mm/yr (Fig S9). If equally split between the InSAR and GNSS, this InSAR-GNSS LOS residual suggests less than 1 mm/yr error in each data set.

4 Velocity decomposition

The ascending and descending LOS velocity maps provide measurements of velocity in two directions. In order to decompose the two LOS velocities into standard 3-component velocities (east, north and vertical), a third constraint must be provided. Hussain et al. (2018) and Weiss et al. (2020) used the interpolated north velocities from GNSS data and the two LOS velocities to simultaneously solve for the east (V_E) and vertical (V_U) velocity components. Tymofyeyeva and Fialko (2018) and Xu et al. (2021) decomposed the LOS velocities into a vertical component and a horizontal component in the local direction determined by interpolated east and north GNSS velocity fields. Both methods require a good distribution of GNSS velocities, which is not available everywhere on the continents.

Shen (2020) and Shen et al. (2021) developed an alternative method to obtain V_E straight away from InSAR LOS by decomposing the ascending and descending LOS into V_E and V_{UN}, where V_{UN} is the combined LOS contributions from the V_N and V_U components projected onto the north-up plane. This method is a simple way of getting high resolution decomposed fields without using an interpolated GNSS V_N. However, it also introduces a different source of error as the V_{UN} vector direction changes slightly with the line-of-sight, the decomposed V_{UN} becoming an approximation of the true values on different tracks. The error from the approximation of V_{UN} can also spill into the V_E obtained. We implement this method and show that the error introduced by the V_{UN} approximation is negligible in comparison to the noise level of the data and build upon this method to extract the V_U from V_{UN} using interpolated V_N.

4.1 Stage 1: Decomposition into V_E and V_{UN}

Following Shen (2020) and Shen et al. (2021), we first decomposed the two LOS velocities into V_E and V_{UN} via:

$$V(LOS) = -V_E cos(\phi) sin(\theta) + V_{UN}\sqrt{1 - sin^2(\theta) cos^2(\phi)} \tag{5}$$

based on the mathematical derivation provided in Fig S7. This partitioning is performed independently for each pixel covered by at least one ascending track and one descending track. The resultant V_E and V_{UN} maps (Fig S10a,c) have the shapes of the overlapping area of the ascending and descending data coverage (Fig 1a). The general form of the inversion is as follows:

$$\begin{bmatrix} \frac{1}{\sigma(a_0)} LOS_{a_0} \\ \frac{1}{\sigma(a_1)} LOS_{a_1} \\ \frac{1}{\sigma(d_0)} LOS_{d_0} \\ \frac{1}{\sigma(d_1)} LOS_{d_1} \end{bmatrix} = \begin{bmatrix} \frac{1}{\sigma(a_0)}(-cos(\phi_{a_0}) sin(\theta_{a_0}) & \sqrt{1 - sin^2(\theta_{a_0}) cos^2(\phi_{a_0})}) \\ \frac{1}{\sigma(a_1)}(-cos(\phi_{a_1}) sin(\theta_{a_1}) & \sqrt{1 - sin^2(\theta_{a_1}) cos^2(\phi_{a_1})}) \\ \frac{1}{\sigma(d_0)}(-cos(\phi_{d_0}) sin(\theta_{d_0}) & \sqrt{1 - sin^2(\theta_{d_0}) cos^2(\phi_{d_0})}) \\ \frac{1}{\sigma(d_1)}(-cos(\phi_{d_1}) sin(\theta_{d_1}) & \sqrt{1 - sin^2(\theta_{d_1}) cos^2(\phi_{d_1})}) \end{bmatrix} \begin{bmatrix} V_E \\ V_{UN} \end{bmatrix} \tag{6}$$

where a_0, a_1, b_0 and b_1 are notations for the up-to-two possible overlapping ascending tracks and up-to-two possible overlapping descending tracks covering a pixel. σ is $\sigma(LOS)$

scaled on a spherical model fit to the $\sigma(LOS)$ profile away from the reference center (Text S5, Fig S11), such that the decomposition will not be overly influenced by data that happen to be in or near the reference window. The number of rows in Equation 6 per pixel depends on the number of tracks covering the pixel with valid data.

We propagate the uncertainties $\sigma(LOS)$ to $\sigma(V_E)$ and $\sigma(V_{UN})$ (Fig S10b,d) through a data covariance matrix, $cov(LOS)$, with only squares of the scaled $\sigma(LOS)$ (Text S5, Fig S11) in the diagonal terms, based on the assumption that all LOS measurements (from different tracks) are independent. $\sigma(V_E)$ and $\sigma(V_{UN})$ are obtained from the square-root of the diagonal terms of the covariance matrix of V_E and V_{UN}, $cov(V_E, V_{UN}) = [A^T cov(LOS)^{-1} A]^{-1}$, with A the transformation matrix from Equation 6.

This method is suitable for areas away from the poles where the heading direction of the track is near north-south, hence the variation of the angle, γ, between the V_{UN} vector and the vertical axis is small (Fig S7). In our study area, γ varies between $\sim 6-9^\circ$ which translates into errors of V_{UN} as the vector sum of $\sim$ 2% of V_N and $\sim$ 0.5% of V_U, as $V_{UN} = -V_N sin(\gamma) + V_U cos(\gamma)$. Therefore, the majority of the error actually comes from the north-south motion. For LOS data of 1 mm/yr uncertainty, this method is robust up to V_N=50 mm/yr.

We further compare our V_E (Fig 4a) with that obtained through the conventional way where the interpolated GNSS V_N is used to remove the contribution of V_N from the two LOS velocities, which are then used to estimate V_E and V_U (Hussain et al., 2018; Weiss et al., 2020). The differences in the two V_E maps are small (0.01±0.03 mm/yr) (Text S6, Fig S12), but the advantages of the $V_E - V_{UN}$ decomposition are that the results are not biased from, and the resolution not reduced because of, the GNSS interpolation.

As the uncertainty level continues to decrease, with longer time series enabled by Sentinel-1's 20 year mission, the errors introduced by the V_E and V_{UN} decomposition will become more significant. One way to mitigate this effect is to choose a reference frame in which V_N is small. This can be done by transforming the GNSS velocities to a reference at the center of the study region (Shen, 2020; Shen et al., 2021) before using the GNSS to mosaic the InSAR LOS (Section 3).

4.2 Stage 2: Decomposition of V_{UN} into V_U and V_N

By this stage, we have isolated V_E (Fig 4a) and are left with the subvertical component V_{UN} (Fig S10c) which is related to the two as yet undetermined velocity components V_U and V_N. It is now necessary to introduce external constraints on the velocities, i.e., GNSS, to separate these two components. As InSAR is more sensitive to V_U than to V_N and GNSS have higher quality measurements and more data points in V_N than in V_U, we interpolated V_N from GNSS velocities to obtain the V_U field.

We interpolate the north component of the GNSS velocities from (M. Wang & Shen, 2020) using the universal kriging algorithm of the Pykrige (v1.6.0) Python module (Murphy et al., 2021). We first cleaned the GNSS data by removing data points with north uncertainties greater than 0.7 mm/yr, which reduced the majority of cases where nearby points had contradictory measurements. The universal kriging algorithm allows a polynomial surface to be removed before and added back after interpolation. We chose to remove a best-fit third order polynomial surface that best describes the distribution of GNSS V_N values. To determine the distance-dependent weighting of data points for interpolation, we fitted a spherical model to the semivariogram calculated from the detrended V_N values:

$$\begin{cases} n + p \times (\frac{3d}{2r} - \frac{d^3}{2r^3}) & d \leq r \\ n + p & d > r \end{cases} \tag{7}$$

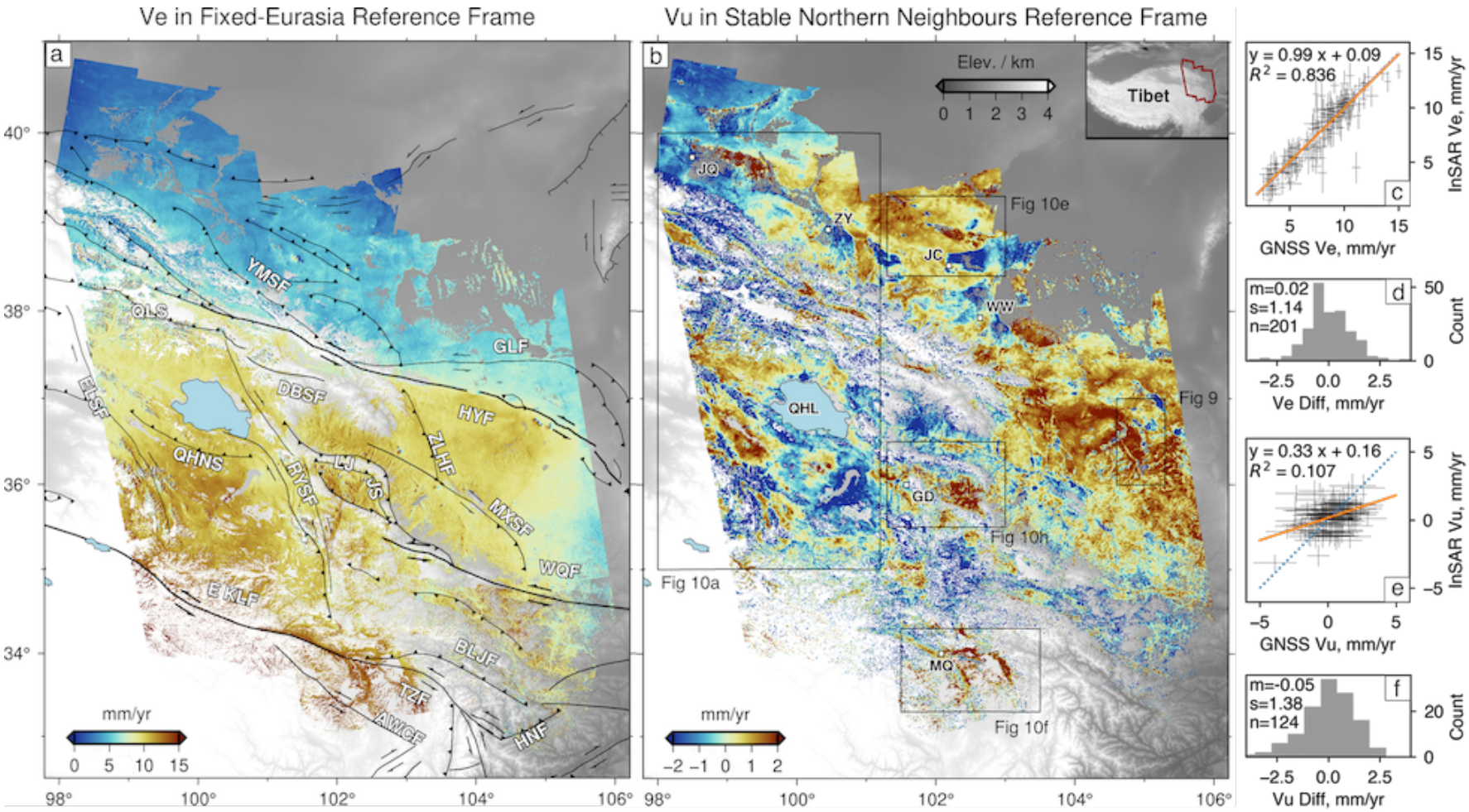

Figure 4. (a) East velocity, V_E, map from direct decomposition of ascending and descending LOS velocity tracks. (b) Vertical velocity, V_U, map decomposed from InSAR V_{UN} (Fig S10b) using interpolated GNSS V_N (Fig S13a). See uncertainty maps in Fig S10 and Fig S13. Elevation is from Shuttle Radar Topography Mission 3-arcsecond Digital Elevation Model (Farr et al., 2007). Faults: HYF=Haiyuan, QLS=Qilianshan, EKLF=East Kunlun, WQF=West Qinling, GLF=Gulang, ZLHF=Zhuanglanghe, MXSF=Maxianshan, JS=Jishishan, LJ=Lajishan, RYSF=Riyueshan, DBSF=Dabanshan, QHNS=Qinghai Nan Shan, ELSF=Elashan, BLJF=Bailongjiang, TZF=Tazang, AWCF=Awancang, HNF=Hanan, YMSF=Yumushan. Cities: JQ=Jiuquan, ZY=Zhangye, JC=Jinchang, WW=Wuwei, GD=Guide, MQ=Maqu, QHL=Qinghai Lake. (c-f) Regressions and histograms of differences between InSAR and GNSS V_E and V_U velocities. (c,e) Crosses = InSAR and GNSS velocities with uncertainties. Orange line = weighted best-fit linear model. Blue dotted line = one-to-one line for reference. (d,f) Differences are calculated as GNSS-InSAR. m=mean, s=standard deviation, n=number of GNSS component velocities in InSAR coverage.

where n is the nugget, s is the sill, $p = s - n$ is the partial sill, r is the range, and d is the distance between any pair of GNSS points. A spherical model was chosen instead of a Gaussian or an exponential model to strike a balance between interpolation smoothness and feature retention. This model also determines how uncertainties increase with distance from the data points (Fig S13a,b).

For each track that covers a pixel, a velocity V_U and its uncertainty $\sigma(V_U)$ can be calculated as:

$$V_U = V_{UN}\frac{\sqrt{1 - sin^2(\theta)cos^2(\phi)}}{cos(\theta)} - V_N sin(\phi)tan(\theta) \tag{8}$$

$$\sigma(V_U) = \sqrt{\sigma^2(V_{UN})\frac{1 - sin^2(\theta)cos^2(\phi)}{cos^2(\theta)} + \sigma^2(V_N)\frac{sin^2(\phi)sin^2(\theta)}{cos^2(\theta)}} \tag{9}$$

Hence, pixels in the track overlaps can have up to four realisations of V_U and $\sigma(V_U)$. For such pixels, a weighted mean of the V_U, $\bar{V}_U = \frac{\Sigma V_{U\,i}/\sigma(V_U)_i}{\Sigma 1/\sigma(V_U)_i^2}$, and the uncertainty of the weighted mean, $\sigma(\bar{V}_U) = 1/\sqrt{\Sigma 1/\sigma(V_U)_i^2}$, are evaluated for the final result (Fig 4b and Fig S13c,d).

4.3 Comparing InSAR and GNSS Velocities and Uncertainties

As only the LOS components from 3D GNSS stations were used in the frame stitching, except for three frames on the edges with fewer than ten 3D stations (Fig S5), and only the V_N GNSS velocities were used in the second step of velocity decomposition, as an additional quality check, it is possible to compare directly the resultant V_E, V_U and their associated uncertainties derived from InSAR with those of the GNSS. The one-to-one fit between InSAR and all 201 stations of GNSS V_E has a gradient of 0.99 and a R^2 of 0.84 (Fig 4c) (or a gradient of 0.93 and a R^2 of 0.76 if only comparing with 62 2D GNSS stations that were not used for tying InSAR LOS). This agreement is remarkable given the high precision of GNSS velocities in the east component (Fig S10a-b). In contrast, the V_U components from InSAR and GNSS only exhibit a weak positive correlation with a gradient of 0.33 and R^2 of 0.11 (Fig 4e). This fit is not surprising given that the uncertainties associated with the GNSS V_U are almost as large as their absolute values. Nevertheless, it is worth noting that the InSAR σV_U is only one third of GNSS σV_U (Fig S13d), thanks to the steep line-of-sight of the satellites. The InSAR V_U map is also characterised by a high degree of spatial variability, which would not have been captured by the sparse GNSS points alone, highlighting the advantages of using InSAR for observing vertical motions. The average differences between InSAR and GNSS V_E and V_U are 0.02 mm/yr and -0.05 mm/y, respectively (Fig 4d,f), confirming that our referencing procedure does not add any biases. The standard deviations of the V_E and V_U differences are 1.14 mm/yr and 1.38 mm/yr, respectively, similar to the 1.00±0.26 mm/yr and 1.67±0.23 mm/yr expected from the combined uncertainties from InSAR and GNSS, suggesting the uncertainties estimated for InSAR V_E and V_U are reasonable.

5 Strain Rate Calculation

Most existing methods for strain rate calculation were designed to derive continuous strain rate fields from sparse and irregularly-spaced levelling or GNSS velocity points. This problem is typically treated either as a velocity interpolation problem with a user choice of smoothing, coupling or tension factor (e.g. Smith & Wessel, 1990; Sandwell & Wessel, 2016), or an inversion problem where strain rates or stresses are directly inverted from velocity point data (e.g. Haines & Holt, 1993; Kreemer et al., 2014; Haines et al., 2015; Haines & Wallace, 2020). The former tends to suffer from poorly constrained uncertainties whereas the latter can be limited by computational power. Kinematic block modeling (e.g. Meade & Hager, 2005; Loveless & Meade, 2010; McCaffrey et al., 2013)

is yet another approach that is often used to focus strain on predefined faults although the number of blocks tends to grow with the number of velocity measurements incorporated into the model. Pagani et al. (2021) developed a Bayesian approach to extract strain rate from an ensemble of interpolated velocities derived from variable triangular meshes. However, none of these approaches have incorporated the dense velocities measured by InSAR.

Hitherto, strain rate calculations from InSAR velocities have relied on downsampling the InSAR data because of the computational limit of the N data by N data matrix inversion and the need to reduce short-wavelength noise in the InSAR velocities (Song et al., 2019; H. Wang et al., 2019; Weiss et al., 2020; Xu et al., 2021). Xu et al. (2021) subsampled the decomposed horizontal InSAR velocities to 2.5 km resolution before interpolating with the *gpsgridder* algorithm of Sandwell and Wessel (2016). For studies using the VELMAP method (H. Wang & Wright, 2012), strain rate is obtained from velocities inverted at the vertices of a triangular mesh using spherical approximation equations (Savage et al., 2001). As the inversion is underdetermined, it needs to be regularised through a smoothing criteria. Although the strength of smoothing is typically chosen by examining the trade-off between misfit and solution roughness, the exact choice of smoothing strength remains somewhat subjective. The data downsampling, smoothing, and low-resolution mesh act to dampen the true strain rate magnitudes and mask large velocities discontinuities that might be associated with creeping faults. Here, we present a new method for strain calculation that preserves the resolution of the InSAR velocities and the sharpness of the strain patterns as much as possible and guides noise suppression using synthetic tests performed on 1D velocity profiles.

5.1 Combining Gradients of Filtered V_E and Interpolated V_N

The gradients of the unfiltered velocities are very noisy due to the $\sim$ 1 mm/yr uncertainty level and the close spacing between velocity observations, thus various filtering strategies were tested. To investigate how filtering affects the signal-to-noise ratio and the strain localisation on faults, we performed synthetic tests on a velocity profile generated using a 1D elastic dislocation model (i.e., a screw-disclocation; Savage, J. C., Burford, 1973) at the same resolution, and with a similar noise level, as the InSAR V_E estimates (Fig S14-S15). Results show that a sliding median filter is better at preserving the shapes of the velocity and gradient profiles than a mean filter (Fig S14a). In addition, applying the filter to the velocity profile before taking the gradients produces more stable results than applying the filter to the unfiltered velocity gradients (Fig S14b). Subsampling the $\sim$100 m resolution velocity profile to $\sim$1 km resolution does not alter profile shape or affect inverted parameters but effectively reduces computational time. We also find that the filter window required to suppress noise is a function of the velocity step, fault locking depth and noise level of the data. A larger filter window is needed for a profile with a larger velocity step, a shallower fault locking and a higher noise level. We experimented with different window sizes and found that a 60 km window is the most suitable for smoothing velocity profiles with noise between 0.5–1 mm/yr, velocity steps between 3–15 mm/yr, typical of slip rates across the Haiyuan and East Kunlun Faults (Kirby et al., 2007; C. Li et al., 2009; J. Li et al., 2016; Yao et al., 2019; Shao et al., 2020), and locking depths between 3–20, typical of locking depths for continental crust (Wright et al., 2013) (Fig S15-S16).

Therefore, we applied a sliding median filter with a 60 $\times$ 60 km window size to the InSAR V_E (Fig S17) before calculating the gradients $\partial V_E/\partial x$ and $\partial V_E/\partial y$. Because the interpolated GNSS V_N is already smooth due to the sparse distribution of control points (Fig S13a,b), we directly evaluate $\partial V_N/\partial x$ and $\partial V_N/\partial y$ without applying additional filtering. The horizontal strain-rate tensor, $\dot{\varepsilon}_h$, is the symmetrical component of the velocity gradient tensor composed of the four velocity gradients, so that the horizontal dilatation rate ($\dot{\varepsilon}_{dil}$, Fig 5e), the maximum shear rate ($\dot{\varepsilon}_{shear}$, Fig 5f), and the second in-

variant of the horizontal strain-rate tensor ($\dot{\varepsilon}_{II_h}$, Fig 5g), are defined as follows (Turcotte & Schubert, 2014; Sandwell & Wessel, 2016; M. Wang & Shen, 2020):

$$\begin{aligned}
\dot{\varepsilon}_h &= \begin{bmatrix} \dot{\varepsilon}_{xx} & \dot{\varepsilon}_{xy} \\ \dot{\varepsilon}_{yx} & \dot{\varepsilon}_{yy} \end{bmatrix} = \begin{bmatrix} \frac{\partial V_E}{\partial x} & \frac{1}{2}(\frac{\partial V_E}{\partial y} + \frac{\partial V_N}{\partial x}) \\ \frac{1}{2}(\frac{\partial V_N}{\partial x} + \frac{\partial V_E}{\partial y}) & \frac{\partial V_N}{\partial y} \end{bmatrix} \\
\dot{\varepsilon}_{dil} &= \dot{\varepsilon}_{xx} + \dot{\varepsilon}_{yy} \\
\dot{\varepsilon}_{shear} &= \sqrt{\dot{\varepsilon}_{xy}^2 + (\dot{\varepsilon}_{xx} - \dot{\varepsilon}_{yy})^2/4)} \\
\dot{\varepsilon}_{II_h} &= \sqrt{\dot{\varepsilon}_{xx}^2 + 2\dot{\varepsilon}_{xy}^2 + \dot{\varepsilon}_{yy}^2}
\end{aligned} \tag{10}$$

5.2 Uncertainties in the Strain Rates

5.2.1 Quantitative Estimates of Strain Rate Uncertainties

The uncertainties in the strain rates should come from that of the component velocity gradients, which in turn depend on the uncertainties of the median filtered InSAR V_E and interpolated GNSS V_N fields. Analytically deriving the uncertainties of V_E gradients taking into account the spatial covariance between pixels is challenging because of the median filtering step. Therefore, we empirically estimated V_E gradient uncertainties at an area overlapped by two ascending and two descending tracks. We first created four versions of V_E, via V_E-V_{UN} decomposition (Section 4.1), from four possible combinations of one of the ascending tracks and one of the descending tracks. Then, we median-filtered them and compared their horizontal gradients (Fig S18). The four versions of V_E gradients give standard deviations of 7.8 nst/yr for $\partial V_E/\partial x$ and 4.3 nst/yr for $\partial V_E/\partial y$, which represent 17% and 10% uncertainty levels relative to the gradient signals (46.4 nst/yr for $\partial V_E/\partial x$ and 45.9 nst/yr for $\partial V_E/\partial y$) (Fig S18). These uncertainties are upper bounds for two reasons. First, the error introduced by the approximation of the V_{UN} vector is the largest on the edges, as in the track overlaps, as compared to in the central parts of a track. Second, our V_E (Fig 4a) in track overlaps is evaluated from all available (three or four) tracks instead of just two tracks used in this experiment; the addition of neighbouring track(s) would reduce this error with both near-range and far-range LOS velocities involved in the inversion (Section 4.1, Fig S12).

To estimate the uncertainties of V_N gradients, we used the Monte Carlo method to create 100 interpolated GNSS V_N fields, each time varying each GNSS V_N velocity by an amount randomly sampled from a Gaussian distribution with associated $\sigma(V_N)$, assuming the $\sigma(V_N)$ are independent. From the 100 derived $\partial V_N/\partial x$ and $\partial V_N/\partial y$ fields, we find 7.2 nst/yr and 5.7 nst/yr of uncertainties relative to 10.6 nst/yr and 10.8 nst/yr of the gradient signals, respectively (Fig S19). These statistics reflect the high noise-to-signal ratios (68% for $\partial V_N/\partial x$ and 53% for $\partial V_N/\partial y$) of the gradients of a spatially smooth V_N field. Taking 7.8 nst/yr for $\sigma(\partial V_E/\partial x)$, 4.3 nst/yr for $\sigma(\partial V_E/\partial y)$, 7.2 nst/yr for $\sigma(\partial V_N/\partial x)$ and 5.7 nst/yr for $\sigma(\partial V_N/\partial y)$, we have uncertainties of 6.3 nst/yr on the maximum shear rate, 9.7 nst/yr on the dilatation rate and 7.0 nst/yr on the second invariant.

5.2.2 Overestimated Strain in Areas of Large $\sigma(V_E)$

As the velocity gradients are squared in the evaluation of maximum shear and second invariant, any noise remaining in the filtered V_E will lead to oscillating gradients of opposite signs (Fig S15a) and an overestimation of the strain rates. This is most likely the case around the West Qinling Faults and near the eastern termination of the East Kunlun Fault (Fig 5), where $\sigma(V_E)$ is up to 2 mm/yr (Fig S10b). We estimate the degree of this overestimation by filtering 1000 simulations of arctangent velocity profiles and analysing the absolute V_E gradients summed over the filtered profile relative to that of the model. For a profile with 2 mm/yr Gaussian noise, 20 km locking depth and 5 mm/yr of velocity step, using a 60 km filter window can lead to overestimates in the absolute

gradients by 23±8%. This percentage overestimation will increase with smaller velocity steps and shallower locking depths as the signal-to-noise ratio decreases.

5.2.3 Underestimated Strain from Low-Resolution GNSS V_N Gradients

The interpolated GNSS V_N field is smoother than the V_E field due to the lower density of the GNSS measurements. As a result, the GNSS velocity gradients are also less sharp and have lower amplitudes than the V_E gradients (Fig 5a-d). This difference has an impact on the spatial patterns in the strain-rate maps, with contributions from the V_N gradients being comparatively weaker. Therefore, we should be mindful of potentially underestimated shear strain rates over N-S oriented strike-slip faults (e.g., Riyueshan Fault) and contractional strain rates over E-W oriented reverse faults (e.g., Qilianshan thrusts).

6 Main Features in the Velocity and Strain-Rate Fields

Our analysis results in two regional velocity maps (Fig 4a,b) covering an area of 440,000 km^2 with ∼100 m resolution, as well as three strain rate maps at ∼ 1 km resolution with better spatial coverage because of the filtering (Fig 5e-g). These maps provide a new, extensive view of the crustal motion of the NE Tibetan Plateau at unprecedented resolution.

6.1 Strain Localisation along Haiyuan and East Kunlun Faults

We observe concentrated strain along the major Haiyuan and East Kunlun Faults (Fig 5g). We also see more distributed strain across the Qilianshan and West Qinling Fault, as well as some finite strain away from the main faults. If we mask out pixels with second invariant strain rate above 40 nst/yr, as highlighted in Fig 5g, the remaining pixels together sum up to half of the total strain rate in the study region and average to 21 nst/yr. The major faults accommodate on average 76 nst/yr of strain rate across 20% of the area.

The spatial extent of the strike-slip motion on the Haiyuan Fault is most clearly defined in the maximum shear rate map (Fig 5f), with high shear extending from Haiyuan County in the east, to Qilian County in the west, where the strike-slip fault terminates and transitions into the Changma and North Qilianshan thrusts. This is consistent with the change of strain patterns to the west of Qilian County where the maximum shear diminishes and transitions to contraction in the form of strongly negative dilatation rates (Fig 5e). In comparison to the Haiyuan Fault, elevated strain on the East Kunlun Fault is less tightly localised on the main fault strand, with shear observed to the south of the fault near Maqing and to the north of the fault near Maqu, where the strain appears distributed across multiple strands.

6.2 Contractional Strain at Fault Junctions

We also observe focused strain at fault junctions where the Haiyuan Fault branches into the Qilianshan Thrusts and where it interacts with the Gulang and Lianhuashan Faults, as well as where the East Kunlun Fault meets the Awancang Fault. These transition areas are characterized by contractional strain rates (i.e., negative dilatation; Fig 5e), suggesting volumetric changes and stress anomalies at the triple junctions, likely induced by relative motion of neighbouring crustal material at the branching points. This observation is in agreement with the model of King and Nábělek (1985) where off-fault strain is expected at a process zone around a three-fault junction to permit zero displacement at the fault intersection. We cannot tell the difference between elastic strain accumulation and plastic strain that does not end up in earthquakes. Further modelling could assess the degree to which off fault deformation is required to release the strain observed.

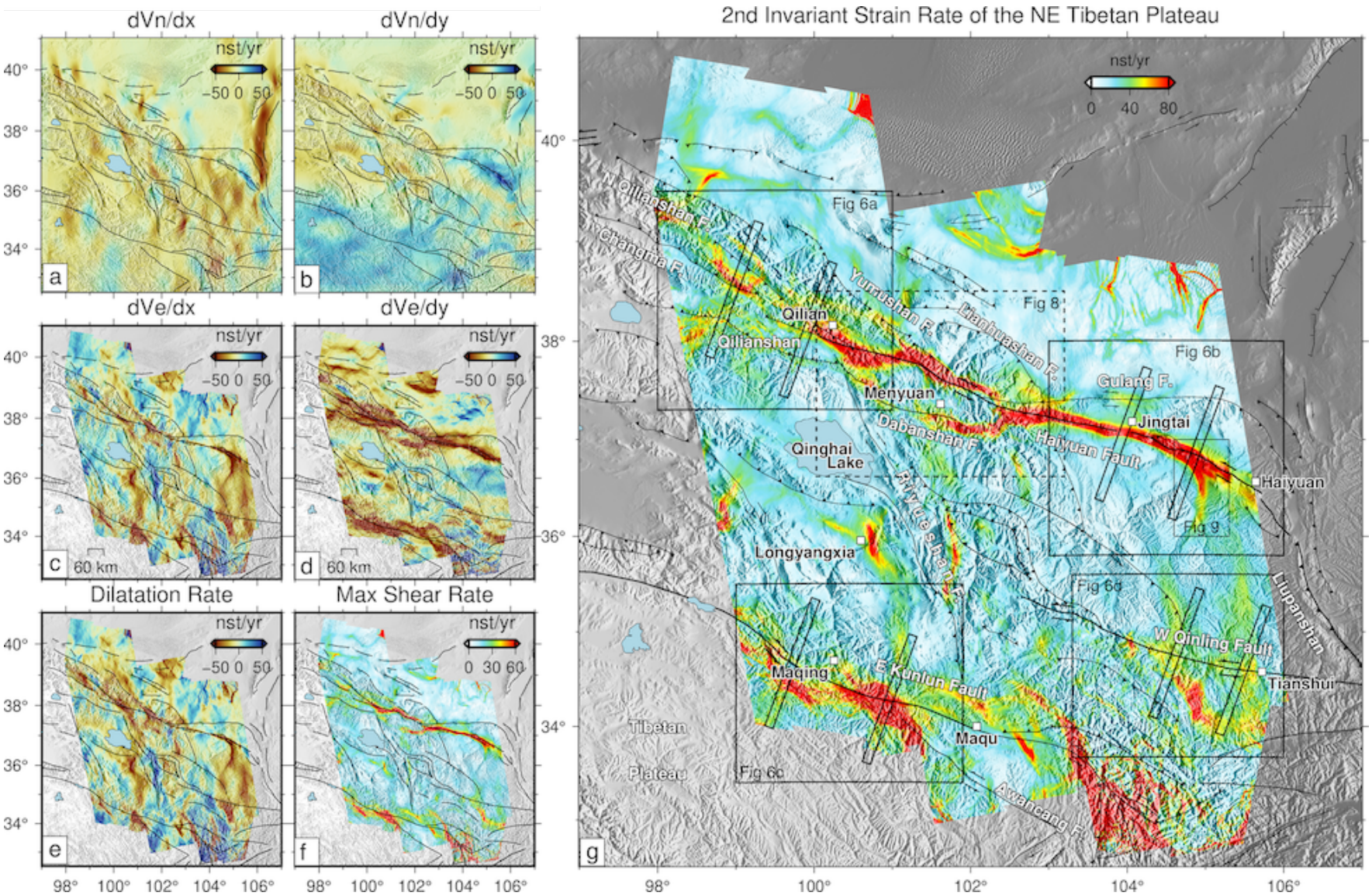

Figure 5. (a) $\partial V_N/\partial y$ and (b) $\partial V_N/\partial x$ velocity gradients calculated from the interpolated GNSS V_N map shown in Fig S13a. (c) $\partial V_E/\partial y$ and (d) $\partial V_E/\partial x$ calculated from the V_E map median-filtered with a 60 km × 60 km window size. Maps of (e) dilatation rate, (f) maximum shear and (g) second invariant of the horizontal strain-rate tensor, calculated from the velocity gradients (a-d) using Equations 10. The colour scales are chosen to highlight strain concentration along faults.

Understanding such focused strain at the fault bends and branches is crucial as such geometric complexities might promote the initiation and termination of future earthquakes (Schwartz & Sibson, 1989; Bhat et al., 2007; Wesnousky, 2008; Walters et al., 2018; Quigley et al., 2019; Sathiakumar & Barbot, 2021).

6.3 Strain-rate and V_E Profiles Across Faults

We further compare strain rates and V_E across the Qilianshan and Haiyuan, East Kunlun and West Qinling Faults using a suite of fault-perpendicular profiles (Fig 6). The magnitude and shapes of the strain peaks are largely related to the step size and gradients of the V_E profiles. A typical arctangent-shaped profile over the East Kunlun Fault (Fig 6c, profile 2-2') corresponds with a Gaussian-shaped strain-rate profile. The 7.3 mm/yr velocity step is likely a combined contribution from both East Kunlun and Awangcang Faults. Despite having a larger velocity step, this long wavelength V_E profile gives rise to a broad strain profile with a lower peak strain value than that of the profile 2 over the Haiyuan Fault (Fig 6b, profile 2-2'), where strain is more localised. A sharp velocity step in V_E in profile 1 across the Haiyuan Fault corresponds to a spike in the strain-rate profile, with a secondary step over the Gulang Fault indicated by a smaller peak in the strain-rate profile (Fig 6b, profile 1-1'). Multiple strain peaks are observed across both profiles over the Qilianshan (Fig 6a), as expected from strain partitioning across the parallel thrusts. The West Qinling Fault is characterised by nearly linear velocity profiles which correspond to near flat strain rate profiles without any prominent peaks associated with the surface fault traces. This suggests that either this area is characterised by distributed deformation, or any localised strain is hidden in the noise caused by vegetation and loess cover in this area, or we could be seeing a seismic cycle effect with rapid postseismic strain rate after a M 8 events that occurred here in 1654 (CEA-PBED, 1995) and slow interseismic strain rate observed now (Elliott et al., 2016; Hussain et al., 2018; Zhu et al., 2020).

6.4 Creep Detection and Creep Rate Measurement over the Laohushan Section

In Fig 7a, we plot the second invariant of strain rate map (Fig 5g) using an adjusted colour map in order to highlight the 30-km-long Laohushan section where creep has been documented over the past three decades (Cavalié et al., 2008; Jolivet et al., 2013, 2015). The V_E profile in Fig 7c shows that the creep has continued between the years 2014 and 2020 with a V_E step of 2.8 ± 0.3 mm/yr, based on the weighted means of the velocities within 5 km on each side of the fault. The equivalent fault parallel creep rate is 2.9 ± 0.3 mm/yr, assuming no vertical or fault perpendicular motions, consistent with the 2.5 ± 0.4 mm/yr obtained by Y. Li et al. (2021) using GNSS, Evisat and levelling data. This is slower than the 5±1 mm/yr measured by Evisat InSAR data between 2004–2009 (Jolivet et al., 2012), and the 6.3 ± 2 mm/yr measured by ERS InSAR data between 1993-1998 (Cavalié et al., 2008), suggesting recent decrease in the creep velocity. The V_E and V_U decomposition also helps separate horizontal creep from the subsidence signal in the Jingtai Basin. The Jingtai Basin is located at a releasing jog between the Laohushan segment to the west and the 1920 Haiyuan Earthquake surface rupture to the east (Jolivet et al., 2012; Han et al., 2021). The subsidence could be caused by extension across the basin induced by the 1920 Haiyuan Earthquake, which would also have lowered the normal stress and hence promoted creep. The continuous decrease of the creep rate over the past three decades suggests that this creep is transient, possibly in relation with the rupture termination of 1920 Haiyuan Earthquake.

We also identify a $\sim$ 66 km long high strain segment further west on the Haiyuan Fault. This could be related to a M_W 5.9 Menyuan Earthquake that occurred on January 21, 2016 (Fig 7a, Fig 8d). However, considering that the fault patch that slipped during the earthquake was only 20 km long (Y. Li, Shan, et al., 2016; H. Wang et al.,

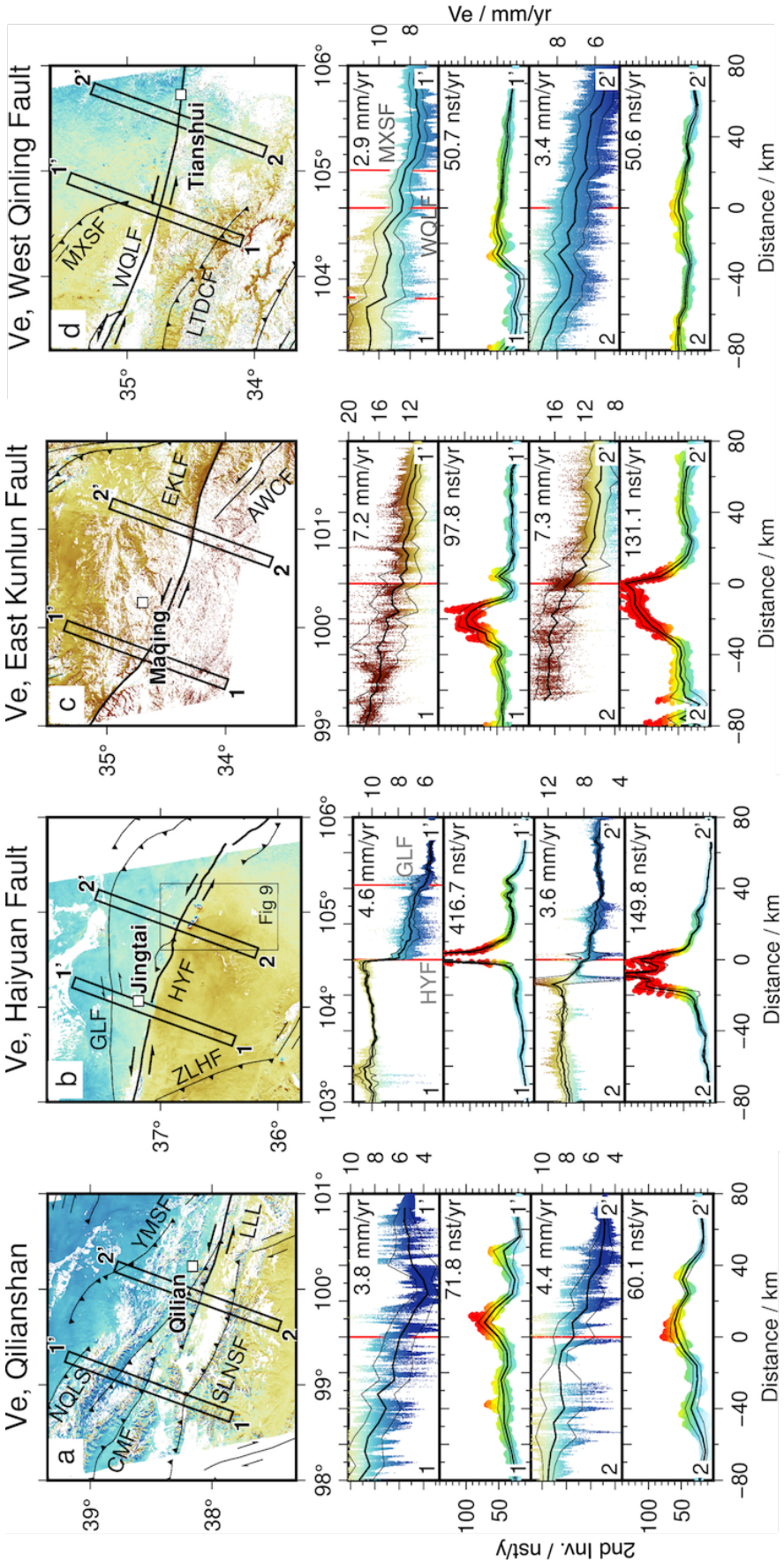

Figure 6. Comparison between full-resolution V_E and second invariant of horizontal strain rate profiles across (a) the Qilianshan thrusts, (b) the Haiyuan Fault (HYF) and the Gulang Fault (GLF), (c) the East Kunlun Fault (EKLF), and (d) the West Qinling Fault (WQLF). Peak strain and the V_E velocity differences between the mean velocity at the ends of the profiles are labelled in each profile panel. Thick and thin black lines on the profiles show median and standard deviations calculated for each 1 km bin. NQLS = North Qilianshan Fault; YMSF = Yumushan Fault; CMF = Changma Fault; SLNSF = Shulunanshan Fault; LLL = Lenglongling Fault; ZLHF = Zhuanglanghe Fault; AWCF = Awancang Fault; MXSF = Maxianshan Fault; LTDCF = Lintan-Dangchang Fault.

2017), yet the high-strain segment is three times longer indicates that the earthquake might have induced postseismic creep. The Menyuan Earthquake was a thrust earthquake that occurred on a fault splay attached to the Haiyuan Fault at a depth of 10 km (Y. Li, Jiang, et al., 2016; H. Wang et al., 2017; Y. Zhang et al., 2020). The motion of the pop-up structure might have released normal stress on the Lenglengling Fault thus making stress conditions conducive to creep on the Haiyuan Fault. This postseismic creep might have, in turn, induced a coulomb stress change that promoted the occurrence of the strike-slip M_W6.6 Jan 8 2022 Menyuan Earthquake on the western end of the creeping section. Similarly, the high-strain signal in the southeast corner of Fig 7a is associated with the 2017 M_S 7.0 Jiuzhaigou Earthquake and associated post-earthquake deformation.

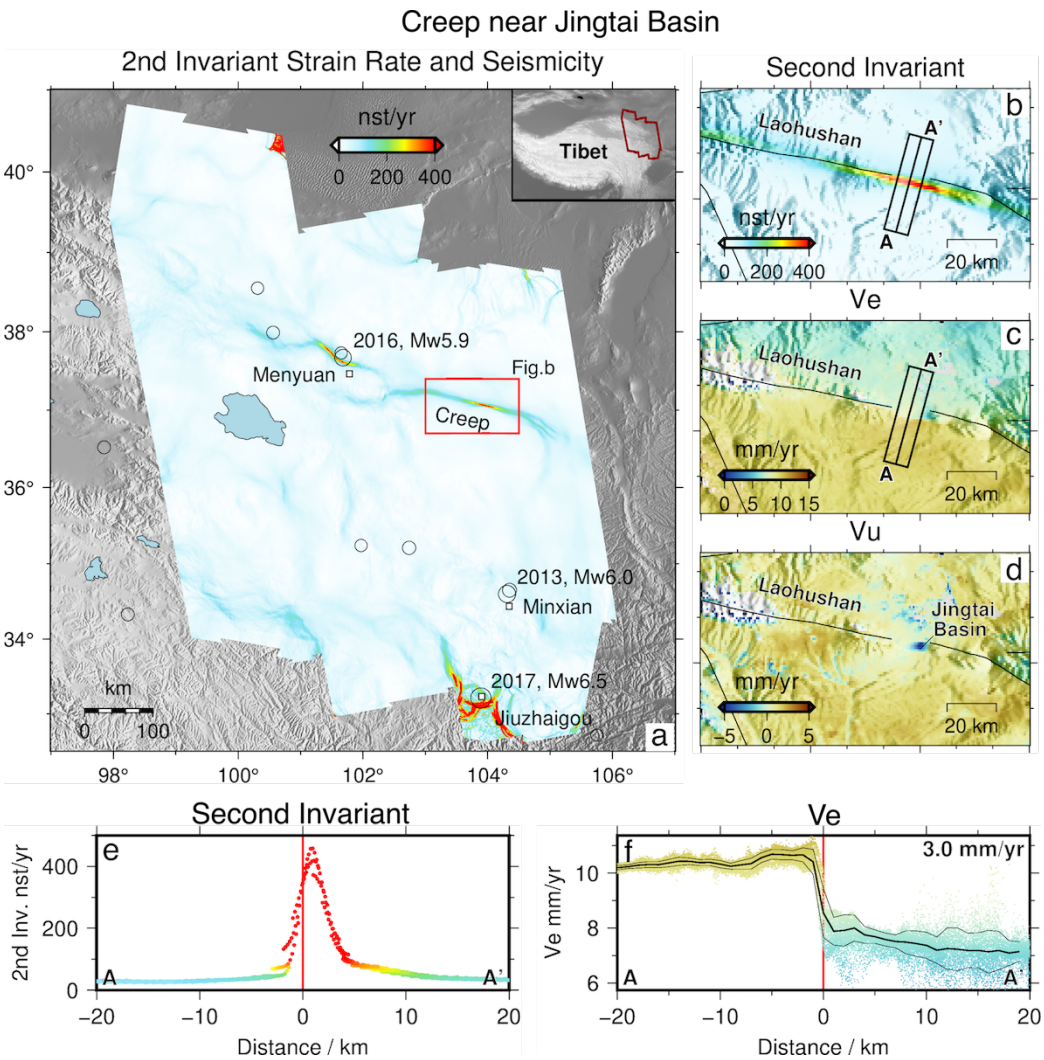

Figure 7. (a) Second invariant of horizontal strain rate. Circles show M_W>5 earthquakes that occurred between 2012 and 2020 from the Global Centroid Moment Tensor Catalogue (Dziewonski et al., 1981), with sizes scaled by magnitude. Event year and magnitude with M_W>5.5 are labeled. (b) Zoomed-in view of the strain rate second invariant for the region indicated with the red box in (a), showing the Laohushan creeping section. Panels (c) and (d) are V_E and V_U maps for the same region. (e) shows the A-A' profile from (b). (f) shows the A-A' profile from (c).

6.5 Shear Strain on the Eastern Extension of the Dabanshan Fault

Fig 8 shows a close-up view of the region around the the central portion of the Haiyuan Fault that highlights elevated maximum shear strain on a fault branch to the south of and parallel to the Lenglongling Fault. The associated velocity step that is clearly visible in both map and profile views indicate relative motion of ~ 2 mm/yr on the eastern extension of the Dabanshan Fault (Fig 8c). The surface trace of this fault is from China's Seismic Active Fault Survey Data Center and is labeled as a Holocene fault, possibly because of the 1929 M5.5 historical earthquake that occurred just to the south (`https://activefault-datacenter.cn/`) (Xu et al., 2016). How and whether this segment connects with the rest of the fault system is not well constrained due to the sparse InSAR data coverage across the mountains (Fig 8f). However, if the Dabanshan and the Haiyuan Faults are connected and capable of rupturing simultaneously, they pose a previously unrecognized and elevated seismic hazard to the region.

6.6 Strain Concentration near the Eastern Termination of the Haiyuan Fault

Additional intriguing features include three high shear strain rate fingers and an arcuate-shaped concentration of contractional strain on the west flank of the Quwu Shan near the eastern termination of the Haiyuan fault (Fig 9a). This feature starts from the east flank of the Hasishan on the Haiyuan Fault and extends from a southern branch (Fig 9b) of the main fault which is commonly believed to be an active fault that did not rupture during the 1920 Haiyuan Earthquake (Cavalié et al., 2008; C. Li et al., 2009; Ren et al., 2016; Matrau et al., 2019; Yao et al., 2019; Ou et al., 2020). Deng et al. (1986) and Gaudemer et al. (1995) suggested the branch extends southeastwards and connects with an oblique reverse fault on the southwestern flank of the Quwu Shan (mapped in Fig 9b) to form a subordinate fault strand in the Haiyuan Fault Zone. However, we do not observe a velocity gradient or elevated strain across the southwestern flank of Quwu Shan. Instead, a V_E gradient and a strong contraction signal exist along the near north-south trending valley between the Yellow River and the Quwu Shan (Fig 9a,d,f). The V_U map also shows a velocity step across the two sides of the valley, with the west uplifting relative to the east, ignoring the subsidence signals along the valley which correspond to the farmlands near villages and are likely caused by water extraction for irrigation (Fig 9e,f, see similar subsidence patterns discussed in Section 6.7.3). This motion might have created the topographic step visible on the hill shade map along the contractional feature (Fig 9c). This is most noticeable near Gaowanxiang, where the westernmost 1 km of an otherwise west-dipping coalesced alluvial fan surface (bajada) is tilted to the east (Fig 9f), diverting the local drainage (Fig 9c). We interpret the signal as a growing fold or a young blind west-dipping thrust fault that, together with the series of thrusts and folds oriented subparallel to the Liupanshan, helps absorb the termination of the left-lateral motion on the Haiyuan Fault (Duvall & Clark, 2010). The localisation of the contractional strain here also suggests that the Longzhong basin block, which is bounded by the Haiyuan, Liupanshan, West Qinling, Maxianshan and Zhuanglanghe Faults (Fig 4a) (e.g. X. Li et al., 2021), might not be as rigid as previously thought (Y. Wang et al., 2017; W. Wang et al., 2017).

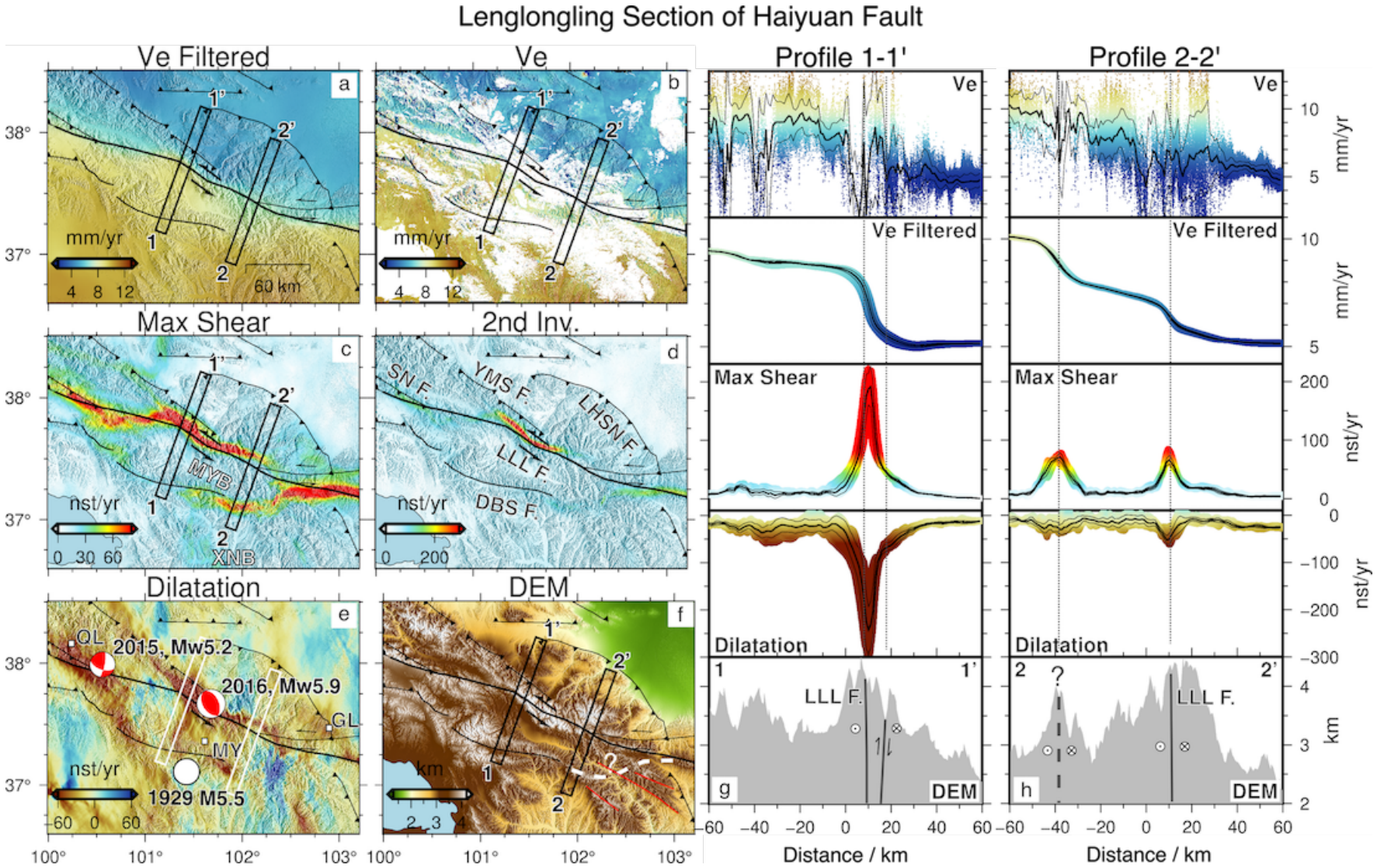

Figure 8. Maps over and profiles across the Lenglongling Section of the Haiyuan Fault. (a) V_E median filtered with a window size of 60 km. (b) full-resolution V_E, (c) Maximum shear strain rate showing shear on a parallel branch to the south of Lenglongling Fault, (d) Second invariant of strain rate, plotted with a different colour scale, showing signal that possibly represents post-seismic creep. (e) Dilatation rate showing contraction signals at fault junctions and focal mechanisms of a 2015 Nov 22 Mw 5.2 oblique strike-slip earthquake and the 2016 Jan 21 Menyuan Earthquake. (f) Topography over the fault branches around the Lenglongling segment of the Haiyuan Fault. (g) Profile 1-1' and (h) profile 2-2' with full-resolution V_E, filtered V_E, maximum shear, dilatation and topography data extracted from (b), (a), (c), (e), and (f). County names: GL=Gulang, QL=Qilian, MY=Menyuan. Fault names: LHSN=Lianhuashannan, YMS=Yumushan, SH=Sunan, LLL=Lenglongling, DBS=Dabanshan, RYS=Riyueshan. Basin names: MYB=Menyuan Basin, XNB=Xining Basin. Dashed lines in (f) and (h) mark a potential fault suggested by the shear strain, though its location in (f) is only weakly constrained by the sparse V_E pixels around this feature. Alternative fault geometry from (J. Zhang et al., 2009) is plotted in (f) in red for comparison.

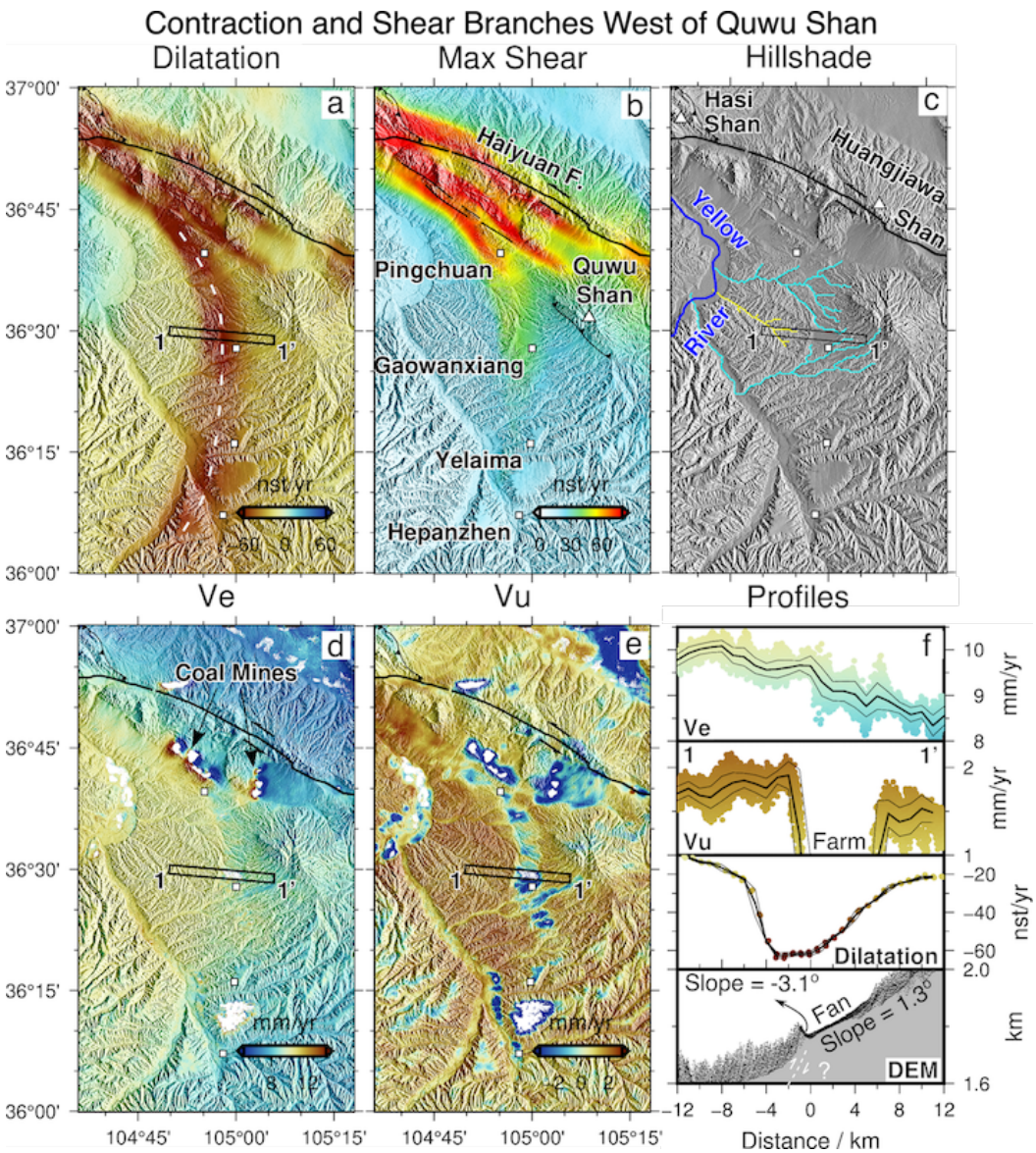

Figure 9. Maps and profiles showing contraction and shear branches that stem from the Haiyuan Fault west of the Quwu Shan. (a) Dilatation, (b) maximum shear strain rate, (c) hillshade of 3-arcsecond digital elevation model from Shuttle Radar Topography Mission (Farr et al., 2007) with diverted streams highlighted in cyan, (d) V_E, (e) V_U where "Farm" indicates farmland and (f) profiles showing a tilted alluvial fan surface collocated with contractional strain and V_E and V_U gradients.

6.7 Vertical Motions from Climatic, Hydrological and Anthropogenic Processes

Unlike the V_E map, which undoubtedly primarily reflects active tectonics, we do not see much correspondence between vertical deformation patterns and the surface fault geometry (Fig 4a-b). Instead, we observe a first order correlation between vertical motion and topography. In the high plateau, the V_U maps is dominated by subsidence. In the lowland, the V_U signal is dominated by uplift. The short-wavelength variations in

vertical motion compared to V_E suggests the source of the vertical motions are likely shallow and mostly driven by surface or near-surface processes. By comparing V_U with Esri's 2020 land cover map (Fig S20)(Karra et al., 2021), we find strong correlations between V_U and three hydrology-related land cover classes, despite the low percentage of these pixels compared to the overall map. Water (mostly along river courses) and flooded vegetation generally correspond to uplift (V_U = 1.3±2.2 mm/yr), and snow/ice corresponds to subsidence (V_U = -2.5±2.9 mm/yr).

6.7.1 Subsidence of Permafrost-Rich Qilianshan

Pixels classified as snow/ice are mostly in the peaks of Qilianshan (Fig S20), east of where Daout et al. (2020) observed active-layer freeze and thaw cycles and widespread subsidence interpreted as ice-loss. We compare our V_U map with the permafrost zonation index (PZI) map from Gruber (2012), which is an estimate of the degree to which permafrost exists in a region. High PZI means permafrost is expected nearly everywhere, whereas low PZI means permafrost likely exists only in the most favorable conditions (Gruber, 2012). We find that the area of strong subsidence in the Qilianshan, where $V_U <$ -2 mm/yr, matches the area where PZI > 0.5 (Fig 10a,c), suggesting that isotropic thaw subsidence might also span this region of the Tibetan Plateau (Zou et al., 2017; Bibi et al., 2018; Cao et al., 2019; Gao et al., 2021; J. Wang et al., 2021; J. Chen et al., 2022).

6.7.2 Uplift from Blocked Drainage

Significant local uplift is detected to the east of Jiuquan, to the north of Jinchang, to the east of Maqu and to the east of Guide cities (Fig 4b). If we compare regions where V_U>1.8 mm/yr to the topography, we find that the rapidly uplifting regions correspond to locations where drainage is blocked by topographic barriers (Fig 10d,e,g,i). The patch near Jiuquan is drained by the Beida and Black Rivers as well as the numerous alluvial fans on the northeast slope of the Qilianshan (Fig 10d). The outlet is blocked by the Jintanan Shan and Heli Shan in the north such that the water is ponding in front of the the linear ridge. Similarly, the triangular patch to the north of Jinchang sits in the Chaoshui Basin, where an endorheic river drained from the northwest terminates. This region is sandwiched between the alluvial fans stemming from the Beida Shan in the north and Longshou Shan in the south, collecting water from two almost opposite azimuths (Fig 10e). The same is true for the fast uplift rates in the Gonghe Basin (Fig 10a-c), where the melt water from the permafrost-rich peaks in the west fails to reach the Yellow River and stalls in a local topographic minimum. Further south, high V_U values are observed in the Zoige Basin to the east of Maqu where the White and Black Rivers join the Yellow River and the Yellow River makes a U-turn in front of the Min and East Kunlun Mountains. This is also where pixels classified as flooded vegetation are clustered (Fig 10f), consistent with the wetland environment of the Zoige Basin (B. Li et al., 2014). As the Yellow River enters the Xunhua Basin (Fig 10h,i), the outflow is again blocked by the N-S trending Jishi Shan such that the entire eastern half of the Xunhua Basin shows rapid uplift rates. The locations of rapid uplift relative to drainage and topography suggests a clear hydrological origin of the uplifting signals. Further work is required to determine whether this is a manifestation of poroelastic expansion of the soil or the cumulative effect of phase bias due to systematic changes in soil properties. One way or another, this phenomena requires a water mass increase likely linked to increases in surface air temperature and precipitation, melting of glaciers and thawing of ice-rich permafrost (e.g. Bibi et al., 2018).

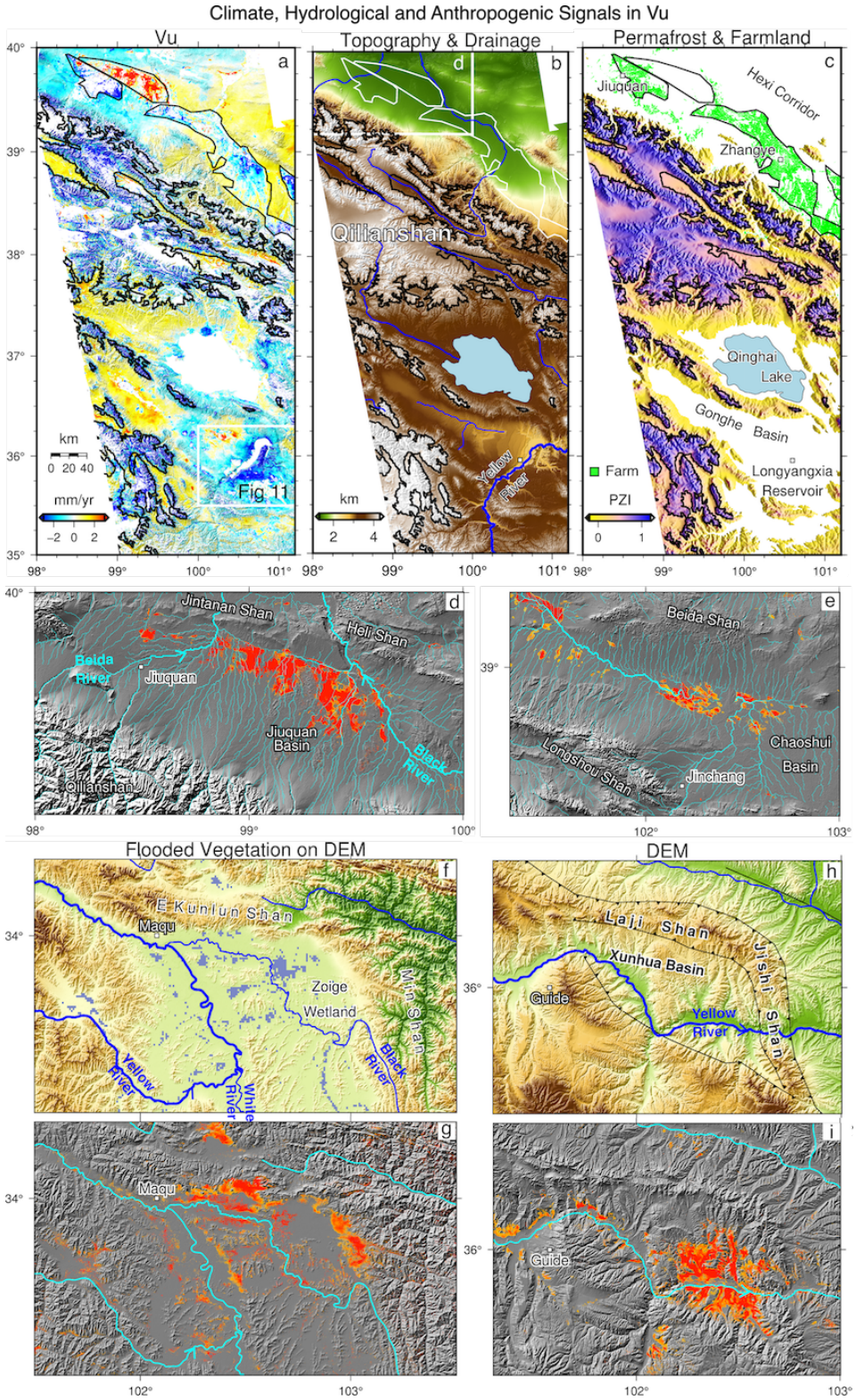

Figure 10. Interpretations of V_U signals in (a-c) the Qilianshan, (d, e) the Hexi Corridor, (f, g) the Zoige Basin, and (h, i) the Xunhua Basin. See location of (d) in panel (b) and locations of (e), (f) and (h) in Fig 4b. (a) V_U, (b) 3-arcsecond digital elevation model (DEM) from Shuttle Radar Topography Mission, (c) Permafrost Zonation Index (PZI) (Gruber, 2012) map and farmland (crops) in ESRI's global land cover map (Karra et al., 2021). Black lines in (a-c) outline the PZI=0.5 contour in the Qilianshan and the boundaries of the anomalous uplift and subsidence signals in the Hexi Corridor. (d, e, g, i) show pixels with V_U>1.8 mm/yr on top of hill shade with drainage data from Generic Mapping Tools (Wessel et al., 2013) and HydroRIVERS data set (available at `https://www.hydrosheds.org`) (Lehner & Grill, 2013). (f) shows permanents rivers and flooded vegetation pixels in purple (Karra et al., 2021) on top of topography. (h) shows faults and permanent rivers on top of topography.

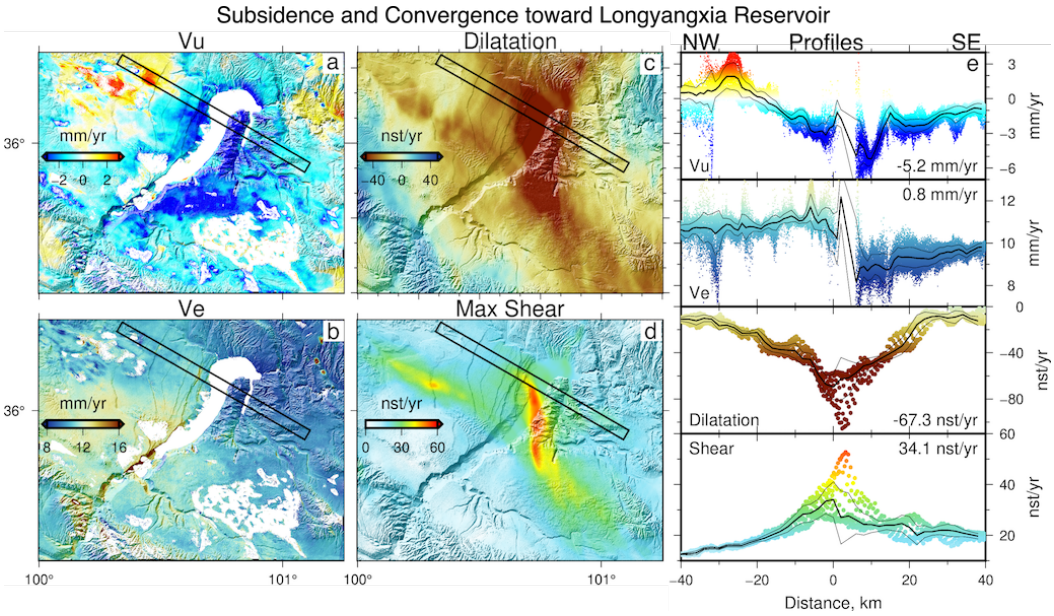

Figure 11. (a) V_U, (b) V_E, (c) dilatation rate and (d) maximum shear rate maps of the Longyangxia Reservoir. (e) Profiles from (a-d) showing subsidence around and convergence towards the center of the reservoir causing dilatation and shear in the area. Thick and thin lines mark binned mean and standard deviations along profiles. Labels on each profile show lowest mean V_U, difference in mean V_E on the edges of the profile, lowest mean dilatation and highest mean maximum shear.

6.7.3 Subsidence of farmlands in the Hexi Corridor

Patches of subsidence are observed along the Hexi Corridor to the north of the permafrost zone (Fig 10a,c). The spatial coverage of the subsidence signals corresponds to farmland near the major cities of Jiuquan, Zhangye, Jinchang and Wuwei (Fig 4b, Fig 10c). We attribute the subsidence to rapid groundwater extraction for irrigation which is common practice in the arid northwest of China, where the loss of groundwater storage has long been a known issue (He et al., 2012; X. Zhang et al., 2018; Wu et al., 2019). The fastest subsiding crop areas are those to the east of Jinchang and to the north of Wuwei (Fig 4), where V_U<-10 mm/yr are observed.

6.7.4 Subsidence around the Longyangxia Reservoir

The moon-shaped empty patch to the south of the Qinghai Lake is the Longyangxia Reservoir (Fig 10a, Fig 11), and is at the center of a subsiding region. The subsidence signal is strongest at the thin strip of land in the head of the hook-shaped water body, with a subsidence rate of ∼5.2 mm/yr (Fig 11e). The subsidence rate decreases away from the reservoir over a wavelength of >20 km on each side, typical of the length scale of elastic deformation of the upper crust (Doin et al., 2015). The V_E profile shows a step that is greater just adjacent to the reservoir and smaller further away, suggesting material is being pulled towards the center of subsidence. Therefore, we interpret subsidence as a result of the gravitational loading from the water column, in response to a ∼20 m overall increase in water level detected between 2017 and 2020 (Zhao et al., 2022). This water load might have been established prior to 2017 and caused convergence of the surrounding crust and hence the contraction observed (Fig 11c). The source of the shear strain is unclear (Fig 11c,d). One possible explanation is that the interpolated GNSS V_N

field is not of high-enough resolution to capture this short-wavelength variation, hence the V_N gradients cannot balance the V_E gradients in the evaluation of the maximum shear rate.

6.7.5 Large-scale Regional Uplift

Focusing only on regions where the the absolute value of V_U is less than than 2 mm/yr (i.e., ignoring non-tectonic deformation) highlights large-scale, regional uplift northward of the West Qinling Fault, across the Haiyuan Fault, along most of the Hexi Corridor, as well as in the lens-shaped valleys between the Qilian ranges and the low-relief plains to the west of Qinghai Lake (Fig 4b). Whilst the bedrock vertical motions in the high plateaus are still mixed and uncertain, we can see a broad-scale uplifting signal across the low-lying northeast half of the study region (compare Fig 1a and Fig 4b). The uplift is relative to the average V_U velocities of three reference GNSS stations in Ordos Plateau, Gobi-Alashan and Mongolia chosen by Liang et al. (2013) in the stable northern neighbours reference frame. Therefore, the observation is consistent with a picture of northward growth of topography as inferred by the new-found activity on the thrusts in Heli Shan to the north of the Hexi Corridor measured by W. J. Zheng et al. (2013).

7 Conclusions

In this study, we have derived ∼100 m resolution V_E and V_U maps at ∼ 1 mm/yr uncertainty levels and three ∼1 km resolution strain rate maps covering 440,000 km^2 of the NE Tibetan Plateau. We developed new methods for mosaicing frame-based LOS velocity maps into regional velocity maps, deriving Cartesian (i.e., north-south, east-west, and vertical) velocities, and deriving high-resolution strain rate maps from the velocity fields that preserve the rich and detailed information contained in the dense geodetic data sets. The resulting V_E and V_U maps highlight for the first time at a large scale tightly focused left-lateral, strike-slip deformation across the major Haiyuan and East Kunlun fault system, and an outward growth of topography to the north-east of the Tibetan plateau. The second-invariant of the horizontal strain-rate tensor shows that half of the total horizontal strain rate is accumulating on those major structures. Shear strain rate helps delineate the extent of the major strike-slip faults, with a mix of both localised and distributed deformation as a result of fault geometry and slip partitioning. Dilatational and compressional strains are observed between Qilianshan thrusts and on fault junctions, such as where the Haiyuan Fault branches into neighboring strike-slip and thrust faults and where the Awancang strike-slip fault merges into the East Kunlun Fault, highlighting the local volumetric changes within zones of complex fault geometry. The high-resolution strain rate maps also aid in identifying fault segments that are creeping at the surface and previously unknown active faults. The Laohushan creeping section of the Haiyuan Fault is mapped to be 30 km long across both the Laohushan with an average creep rate of ∼3 mm/yr, which is >20% lower than the creep rate reported in previous studies. High shear-strain rates are also observed along the Lenglongling section of the Haiyuan Fault, potentially induced by postseismic creep following the 2016 Menyuan Earthquake. The eastward motion of the eastern half of the Menyuan Basin also appears to be decoupled from that in the Xining Basin, causing shear strain to accumulate on the eastern extension of Dabanshan Fault. Strong north-south-trending contraction is identified on the western flank of the Quwushan, in agreement with a back-tilted alluvial fan surface. The V_U map reveals rapid subsidence across the permafrost-rich Qilianshan due to large-scale ice loss, at the oases along the Hexi Corridor due to the extraction of groundwater for irrigation, and around the Longyangxia Reservoir due to gravitational loading from the increasing water level. Small-scale uplifts are also observed at the Jiuquan, Chaoshui, Zoige and Xunhua Basins where river drainage hits topographic barriers. With the ongoing expansion of global InSAR data processing and coverage, high-resolution velocity and strain rate maps like those shown here will play an increasingly important role

in measuring active fault deformation, detecting unknown and creeping faults, advancing our understanding of the regional and global seismic hazard caused by active faults and characterization of climatic, hydrologic and anthropogenic-related processes alike.

Acknowledgments

We would like to thank the European Space Agency for the open data policy on the Sentinel-1 mission. This study was funded by the Natural Environment Research Council (NERC) through the 'Looking inside the Continents from Space (LiCS)' large grant (NE/K011006/1), the Centre for the Observation and Modelling of Earthquakes, Volcanoes and Tectonics (COMET), a partnership between UK Universities and the British Geological Survey, and the 'Earthquakes without Frontiers (EwF)' consortium (NE/J01978X/1). Qi Ou has been supported by scholarships and awards from China Scholarship Council-Pacific Alliance Group Oxford Scholarship and Great Britain-China Educational Trust. LiCSAR data contains modified Copernicus Sentinel data [2014-2019] analysed by the COMET-LiCSAR team; we thank Yasser Maghsoudi for his support. LiCSAR processing is carried out at JASMIN, the UK's collaborative data analysis facility for environmental science (http://jasmin.ac.uk) hosted at the Centre for Environmental Data Analysis (CEDA).

We thank Jérôme Lavé for helpful discussions on the geomorphologic observations that corroborated our interpretation of strain features. Figures were plotted using the Generic Mapping Tools Version 6 (Wessel et al., 2019) and Python.

Data Availability Statement

The original interferograms are available on COMET-LiCS portal (https://comet.nerc.ac.uk/comet-lics-portal/). Archiving of our derived line-of-sight and decomposed velocities is underway. These data will be made available at CEDA archive and can temporarily be accessed from Supporting Information for review purposes.

References

Ansari, H., De Zan, F., & Parizzi, A. (2020). Study of Systematic Bias in Measuring Surface Deformation with SAR Interferometry. *IEEE Transactions on Geoscience and Remote Sensing*(December), 1–12. doi: 10.1109/TGRS.2020.3003421

Bekaert, D. P., Biessel, R., Havazli, E., Hua, H., Karim, M., Lai-Norling, J., ... Zhang, A. (2020, December). New and upcoming developments of standardized InSAR Products by the Advanced Rapid Imaging and Analysis (ARIA) Project for Natural Hazards. In *Agu fall meeting abstracts* (Vol. 2020, p. G004-0038).

Bhat, H. S., Olives, M., Dmowska, R., & Rice, J. R. (2007). Role of fault branches in earthquake rupture dynamics. *Journal of Geophysical Research: Solid Earth*, *112*(11), 1–16. doi: 10.1029/2007JB005027

Bibi, S., Wang, L., Li, X., Zhou, J., Chen, D., & Yao, T. (2018). Climatic and associated cryospheric, biospheric, and hydrological changes on the Tibetan Plateau: a review. *International Journal of Climatology*, *38*(January), e1–e17. doi: 10.1002/joc.5411

Biggs, J., Wright, T., Lu, Z., & Parsons, B. (2007). Multi-interferogram method for measuring interseismic deformation: Denali Fault, Alaska. *Geophysical Journal International*, *170*(3), 1165-1179. doi: 10.1111/j.1365-246X.2007.03415.x

Burgmann, R., Rosen, P. A., & Fielding, E. J. (2000). SYNTHETIC APERTURE RADAR INTERFEROMETRY TO MEASURE EARTH'S SURFACE TOPOGRAPHY AND ITS DEFORMATION. *Annu. Rev. Earth Planet. Sci.*, *28*, 169–209.

Cao, B., Zhang, T., Wu, Q., Sheng, Y., Zhao, L., & Zou, D. (2019). Permafrost zonation index map and statistics over the Qinghai–Tibet Plateau based on field evidence. *Permafrost and Periglacial Processes*, *30*(3), 178–194. doi: 10.1002/ppp.2006

Cavalié, O., Lasserre, C., Doin, M. P., Peltzer, G., Sun, J., Xu, X., & Shen, Z. K. (2008). Present-day deformation across the Haiyuan fault (Gansu, China), measured by SAR interferometry. *European Space Agency, (Special Publication)*(655).

CEA-PBED, C. E. A. E. D. P. B. (1995). *China Historical Strong Earthquake Catalogue (BC23-AD1911).*

Chen, C. W., & Zebker, H. A. (2002). Phase unwrapping for large SAR interferograms: Statistical segmentation and generalized network models. *IEEE Transactions on Geoscience and Remote Sensing*, *40*(8), 1709–1719. doi: 10.1109/TGRS.2002.802453

Chen, J., Wu, T., Zou, D., Liu, L., Wu, X., Gong, W., ... Yang, S. (2022). Magnitudes and patterns of large-scale permafrost ground deformation revealed by Sentinel-1 InSAR on the central Qinghai-Tibet Plateau. *Remote Sensing of Environment*, *268*(October 2021), 112778. Retrieved from `https://doi.org/10.1016/j.rse.2021.112778` doi: 10.1016/j.rse.2021.112778

Daout, S., Dini, B., Haeberli, W., Doin, M. P., & Parsons, B. (2020). Ice loss in the Northeastern Tibetan Plateau permafrost as seen by 16 yr of ESA SAR missions. *Earth and Planetary Science Letters*, *545*, 116404. doi: 10.1016/j.epsl.2020.116404

Daout, S., Doin, M. P., Peltzer, G., Lasserre, C., Socquet, A., Volat, M., & Sudhaus, H. (2018). Strain Partitioning and Present-Day Fault Kinematics in NW Tibet From Envisat SAR Interferometry. *Journal of Geophysical Research: Solid Earth*, *123*(3), 2462–2483. doi: 10.1002/2017JB015020

Daout, S., Doin, M.-P., Peltzer, G., Socquet, A., & Lasserre, C. (2017). Large-scale InSAR monitoring of permafrost freeze-thaw cycles on the Tibetan Plateau. *Geophysical Research Letters*, *44*(2), 901-909. doi: 10.1002/2016GL070781

Daout, S., Jolivet, R., Lasserre, C., Doin, M. P., Barbot, S., Tapponnier, P., ... Sun, J. (2016). Along-strike variations of the partitioning of convergence across the Haiyuan fault system detected by InSAR. *Geophysical Journal International*, *205*(1), 536–547. doi: 10.1093/gji/ggw028

Daout, S., Sudhaus, H., Kausch, T., Steinberg, A., & Dini, B. (2019). Interseismic and Postseismic Shallow Creep of the North Qaidam Thrust Faults Detected with a Multitemporal InSAR Analysis. *Journal of Geophysical Research: Solid Earth*, *124*(7), 7259–7279. doi: 10.1029/2019JB017692

Deng, Q., Chen, S., Song, F., Zhu, S., Wang, Y., Zhang, W., ... Zhang, P. (1986). Variations in the geometry and amount of slip on the Haiyuan (Nanxihaushan) Fault zone, China and the surface rupture of the 1920 Haiyuan earthquake. In *Haiyuan fault zone* (pp. 169–182). doi: 10.1029/GM037p0169

Deng, Q., Sung, F., Zhu, S., Li, M., Wang, T., Zhang, W., ... Zhang, P. (1984). Active faulting and tectonics of the Ningxia-Hui Autonomous Region, China. *Journal of Geophysical Research*, *89*(10), 4427–4445. doi: 10.1029/JB089iB06p04427

Doin, M. P., Twardzik, C., Ducret, G., Lasserre, C., Guillaso, S., & Jianbao, S. (2015). InSAR measurement of the deformation around Siling Co Lake: Inferences on the lower crust viscosity in central Tibet. *Journal of Geophysical Research: Solid Earth*, *120*(7), 5290–5310. doi: 10.1002/2014JB011768

Duvall, A. R., & Clark, M. K. (2010). Dissipation of fast strike-slip faulting within and beyond northeastern Tibet. *Geology*, *38*(3), 223–226. doi: 10.1130/G30711.1

Dziewonski, A. M., Chou, T.-A., & Woodhouse, J. H. (1981). Determination of earthquake source parameters from waveform data for studies of global and

regional seismicity. *Journal of Geophysical Research: Solid Earth*, *86*(B4), 2825-2852. doi: 10.1029/JB086iB04p02825

Ekström, G., Nettles, M., & Dziewoński, A. (2012). The global CMT project 2004–2010: Centroid-moment tensors for 13,017 earthquakes. *Physics of the Earth and Planetary Interiors*, *200-201*, 1 - 9. doi: 10.1016/j.pepi.2012.04.002

Elliott, J. R., Walters, R. J., & Wright, T. J. (2016). The role of space-based observation in understanding and responding to active tectonics and earthquakes. *Nature Communications*, *7*, 1–16. doi: 10.1038/ncomms13844

England, P., & Houseman, G. (1985). Role of lithospheric strength heterogeneities in the tectonics of Tibet and neighbouring regions. *Nature*, *315*(6017), 297–301. doi: 10.1038/315297a0

England, P., & Molnar, P. (1997). Active deformation of Asia: From kinematics to dynamics. *Science*, *278*(5338), 647–650. doi: 10.1126/science.278.5338.647

Farr, T. G., Rosen, P. A., Caro, E., Crippen, R., Duren, R., Hensley, S., ... Alsdorf5, D. (2007). The Shuttle Radar Topography Mission. *Reviews of Geophysics*, *45*(RG2004), 1–33. doi: 10.1029/2005RG000183

Fattahi, H., & Amelung, F. (2014, 08). InSAR uncertainty due to orbital errors . *Geophysical Journal International*, *199*(1), 549-560. doi: 10.1093/gji/ggu276

Flesch, L. M., Haines, A. J., & Holt, W. E. (2001). Dynamics of the India-Eurasia collision zone. *JOURNAL OF GEOPHYSICAL RESEARCH*, *106*(B8), 16435–16460. Retrieved from 10.1029/2001JB000208

Gan, W., Zhang, P., Shen, Z. K., Niu, Z., Wang, M., Wan, Y., ... Cheng, J. (2007). Present-day crustal motion within the Tibetan Plateau inferred from GPS measurements. *Journal of Geophysical Research: Solid Earth*, *112*(8), 1–14. doi: 10.1029/2005JB004120

Gao, T., Zhang, Y., Kang, S., Abbott, B. W., Wang, X., Zhang, T., ... Gustafsson, O. (2021). Accelerating permafrost collapse on the eastern Tibetan Plateau. *Environmental Research Letters*, *16*(5). doi: 10.1088/1748-9326/abf7f0

Gaudemer, Y., Tapponnier, P., Meyer, B., Peltzer, G., Shunmin, G., Zhitai, C., ... Cifuentes, I. (1995). Partitioning of crustal slip between linked, active faults in the eastern Qilian Shan, and evidence for a major seismic gap, the 'Tianzhu gap', on the western Haiyuan Fault, Gansu (China). *Geophysical Journal International*, *120*(3), 599–645. doi: 10.1111/j.1365-246X.1995.tb01842.x

Gomba, G., Rodriguez Gonzalez, F., & De Zan, F. (2017). Ionospheric phase screen compensation for the Sentinel-1 TOPS and ALOS-2 ScanSAR modes. *IEEE Transactions on Geoscience and Remote Sensing*, *55*(1), 223–235. doi: 10.1109/TGRS.2016.2604461

Gruber, S. (2012). Derivation and analysis of a high-resolution estimate of global permafrost zonation. *Cryosphere*, *6*(1), 221–233. doi: 10.5194/tc-6-221-2012

Haines, A. J., Dimitrova, L. L., Wallace, L. M., & Williams, C. A. (2015). Introduction to the Vertical Derivatives of Horizontal Stress (VDoHS) Rates. , 9–18. doi: 10.1007/978-3-319-21578-5_2

Haines, A. J., & Holt, W. E. (1993). A procedure for obtaining the complete horizontal motions within zones of distributed deformation from the inversion of strain rate data. *Journal of Geophysical Research*, *98*(B7). doi: 10.1029/93jb00892

Haines, A. J., & Wallace, L. M. (2020). New Zealand-Wide Geodetic Strain Rates Using a Physics-Based Approach. *Geophysical Research Letters*, *47*(1). doi: 10.1029/2019GL084606

Han, L., Liu-Zeng, J., Yao, W., Shao, Y., Yuan, Z., & Wang, Y. (2021). Coseismic slip gradient at the western terminus of the 1920 Haiyuan Mw 7.9 earthquake. *Journal of Structural Geology*, *152*(March), 104442. doi: 10.1016/j.jsg.2021.104442

He, J., Ma, J., Zhang, P., Tian, L., Zhu, G., Mike Edmunds, W., & Zhang, Q.

(2012). Groundwater recharge environments and hydrogeochemical evolution in the Jiuquan Basin, Northwest China. *Applied Geochemistry*, *27*(4), 866–878. doi: 10.1016/j.apgeochem.2012.01.014

Hussain, E., Wright, T. J., Walters, R. J., Bekaert, D. P. S., Lloyd, R., & Hooper, A. (2018). Constant strain accumulation rate between major. *Nature Communications*, *9*(1392), 1–9. doi: 10.1038/s41467-018-03739-2

Institute of Geology. (1990). *Active Haiyuan Fault Zone Monograph* . Seismological Publishing House, Beijing, China.

ISC, (International Seismological Centre). (2019). *ISC-GEM Earthquake Catalogue, http://doi.org/10.31905/D808B825.*

Jolivet, R., Candela, T., Lasserre, C., Renard, F., Klinger, Y., & Doin, M. P. (2015). The burst-like behavior of aseismic slip on a rough fault: The creeping section of the Haiyuan fault, China. *Bulletin of the Seismological Society of America*, *105*(1), 480–488. doi: 10.1785/0120140237

Jolivet, R., Lasserre, C., Doin, M.-P., Guillaso, S., Peltzer, G., Dailu, R., ... Xu, X. (2012). Shallow creep on the Haiyuan Fault (Gansu, China) revealed by SAR Interferometry. *Journal of Geophysical Research*, *117*. doi: 10.1029/2011JB008732

Jolivet, R., Lasserre, C., Doin, M. P., Peltzer, G., Avouac, J. P., Sun, J., & Dailu, R. (2013). Spatio-temporal evolution of aseismic slip along the Haiyuan fault, China: Implications for fault frictional properties. *Earth and Planetary Science Letters*, *377-378*, 23–33. doi: 10.1016/j.epsl.2013.07.020

Karra, K., Kontgis, C., Statman-Weil, Z., Mazzariello, J., Mathis, M., & Brumby, S. (2021). Global land use/land cover with Sentinel-2 and deep learning. In *Igarss 2021-2021 ieee international geoscience and remote sensing symposium. ieee.*

King, G., & Nábělek, J. (1985). Role of fault bends in the initiation and termination of earthquake rupture. *Science*, *228*(4702), 984–987. doi: 10.1126/science.228.4702.984

Kirby, E., Harkins, N., Wang, E., Shi, X., Fan, C., & Burbank, D. (2007). Slip rate gradients along the eastern Kunlun fault. *Tectonics*, *26*(2), 1–16. doi: 10.1029/2006TC002033

Kreemer, C., Blewitt, G., & Klein, E. C. (2014). A geodetic plate motion and Global Strain Rate Model. *Geochemistry, Geophysics, Geosystems*, *15*, 3849–3889. doi: 10.1002/2014GC005407

Lazecký, M., Spaans, K., González, P. J., Maghsoudi, Y., Morishita, Y., Albino, F., ... Wright, T. J. (2020). LiCSAR: An Automatic InSAR Tool for Measuring and Monitoring Tectonic and Volcanic Activity. *Remote Sensing*, *12*(15), 2430. doi: 10.3390/rs12152430

Lehner, B., & Grill, G. (2013). Global river hydrography and network routing: baseline data and new approaches to study the world's large river systems. *Hydrological Processes*, *27*(15), 2171–2186. doi: https://doi.org/10.1002/hyp.9740.Dataisavailableatwww.hydrosheds.org.

Li, B., Yu, Z., Liang, Z., Song, K., Li, H., Wang, Y., ... Acharya, K. (2014). Effects of Climate Variations and Human Activities on Runoff in the Zoige Alpine Wetland in the Eastern Edge of the Tibetan Plateau. *Journal of Hydrologic Engineering*, *19*(5), 1026–1035. doi: 10.1061/(asce)he.1943-5584.0000868

Li, C., Zhang, P.-z., Yin, J., & Min, W. (2009). Late Quaternary left-lateral slip rate of the Haiyuan fault, northeastern margin of the Tibetan Plateau. *Tectonics*, *28*(5). doi: 10.1029/2008TC002302

Li, H., Zhang, Y., Dong, S., Zhang, J., Sun, Y., & Wang, Q. (2020). Neotectonics of the Bailongjiang and Hanan faults: New insights into late Cenozoic deformation along the eastern margin of the Tibetan Plateau. *GSA Bulletin*, 1–18. doi: 10.1130/b35374.1

Li, J., Zhang, Y., Li, H., Xiong, J., Li, J., & Wu, T. (2016). Revisiting Late Quaternary Slip-rate along the Maqu Segment of the Eastern Kunlun Fault, North-

east Tibet. *Acta Seismologica Sinica (English Edition)*, *90*(2), 486–502.

Li, X., Pierce, I. K. D., Bormann, J. M., Hammond, W. C., Zhang, Z., Li, C., ... Zhang, P. (2021). Tectonic Deformation of the Northeastern Tibetan Plateau and Its Surroundings Revealed With GPS Block Modeling. *Journal of Geophysical Research: Solid Earth*, *126*(5), 1–15. doi: 10.1029/2020jb020733

Li, Y., Jiang, W., Zhang, J., & Luo, Y. (2016). Space geodetic observations and modeling of 2016 Mw 5.9 Menyuan earthquake: Implications on seismogenic tectonic motion. *Remote Sensing*, *8*(6), 1–11. doi: 10.3390/rs8060519

Li, Y., Nocquet, J. M., Shan, X., & Song, X. (2021). Geodetic Observations of Shallow Creep on the Laohushan-Haiyuan Fault, Northeastern Tibet. *Journal of Geophysical Research: Solid Earth*, *126*(6), 1–18. doi: 10.1029/2020JB021576

Li, Y., Shan, X., Qu, C., & Wang, Z. (2016). Fault locking and slip rate deficit of the Haiyuan-Liupanshan fault zone in the northeastern margin of the Tibetan Plateau. *Journal of Geodynamics*, *102*, 47–57. doi: 10.1016/j.jog.2016.07.005

Liang, S., Gan, W., Shen, C., Xiao, G., Liu, J., Chen, W., ... Zhou, D. (2013). Three-dimensional velocity field of present-day crustal motion of the Tibetan Plateau derived from GPS measurements. *J. Geophys. Res. Solid Earth*, *118*, 5722–5732. doi: 10.1002/2013JB010503

Liu-zeng, J., Shao, Y., Klinger, Y., Xie, K., Yuan, D., & Lei, Z. (2015). Variability in magnitude of paleoearthquakes revealed by trenching and historical records, along the Haiyuan Fault, China. *Journal of Geophysical Research: Solid Earth*, *120*, 8304–8333. doi: DOI:10.1002/2015JB012163

López-Quiroz, P., Doin, M. P., Tupin, F., Briole, P., & Nicolas, J. M. (2009). Time series analysis of Mexico City subsidence constrained by radar interferometry. *Journal of Applied Geophysics*, *69*(1), 1–15. doi: 10.1016/j.jappgeo.2009.02.006

Loveless, J. P., & Meade, B. J. (2010). Geodetic imaging of plate motions, slip rates, and partitioning of deformation in Japan. *Journal of Geophysical Research*, *115*(B2), 1–35. doi: 10.1029/2008jb006248

Matrau, R., Klinger, Y., Woerd, J. V. D., Li, Z., & Xu, X. (2019). Late Pleistocene - Holocene slip rate along the Hasi Shan restraining bend of the Haiyuan fault : implication for faulting dynamics of a complex fault system. *Tectonics*, 0–3. doi: 10.1029/2019TC005488

Maubant, L., Pathier, E., Daout, S., Radiguet, M., Doin, M.-P., Kazachkina, E., ... Walpersdorf, A. (2020). Independent Component Analysis and Parametric Approach for Source Separation in InSAR Time Series at Regional Scale: Application to the 2017–2018 Slow Slip Event in Guerrero (Mexico). *Journal of Geophysical Research: Solid Earth*, *125*(3), e2019JB018187. doi: 10.1029/2019JB018187

McCaffrey, R., King, R. W., Payne, S. J., & Lancaster, M. (2013). Active tectonics of northwestern U.S. inferred from GPS-derived surface velocities. *Journal of Geophysical Research: Solid Earth*, *118*(2), 709–723. doi: 10.1029/2012JB009473

Meade, B. J., & Hager, B. H. (2005). Block models of crustal motion in southern California constrained by GPS measurements. *Journal of Geophysical Research: Solid Earth*, *110*(3), 1–19. doi: 10.1029/2004JB003209

Molnar, P., & Tapponnier, P. (1975). Cenozoic Tectonics of Asia: Effects of a Continental Collision. *Science*, *189*(4201), 419–426.

Morishita, Y., Lazecky, M., Wright, T. J., Weiss, J. R., Elliott, J. R., & Hooper, A. (2020). LiCSBAS: An open-source insar time series analysis package integrated with the LiCSAR automated sentinel-1 InSAR processor. *Remote Sensing*, *12*(3), 5–8. doi: 10.3390/rs12030424

Murphy, B., Müller, S., & Yurchak, R. (2021). *GeoStat-Framework/PyKrige: v1.6.1 (v1.6.1). Zenodo.* doi: https://doi.org/10.5281/zenodo.5380342

Ou, Q., Kulikova, G., Yu, J., Elliott, A., Parsons, B., & Walker, R. (2020). Mag-

nitude of the 1920 Haiyuan Earthquake Reestimated Using Seismological and Geomorphological Methods. *Journal of Geophysical Research: Solid Earth*, *125*(8). doi: 10.1029/2019jb019244

Pagani, C., Bodin, T., Métois, M., & Lasserre, C. (2021). Bayesian Estimation of Surface Strain Rates From Global Navigation Satellite System Measurements: Application to the Southwestern United States. *Journal of Geophysical Research: Solid Earth*, *126*(6), 1–25. doi: 10.1029/2021JB021905

Pichon, X. L., Fournier, M., & Jolivet, L. (1992). Kinematics, topography, shortening , and extrusion in the India-Eurasia collision. *Tectonics*, *11*(6), 1085–1098.

Qiao, X., Qu, C., Shan, X., Zhao, D., & Liu, L. (2021). Interseismic slip and coupling along the haiyuan fault zone constrained by InSAR and GPS measurements. *Remote Sensing*, *13*(16), 1–20. doi: 10.3390/rs13163333

Quigley, M. C., Jiménez, A., Duffy, B., & King, T. R. (2019). Physical and Statistical Behavior of Multifault Earthquakes: Darfield Earthquake Case Study, New Zealand. *Journal of Geophysical Research: Solid Earth*, *124*(5), 4788–4810. doi: 10.1029/2019JB017508

Ren, Z., Zhang, Z., Chen, T., Yan, S., Yin, J., Zhang, P., & Zheng, W. (2016). Clustering of offsets on the haiyuan fault and their relationship to paleoearthquakes. *Bulletin of the Geological Society of America*, *128*(1-2), 3–18. doi: 10.1130/B31155.1

Rousset, B., Jolivet, R., Simons, M., Lasserre, C., Riel, B., Milillo, P., ... Renard, F. (2016). An aseismic slip transient on the North Anatolian Fault. *Geophysical Research Letters*, *43*(7), 3254–3262. doi: 10.1002/2016GL068250

Sandwell, D. T., & Wessel, P. (2016). Interpolation of 2-D vector data using constraints from elasticity. *Geophysical Research Letters*, *43*(10), 10703–10709. doi: 10.1002/2016GL070340

Sathiakumar, S., & Barbot, S. (2021). The stop-start control of seismicity by fault bends along the Main Himalayan Thrust. *Communications Earth & Environment*, *2*(1), 1–11. doi: 10.1038/s43247-021-00153-3

Savage, J. C., Gan, W., & Svarc, J. L. (2001). Strain accumulation and rotation in the Eastern California Shear Zone. *Journal of Geophysical Research: Solid Earth*, *106*(B10), 21995–22007. doi: 10.1029/2000jb000127

Savage, J. C., Burford, R. O. (1973). Savage, J. C., and R. O. Burford. "Geodetic determination of relative plate motion in central California. *Journal of Geophysical Research*, *78*(5), 832–845.

Schwartz, D. P., & Sibson, R. H. (1989). Fault Segmentation and Controls of Rupture Initiation and Termination. *U.S. Geological Survey Open File Report No. 89-315*, 458.

Shao, Y., Liu-zeng, J., Woerd, J. V. D., Klinger, Y., Oskin, M. E., Zhang, J., ... Yao, W. (2020). Late Pleistocene slip rate of the central Haiyuan fault constrained from optically stimulated luminescence , 14 C , and cosmogenic isotope dating and high-resolution topography. , 1–23. doi: 10.1130/B35571.1/5173570/b35571.pdf

Shen, L. (2020). *Characterising Seismic Hazard with InSAR Measurements: cases over large length scales* (Unpublished doctoral dissertation). PhD thesis, University of Leeds.

Shen, L., Hooper, A., & Elliott, J. (2019). A Spatially Varying Scaling Method for InSAR Tropospheric Corrections Using a High-Resolution Weather Model. *Journal of Geophysical Research: Solid Earth*, 1–18. doi: 10.1029/2018JB016189

Shen, L., Hooper, A., Elliott, J., & Wright, T. (2021). Large-scale interseismic deformation along the Altyn Tagh Fault determined from Sentinel-1 InSAR. In *Egu general assembly* (pp. EGU21–10278). doi: https://doi.org/10.5194/egusphere-egu21-10278,2021

Smith, W. H., & Wessel, P. (1990). Gridding with continuous curvature splines in

tension. *Geophysics*, *55*(3), 293–305. doi: 10.1190/1.1442837

Song, X., Jiang, Y., Shan, X., Gong, W., & Qu, C. (2019). A fine velocity and strain rate field of present-day crustal motion of the northeastern Tibetan Plateau inverted jointly by InSAR and GPS. *Remote Sensing*, *11*(4). doi: 10.3390/rs11040435

Tapponnier, P., Zhiqin, X., Roger, F., Meyer, B., Arnaud, N., Wittlinger, G., & Jingsui, Y. (2001). Oblique stepwise rise and growth of the tibet plateau. *Science*, *294*(5547), 1671–1677. doi: 10.1126/science.105978

Tarantola, A. (2005). *Inverse Problem Theory and Methods for Model Parameter Estimation*. Society for Industrial and Applied Mathematics. doi: 10.1137/1.9780898717921

Thollard, F., Clesse, D., Doin, M.-p., Donadieu, J., Durand, P., Grandin, R., ... Specht, B. (2021). FLATSIM : The ForM@Ter LArge-Scale Multi-Temporal Sentinel-1 InterferoMetry Service. *Remote Sensing*, *13*(18), 1–29.

Turcotte, D., & Schubert, G. (2014). *Geodynamics* (3rd ed.). Cambridge University Press. doi: 10.1017/CBO9780511843877

Tymofyeyeva, E., & Fialko, Y. (2018). Geodetic Evidence for a Blind Fault Segment at the Southern End of the San Jacinto Fault Zone. *Journal of Geophysical Research: Solid Earth*, *123*(1), 878–891. doi: 10.1002/2017JB014477

Walters, R. J., Gregory, L. C., Wedmore, L. N., Craig, T. J., McCaffrey, K., Wilkinson, M., ... Vittori, E. (2018). Dual control of fault intersections on stop-start rupture in the 2016 Central Italy seismic sequence. *Earth and Planetary Science Letters*, *500*, 1–14. doi: 10.1016/j.epsl.2018.07.043

Wang, H., Liu-Zeng, J., Ng, A.-M., Ge, L., Javed, F., Long, F., ... Shao, Z. (2017). Sentinel-1 observations of the 2016 Menyuan earthquake: A buried reverse event linked to the left-lateral Haiyuan fault. *International Journal of Applied Earth Observation and Geoinformation*, *61*(October 2016), 14–21. doi: 10.1016/j.jag.2017.04.011

Wang, H., & Wright, T. J. (2012). Satellite geodetic imaging reveals internal deformation of western Tibet. *Geophysical Research Letters*, *39*(7), 1–5. doi: 10.1029/2012GL051222

Wang, H., Wright, T. J., Liu-Zeng, J., & Peng, L. (2019). Strain Rate Distribution in South-Central Tibet From Two Decades of InSAR and GPS. *Geophysical Research Letters*, *46*(10), 5170–5179. doi: 10.1029/2019GL081916

Wang, J., Wang, C., Zhang, H., Tang, Y., Duan, W., & Dong, L. (2021). Freeze-thaw deformation cycles and temporal-spatial distribution of permafrost along the qinghai-tibet railway using multitrack InSAR processing. *Remote Sensing*, *13*(23). doi: 10.3390/rs13234744

Wang, M., & Shen, Z.-K. (2020). Present-Day Crustal Deformation of Continental China Derived From GPS and Its Tectonic Implications. *Journal of Geophysical Research: Solid Earth*, *125*(2). doi: 10.1029/2019JB018774

Wang, W., Qiao, X., Yang, S., & Wang, D. (2017). Present-day velocity field and block kinematics of Tibetan Plateau from GPS measurements. *Geophysical Journal International*, *208*(2), 1088–1102. doi: 10.1093/gji/ggw445

Wang, Y., Wang, M., & Shen, Z. K. (2017). Block-like versus distributed crustal deformation around the northeastern Tibetan plateau. *Journal of Asian Earth Sciences*, *140*, 31–47. doi: 10.1016/j.jseaes.2017.02.040

Weiss, J. R., Walters, R. J., Morishita, Y., Wright, T. J., Lazecky, M., Wang, H., ... Parsons, B. (2020). High-resolution surface velocities and strain for Anatolia from Sentinel-1 InSAR and GNSS data. *Geophysical Research Letters*, 0–2. doi: 10.1029/2020GL087376

Wesnousky, S. G. (2008). Displacement and geometrical characteristics of earthquake surface ruptures: Issues and implications for seismic-hazard analysis and the process of earthquake rupture. *Bulletin of the Seismological Society of America*, *98*(4), 1609–1632. doi: 10.1785/0120070111

Wessel, P., Luis, J. F., Uieda, L., Scharroo, R., Wobbe, F., Smith, W. H., & Tian, D. (2019). The Generic Mapping Tools Version 6. *Geochemistry, Geophysics, Geosystems*, *20*(11), 5556–5564. doi: 10.1029/2019GC008515

Wessel, P., Smith, W. H. F., Scharroo, R., Luis, J., & Wobbe, F. (2013). Generic Mapping Tools: Improved Version Released. *Eos, Transactions American Geophysical Union*, *94*(45), 409-410. doi: 10.1002/2013EO450001

Wicks, C., Weaver, C., Bodin, P., & Sherrod, B. (2013). InSAR Evidence for an active shallow thrust fault beneath the city of Spokane Washington, USA. *Journal of Geophysical Research: Solid Earth*, *118*(3), 1268-1276. doi: 10.1002/jgrb.50118

Wright, T. J., Elliott, J. R., Wang, H., & Ryder, I. (2013). Earthquake cycle deformation and the Moho: Implications for the rheology of continental lithosphere. *Tectonophysics*, *609*, 504–523. doi: 10.1016/j.tecto.2013.07.029

Wu, H., Wang, L., Liu, L., Hao, L., Ma, Q., Li, F., ... Zheng, Y. (2019). Groundwater recharge and evolution in the Wuwei Basin, northwestern China. *Environmental Earth Sciences*, *78*(12), 1–10. doi: 10.1007/s12665-019-8362-5

Xiong, X., Shan, B., Zheng, Y., & Wang, R. (2010). Tectonophysics Stress transfer and its implication for earthquake hazard on the Kunlun Fault , Tibet. *Tectonophysics*, *482*(1-4), 216–225. doi: 10.1016/j.tecto.2009.07.020

Xu, X., Han, Z., Yang, X., Zhang, S., Yu, G., Zhou, B., ... Ran, Y. (2016). *Zhong Guo Ji Lin Jin Di Qu Di Zhen Gou Zao Tu.* doi: 10.12031/activefault.china.250.2016.db

Xu, X., & Sandwell, D. T. (2020). Toward Absolute Phase Change Recovery With InSAR: Correcting for Earth Tides and Phase Unwrapping Ambiguities. *IEEE Transactions on Geoscience and Remote Sensing*, *58*(1), 726–733.

Xu, X., Sandwell, D. T., Klein, E., & Bock, Y. (2021). Integrated Sentinel-1 InSAR and GNSS Time-Series Along the San Andreas Fault System. *Journal of Geophysical Research: Solid Earth*, *126*(11), 1–14. doi: 10.1029/2021JB022579

Xu, X., Zhang, Z., Hu, F., & Chen, X. (2019). Dynamic rupture simulations of the 1920 Ms 8.5 Haiyuan earthquake in China. *Bulletin of the Seismological Society of America*, *109*(5), 2009–2020. doi: 10.1785/0120190061

Yao, W., Liu-Zeng, J., Oskin, M. E., Wang, W., Li, Z., Prush, V., ... Klinger, Y. (2019). Reevaluation of the Late Pleistocene Slip Rate of the Haiyuan Fault Near Songshan, Gansu Province, China. *Journal of Geophysical Research: Solid Earth*, *124*(5), 5217–5240. doi: 10.1029/2018JB016907

Yu, C., Li, Z., Penna, N. T., & Crippa, P. (2018). Generic Atmospheric Correction Model for Interferometric Synthetic Aperture Radar Observations. *Journal of Geophysical Research: Solid Earth*, *123*(10), 9202–9222. doi: 10.1029/2017JB015305

Yuan, D. Y., Ge, W. P., Chen, Z. W., Li, C. Y., Wang, Z. C., Zhang, H. P., ... Roe, G. H. (2013). The growth of northeastern Tibet and its relevance to large-scale continental geodynamics: A review of recent studies. *Tectonics*, *32*(5), 1358–1370. doi: 10.1002/tect.20081

Zhang, J., Bock, Y., Johnson, H., Fang, P., Williams, S., Genrich, J., ... Behr, J. (1997). Southern California Permanent GPS Geodetic Array: Error analysis of daily position estimates and site velocities. *Journal of Geophysical Research*, *102*(B8), 18035–18005. doi: 10.1029/97JB01380

Zhang, J., Ma, Z., Li, Z., & Li, W. (2009). Study on Deformational Characteristics of Northeastern Qinghai-Xizang (Tibetan) Plateau from Late Cenozoic Deformation in the Xining Basin. *Geological Review*, *55*(4), 731–747.

Zhang, P., Molnar, P., Burchfiel, B. C. C., Royden, L., Wang, Y., Deng, Q., ... Jiao Decheng (1988). Bounds on the Holocene slip rate of the Haiyuan fault, North-Central China. *Quaternary Research*, *30*(2), 151–164. doi: 10.1016/0033-5894(88)90020-8

Zhang, X., Wang, N., Xie, Z., Ma, X., & Huete, A. (2018). Water loss due to in-

creasing planted vegetation over the Badain Jaran Desert, China. *Remote Sensing*, *10*(1), 1–21. doi: 10.3390/rs10010134

Zhang, Y., Shan, X., Zhang, G., Zhong, M., Zhao, Y., Wen, S., ... Zhao, D. (2020). The 2016 Mw 5.9 Menyuan earthquake in the Qilian Orogen, China: A potentially delayed depth-segmented rupture following from the 1986 Mw 6.0 Menyuan Earthquake. *Seismological Research Letters*, *91*(2), 758–769. doi: 10.1785/0220190168

Zhao, S., Zeng, R., Zhang, H., Meng, X., Zhang, Z., Meng, X., ... Liu, J. (2022). Impact of Water Level Fluctuations on Landslide Deformation at Longyangxia Reservoir, Qinghai Province, China. *Remote Sensing*, *14*(212), 1–33.

Zheng, G., Wang, H., Wright, T. J., Lou, Y., Zhang, R., Zhang, W., ... Wei, N. (2017). Crustal Deformation in the India-Eurasia Collision Zone From 25 Years of GPS Measurements. *Journal of Geophysical Research: Solid Earth*, *122*(11), 9290–9312. doi: 10.1002/2017JB014465

Zheng, W., Yuan, D., Zhang, P., Yu, J., Lei, Q., Wang, W., ... Liu, X. (2016). Tectonic geometry and kinematic dissipation of the active faults in the northeastern Tibetan Plateau and their implications for understanding northeastern growth of the plateau ( ). *Quaternary Sciences*, *36*(4), 775–788. doi: 10.11928/j.issn.1001-7410.2016.04.01

Zheng, W., Zhang, P., He, W., Yuan, D., Shao, Y., Zheng, D., ... Min, W. (2013). Transformation of displacement between strike-slip and crustal shortening in the northern margin of the Tibetan Plateau: Evidence from decadal GPS measurements and late Quaternary slip rates on faults. *Tectonophysics*, *584*, 267–280. doi: 10.1016/j.tecto.2012.01.006

Zheng, W. J., Zhang, P. Z., Ge, W. P., Molnar, P., Zhang, H. P., Yuan, D. Y., & Liu, J. H. (2013). Late Quaternary slip rate of the South Heli Shan Fault (northern Hexi Corridor, NW China) and its implications for northeastward growth of the Tibetan Plateau. *Tectonics*, *32*(2), 271–293. doi: 10.1002/tect.20022

Zhou, Y., Thomas, M. Y., Parsons, B., & Walker, R. T. (2018). Time-dependent postseismic slip following the 1978 Mw 7.3 Tabas-e-Golshan, Iran earthquake revealed by over 20 years of ESA InSAR observations. *Earth and Planetary Science Letters*, *483*, 64–75. doi: 10.1016/j.epsl.2017.12.005

Zhu, Y., Wang, K., & He, J. (2020). Effects of Earthquake Recurrence on Localization of Interseismic Deformation Around Locked Strike-Slip Faults. *Journal of Geophysical Research: Solid Earth*, *125*(8). doi: 10.1029/2020JB019817

Zou, D., Zhao, L., Sheng, Y., Chen, J., Hu, G., Wu, T., ... Cheng, G. (2017). A new map of permafrost distribution on the Tibetan Plateau. *Cryosphere*, *11*(6), 2527–2542. doi: 10.5194/tc-11-2527-2017

Supporting Information for "Large-scale Interseismic Strain Mapping of the NE Tibetan Plateau from Sentinel-1 Interferometry"

Q. Ou[1], S. Daout[1] *, J.R. Weiss[2,3,] †, L. Shen[2], M. Lazecký[2], T.J. Wright[2],

B.E. Parsons[1]

[1]COMET, Department of Earth Sciences, University of Oxford, South Parks Road, Oxford, United Kingdom

[2]COMET, School of Earth and Environment, University of Leeds, Leeds, , United Kingdom

[3]Institute of Geosciences, University of Potsdam, Karl-Liebknecht-Strasse 24, Potsdam, Germany

Contents of this file

1. Text S1 to S6
2. Figures S1 to S20

Corresponding author: Q. Ou, COMET, Department of Earth Sciences, University of Oxford, South Parks Road, Oxford, United Kingdom. (qi.ou@earth.ox.ac.uk)

*Current address, Université de Lorraine - CNRS, UMR 7358, rue N. D. des Pauvres, 54501 Vandœuvre les Nancy, France

†Current address, NOAA/NWS Pacific Tsunami Warning Center, 1845 Wasp Boulevard, Honolulu, Hawaii, USA

Introduction

Texts S1-S3 describe detailed methods for InSAR time series analysis. Fig S1-S2 show the interferogram networks. Figs S3-S4 show quality analysis of atmospheric correction using the GACOS model. Text S4 describe GNSS data available in the study area. Figs S5 shows LOS velocities before they are placed in the GNSS reference frame and the distribution of 2D and 3D GNSS stations in the area. Figs S6-S9 illustrate the method used to stitch InSAR LOS along track and assess the effectiveness of the method. Figs S7, S10 and S13 illustrate the detailed steps in decomposing LOS into Cartesian velocities. Text S5 and Fig S11 describe a method to scale InSAR LOS uncertainty maps to remove the local reference effect. Text S6 and S12 compare an alternative velocity decomposition method with the $V_E - V_{UN}$ decomposition described in the main text. Figs S14 and S16 show synthetic tests that inform the filtering of InSAR V_E for strain rate calculations. Fig S17 compares InSAR V_E before and after filtering. Figs S18 and S19 illustrate estimated uncertainties of the V_E and V_N gradients. Fig S20 shows the correlation between ESRI's land cover classification (Karra et al., 2021) and the InSAR V_U map.

Text S1. Ramp removal

Inverting for a network of ramp parameters directly from the network of interferograms is computational expensive. Therefore, we first invert for the best-fit ramp parameters for each interferogram and, from these ramp parameters, invert for networks of ramp parameters per epoch separately to ensure network closure. The ramp removal takes place in four steps: (1) Mask each interferogram with the filtered coherence file from the LiCSAR outputs to only include pixels with coherence higher than 0.5; (2) Estimate the best-fitting linear ramp parameters, a_{ij}, b_{ij}, c_{ij}, for each interferogram between epochs i and j with a planar ramp of the form $z_{ij} = a_{ij}x + b_{ij}y + c_{ij}$, where (x, y) are pixel positions in radar coordinates and calculate the pixel residuals; (3) Separately invert for three networks of epoch ramp parameters a_k, b_k, c_k at each epoch k that best fit the interferogram ramp parameters a_{ij}, b_{ij}, c_{ij} while ensuring network closure; (4) Remove the planar ramps, $z'_{ij} = (a_j - a_i)x + (b_j - b_i)y + (c_j - c_i)$, reconstructed using the epoch ramp parameters from each interferogram.

The inversion in step (3) is weighted by both the temporal baseline of the interferogram in decimal years, dt, and the root-mean-square of the pixel residuals from planar ramp fitting in step (2), rms. This gives higher weights to interferograms with shorter temporal baselines and lower rms residuals. The exact formulation is as follows:

$$\begin{bmatrix} \frac{1}{\sigma_{12}} a_{12} \\ \vdots \\ \frac{1}{\sigma_{ij}} a_{ij} \\ \vdots \\ \frac{1}{\sigma_{(k-1)k}} a_{(k-1)k} \end{bmatrix} = \begin{bmatrix} \frac{1}{\sigma_{12}} & (-1 & 1 & 0 & \dots & \dots & 0) \\ \vdots & \vdots & \vdots & \vdots & \vdots & \vdots & \vdots \\ \frac{1}{\sigma_{ij}} & (0 & \dots & -1 & 1 & \dots & 0) \\ \vdots & \vdots & \vdots & \vdots & \vdots & \vdots & \vdots \\ \frac{1}{\sigma_{(k-1)k}} & (0 & \dots & \dots & 0 & -1 & 1) \end{bmatrix} \begin{bmatrix} a_1 \\ a_2 \\ \vdots \\ a_i \\ a_j \\ \vdots \\ a_{k-1} \\ a_k \end{bmatrix} \tag{1}$$

$$\text{where} \quad \sigma_{ij} = \frac{1}{w_1} + \frac{1}{w_2}$$
$$w_1 = exp(\frac{-dt_{ij}}{2})$$
$$w_2 = exp(\frac{-rms_{ij}}{rms_{80}}) + 0.01$$

taking the inversion for parameter a as an example; rms_{80} is a constant equal to the 80 percentile of the rms values of all interferograms, which ensures the partial weights, w_1 and w_2, have similar ranges. The same inversion is performed for ramp parameters b and c separately.

The reconstructed ramps may have slightly different ramp parameters than the best-fitting ramps, but this step is necessary to ensure ramps removed do not introduce artificial phase misclosure in the network. In addition, it also avoids overfitting each interferogram which could be biased by tectonic signals, turbulent tropospheric delays, decorrelation noise and unwrapping mistakes. After ramp removal, the flattened interferograms for all frames have an average pixel root-mean-squared value of 2.16 rad (∼4 cm two-way), which represents the amplitude of spatial variation of the data used in the times series.

Text S2. Time series inversion

Time series analysis was performed using the NSBAS program developed by López-Quiroz, Doin, Tupin, Briole, and Nicolas (2009) and Doin et al. (2015). NSBAS solves for the temporal increments of phase changes, $\delta\phi_n$, per pixel and applies an overall smoothed temporal function defined by ϕ_k^s to regularize the problem in case of gaps in the network

(Doin et al., 2015):

$$\forall q \in [1, M] \quad \sum_{n=i}^{n=j-1} \delta\phi_n = \Phi_q \tag{2}$$

$$-\alpha W_1 \phi_1^s = 0 \tag{3}$$

$$\forall k \in [2, N] \quad \alpha W_k \left(\sum_{n=1}^{n=k-1} \delta\phi_n - \phi_k^s \right) = 0 \tag{4}$$

$$\forall k \in [1, N] \quad \gamma \omega_k \partial^2 \phi_k^s / \partial t^2 = 0 \tag{5}$$

where Φ_q is the phase in qth interferogram between epoch numbers $n = i$ and $n = j$; ϕ_k is the cumulative phase increment from the first epoch $\phi_1 = 0$ to ϕ_{k-1}. N is the total number of epochs; M is the total number of interferograms. γ is the smoothing coefficient; ω_k is the average time interval between the 5 epochs used to calculate the second derivative. α is set small enough to only have an impact when there are missing links in the network. W_k can be changed at each iteration to weight the inversion differently. The method also has an option to downsample the data for faster computation.

The full-resolution inversion is carried out in two iterations. The first iteration is weighted by the planar ramp misfit per interferogram obtained from the previous step such that the spatially noisier pixels are weighted less. The residuals between the input interferograms and reconstructed interferograms from the first iteration are used to weight the second iteration such that interferograms that fit poorly temporally into the network have less effect on the final time series. We then added the incremental phase delays, $\delta\phi_n$, assuming $\phi_1 = 0$, to obtain the time series of total phase delay, ϕ_k, for LOS velocity extraction.

Text S3. LOS Velocity Extraction

We extract a linear velocity, V, from the time series with $\phi_k = Vt_k$ also in two iterations, where t_k is the cumulative time from the first epoch (Daout et al., 2017). The first iteration is weighted by $\phi_{RMS_{epoch}}$ from the time series inversion and the RMS residual to the planar ramp misfit of the cumulative displacement at each epoch. This means dates associated with interferograms that poorly fit the reconstructed interferograms and dates with noiser cumulative displacements have less effect on the linear velocity. Then, the misfit per pixel per epoch from the first iteration is added to the weighting parameter for the second iteration of inversion such that the epochs that deviate more from a linear velocity trend are weighted less.

Text S4. GNSS data on the NE Tibetan Plateau

Thanks to the two-phased installation of the CMONOC GNSS network in 1999 and 2009, the NE Tibetan Plateau is well covered by GNSS stations in terms of spatial density and distribution (Gan et al., 2007; Liang et al., 2013; Wang & Shen, 2020). Most stations in the area were installed in phase I of the project in 1999. Most of the stations in the area are campaign GNSS sites that have existed for almost 20 years. The sites were measured twice a year resulting in horizontal velocities with low uncertainties. Wang and Shen (2020) present the latest horizontal velocity field for the area, combining data from continuous and campaign stations from both CMOMOC and regional networks. Their data are published in both ITRF2008 and a Eurasia-fixed reference frame and have an average uncertainty of 0.2 mm/yr. Vertical velocities are available from Liang et al. (2013) in both ITRF2008 and a stable northern neighbours reference frame, with an average uncertainty of 1.5 mm/yr. The stable northern neighbours reference is relative to the average vertical velocity from three continuous stations in the stable Alashan, Ordos and Mon-

golia blocks to highlight the relative vertical motion within the Tibetan Plateau (Liang et al., 2013). As the horizontal components are orthogonal to the vertical component and the reference frame transformations in the horizontal and vertical components are independent, we combine the horizontal components in the Eurasia-fixed reference frame from Wang and Shen (2020) with the vertical components in stable northern neighbours reference frame from Liang et al. (2013) to highlight the tectonic signals.

Not all stations with horizontal velocities have associated vertical velocities because Liang et al. (2013) discarded vertical measurements with uncertainty greater than 2.5 mm/yr and from stations in operation for less than 3 years. There are 282 stations with horizontal velocities in the area covered by the InSAR LOS data and 169 of these have an associated vertical velocity. All 23 frames contain at least 10 well-distributed stations and 20 have at least 8 stations with 3D velocities (Fig 4). Only three frames in the southwest, 026A_05526_131313, 106D_05447_131313 and 033D_05503_131313 (Fig 1), have only 2 or 3 3D stations available, but all have good 2D station coverage.

Text S5. Adjusting $\sigma(LOS)$ for velocity decomposition

The $\sigma(LOS)$ maps derived from time series analysis have lower uncertainties around the chosen reference windows (Fig 2o). This is partly due to the inherent better data quality as the references are chosen in high-coherence non-deforming areas, and partly due to the referencing effect that locally suppressed scatters in the time series and potentially distributed the scatter in the reference window to pixels further away. If these $\sigma(LOS)$ maps are used in the velocity decomposition, the LOS entry that happen to be near the local reference of the frame will be weighted more heavily and the low uncertainty will be reflected in the $\sigma(V_E)$ and $\sigma(V_{UN})$ maps.

The conventional approach for propagating such spatially correlated errors through subsequent calculations is via a covariance matrix estimated from semivariograms based on the LOS velocities (i.e., Sudhaus & Jónsson, 2009). However, in the velocity decomposition step, this approach would require all pixels in the map to be decomposed together with a covariance matrix of the dimension of $10^8 \times 10^8$, which is computationally impractical to implement. The signals in the velocity maps also do not always allow the semivariograms to plateau, making the estimation of a sill difficult. Therefore, we performed velocity decomposition pixel by pixel and tried to remove the effect of the local reference on each $\sigma(LOS)$ map.

We first fitted a spherical model (Equation 7) to the bin median values along the uncertainty profile (thick yellow line in Fig S11a), where d is now distance away from the reference point (yellow dot in Fig S11b). As the reference was the mean value of pixels within a 400×400 window of each contributing interferogram, rather than a fixed pixel on the map, we chose the zero distance at the median location of all pixels with $\sigma(LOS)$ in the lowest 2 percentile. To ensure a good profile fit near the nugget, we weighted the spherical model fitting by $1/(std+d/d_{max})$, where std is the standard deviation of $\sigma(LOS)$ in each bin (thin yellow line in Fig S11a) and d_{max} is the longest distance obtained in the frame.

Then, we scaled up the profile to the sill level by multiplying each scatter point by the ratio between the sill and the best-fit spherical model evaluated at the same distance (red line in Fig S11a). Thanks to the non-zero nugget resulting from the window referencing of the inteferograms, no extreme uncertainty values formed around the reference after scaling. The scatter and the $\sigma(LOS)$ values become more uniform across the scaled

uncertainty profile (Fig S11c). The region around the reference window in the scaled $\sigma(LOS)$ map (Fig S11d) no longer show an uncertainty dip. However, the uncertainty variation characteristic of the quality of time series at each pixel is retained. After the scaled $\sigma(LOS)$ are propagated through the velocity decomposition, the $\sigma(V_E)$ and $\sigma(V_U)$ maps obtained no longer show local referencing effects, but instead, represent uncertainties with velocities referenced in the far field (Fig S14b and Fig S16d).

Text S6. One-Stage Velocity Decomposition with Interpolated GNSS V_N

We compare the two-stage velocity decomposition described in the main text, where V_E and V_{UN} are obtained first from LOS velocity maps before V_U is obtained from V_{UN}, with the conventional approach where the interpolated V_N from GNSS is first taken out of the LOS before V_E and V_U are decomposed in a one stage.

$$\begin{bmatrix} \frac{1}{\sigma(a_0)}(LOS_{a_0} - V_N(sin(\phi_{a_0})sin(\theta_{a_0})) \\ \frac{1}{\sigma(a_1)}(LOS_{a_1} - V_N(sin(\phi_{a_0})sin(\theta_{a_0})) \\ \frac{1}{\sigma(d_0)}(LOS_{d_0} - V_N(sin(\phi_{d_0})sin(\theta_{d_0})) \\ \frac{1}{\sigma(d_1)}(LOS_{d_1} - V_N(sin(\phi_{d_1})sin(\theta_{d_1})) \end{bmatrix} = \begin{bmatrix} \frac{1}{\sigma(a_0)}(-cos(\phi_{a_0})sin(\theta_{a_0}) \;\; cos(\theta_{a_0})) \\ \frac{1}{\sigma(a_1)}(-cos(\phi_{a_1})sin(\theta_{a_1}) \;\; cos(\theta_{a_1})) \\ \frac{1}{\sigma(d_0)}(-cos(\phi_{d_0})sin(\theta_{d_0}) \;\; cos(\theta_{d_0})) \\ \frac{1}{\sigma(d_1)}(-cos(\phi_{d_1})sin(\theta_{d_1}) \;\; cos(\theta_{d_1})) \end{bmatrix} \begin{bmatrix} V_E \\ V_U \end{bmatrix} \tag{6}$$

where $\sigma(k) = \sqrt{\sigma(LOS_k)^2 - (\sigma(V_N)sin(\phi_k)sin(\theta_k))^2}$ for k in a_0, a_1, d_0 and d_1. The $\sigma(V_E)$ is similarly obtained by taking the square-root of the diagonal terms of the covariance matrix assuming independent measurements in the data vector.

The differences between the V_E and $\sigma(V_E)$ obtained by these two methods are shown in Fig S12. The V_E difference map shows a systematic variation of the differences along the range direction, with zero difference along the north-south axis where the incidence angles θ between the ascending and descending tracks are equal. The $\sigma(V_E)$ difference map shows a spatial pattern that reflects the distribution of the GNSS stations where the uncertainty

of the V_E map obtained by the one-stage decomposition increases away from the GNSS stations. Overall, the differences between the two V_E maps average to 0.01±0.03 mm/yr, way below the ∼1 mm/yr uncertainty level that we are working with. The differences between the two $\sigma(V_E)$ maps average to 0.004±0.007 mm/yr, again negligible, suggesting both methods can be used without affecting the final results.

References

Chen, P., Shi, W., Liu, Y., & Cao, X. (2022). Slip rate deficit partitioned by fault-fold system on the active Haiyuan fault zone, Northeastern Tibetan Plateau. *Journal of Structural Geology*, *155*(January), 104516. doi: 10.1016/j.jsg.2022.104516

Daout, S., Doin, M.-P., Peltzer, G., Socquet, A., & Lasserre, C. (2017). Large-scale InSAR monitoring of permafrost freeze-thaw cycles on the Tibetan Plateau. *Geophysical Research Letters*, *44*(2), 901-909. doi: 10.1002/2016GL070781

Diao, F., Xiong, X., Wang, R., Walter, T. R., Wang, Y., & Wang, K. (2019). Slip Rate Variation Along the Kunlun Fault (Tibet): Results From New GPS Observations and a Viscoelastic Earthquake-Cycle Deformation Model. *Geophysical Research Letters*, *46*(5), 2524–2533. doi: 10.1029/2019GL081940

Doin, M. P., Twardzik, C., Ducret, G., Lasserre, C., Guillaso, S., & Jianbao, S. (2015). InSAR measurement of the deformation around Siling Co Lake: Inferences on the lower crust viscosity in central Tibet. *Journal of Geophysical Research: Solid Earth*, *120*(7), 5290–5310. doi: 10.1002/2014JB011768

Gan, W., Zhang, P., Shen, Z. K., Niu, Z., Wang, M., Wan, Y., ... Cheng, J. (2007). Present-day crustal motion within the Tibetan Plateau inferred from GPS measurements. *Journal of Geophysical Research: Solid Earth*, *112*(8), 1–14. doi:

10.1029/2005JB004120

Karra, K., Kontgis, C., Statman-Weil, Z., Mazzariello, J., Mathis, M., & Brumby, S. (2021). Global land use/land cover with Sentinel-2 and deep learning. In *Igarss 2021-2021 ieee international geoscience and remote sensing symposium. ieee.*

Liang, S., Gan, W., Shen, C., Xiao, G., Liu, J., Chen, W., ... Zhou, D. (2013). Three-dimensional velocity field of present-day crustal motion of the Tibetan Plateau derived from GPS measurements. *J. Geophys. Res. Solid Earth*, *118*, 5722–5732. doi: 10.1002/2013JB010503

López-Quiroz, P., Doin, M. P., Tupin, F., Briole, P., & Nicolas, J. M. (2009). Time series analysis of Mexico City subsidence constrained by radar interferometry. *Journal of Applied Geophysics*, *69*(1), 1–15. doi: 10.1016/j.jappgeo.2009.02.006

Sudhaus, H., & Jónsson, S. (2009). Improved source modelling through combined use of InSAR and GPS under consideration of correlated data errors: Application to the June 2000 Kleifarvatn earthquake, Iceland. *Geophysical Journal International*, *176*(2), 389–404. doi: 10.1111/j.1365-246X.2008.03989.x

Wang, M., & Shen, Z.-K. (2020). Present-Day Crustal Deformation of Continental China Derived From GPS and Its Tectonic Implications. *Journal of Geophysical Research: Solid Earth*, *125*(2). doi: 10.1029/2019JB018774

Wright, T. J., Elliott, J. R., Wang, H., & Ryder, I. (2013). Earthquake cycle deformation and the Moho: Implications for the rheology of continental lithosphere. *Tectonophysics*, *609*, 504–523. doi: 10.1016/j.tecto.2013.07.029

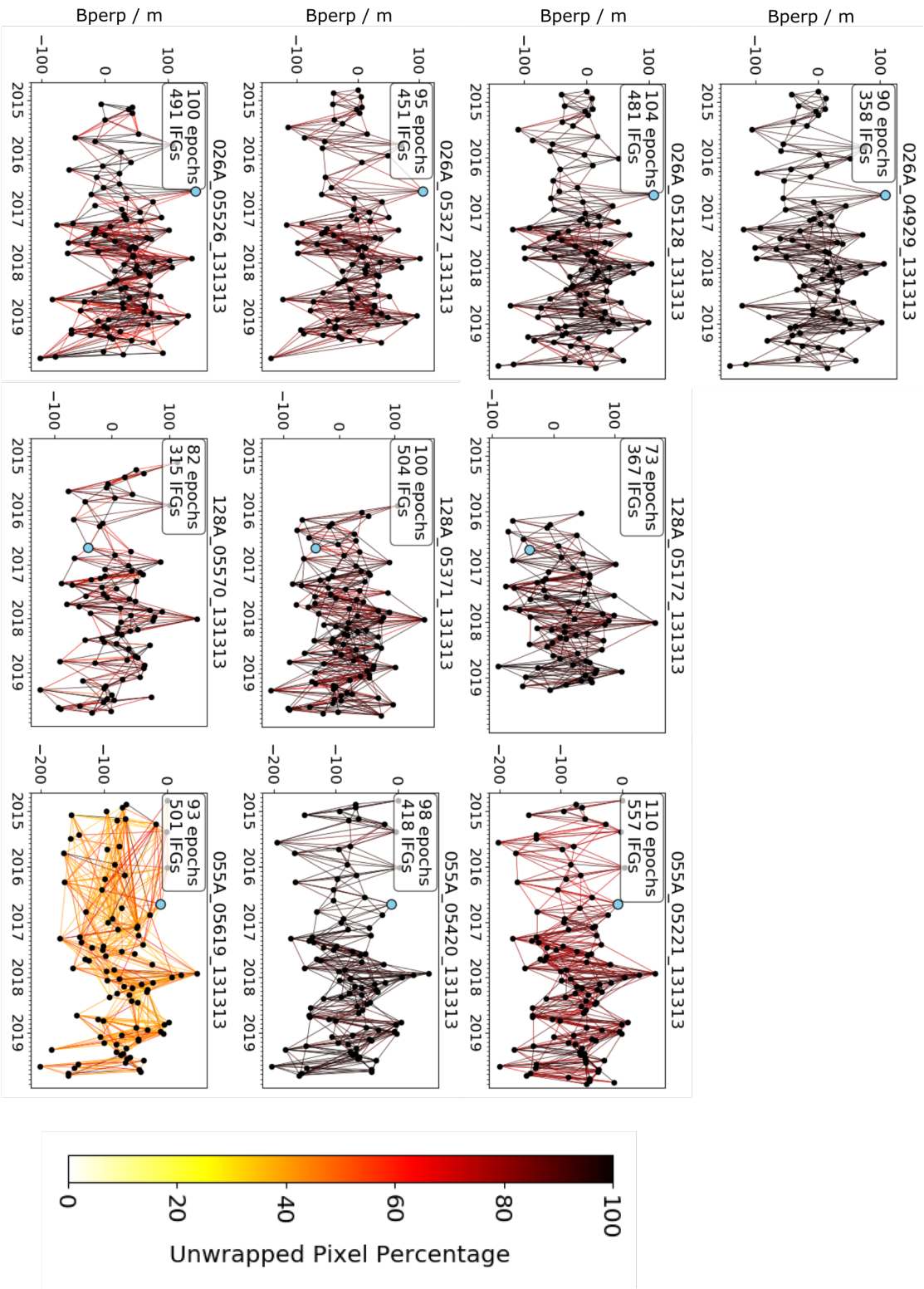

Figure S1. Perpendicular baseline plots for the final time series of ascending frames. Black dots represent all the acquisition dates with their perpendicular baseline. Blue dot in each frame represents the primary epoch to which imagery from other epochs are coregistered. Each line segment represents an interferogram (interferogram) between two acquisition dates with a colour scale representing the percentage of pixels unwrapped out of all pixels in the frame.

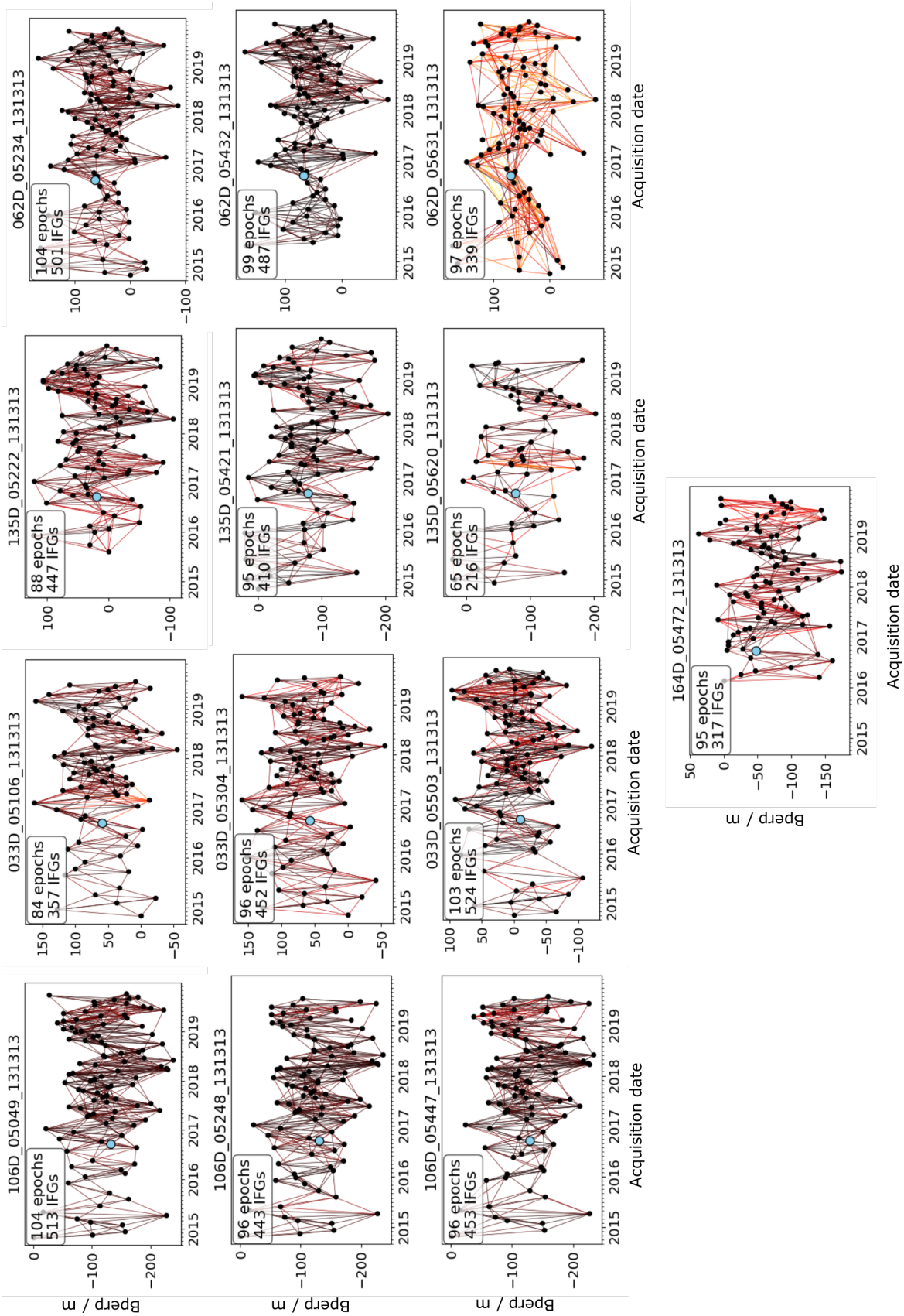

Figure S2. Same as in Fig S1 but for the descending frames.

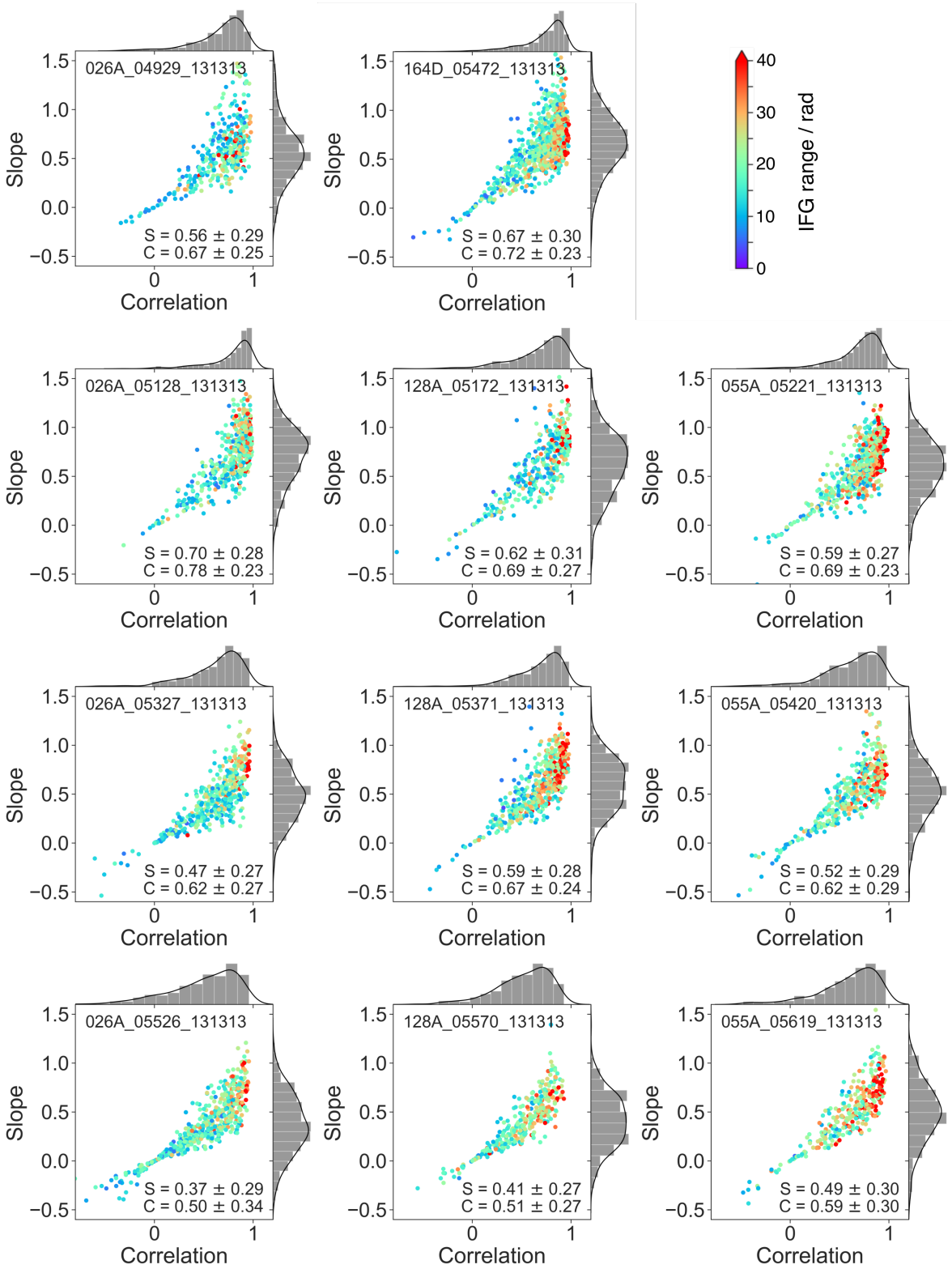

Figure S3. Joint plots between slope and correlation from the scatter plots between GACOS LOS and unwrapped interferogram (Fig 2c) for all interferograms in all ascending frames and frame 164D_05472_131313. The colour of the scatter points represent the amplitude range (difference between the 99.7 percentile and 0.03 percentile of the pixel values) of the corresponding interferogram. The S and C labels in each panel stand for slope and correlation with their mean and standard deviations for each frame.

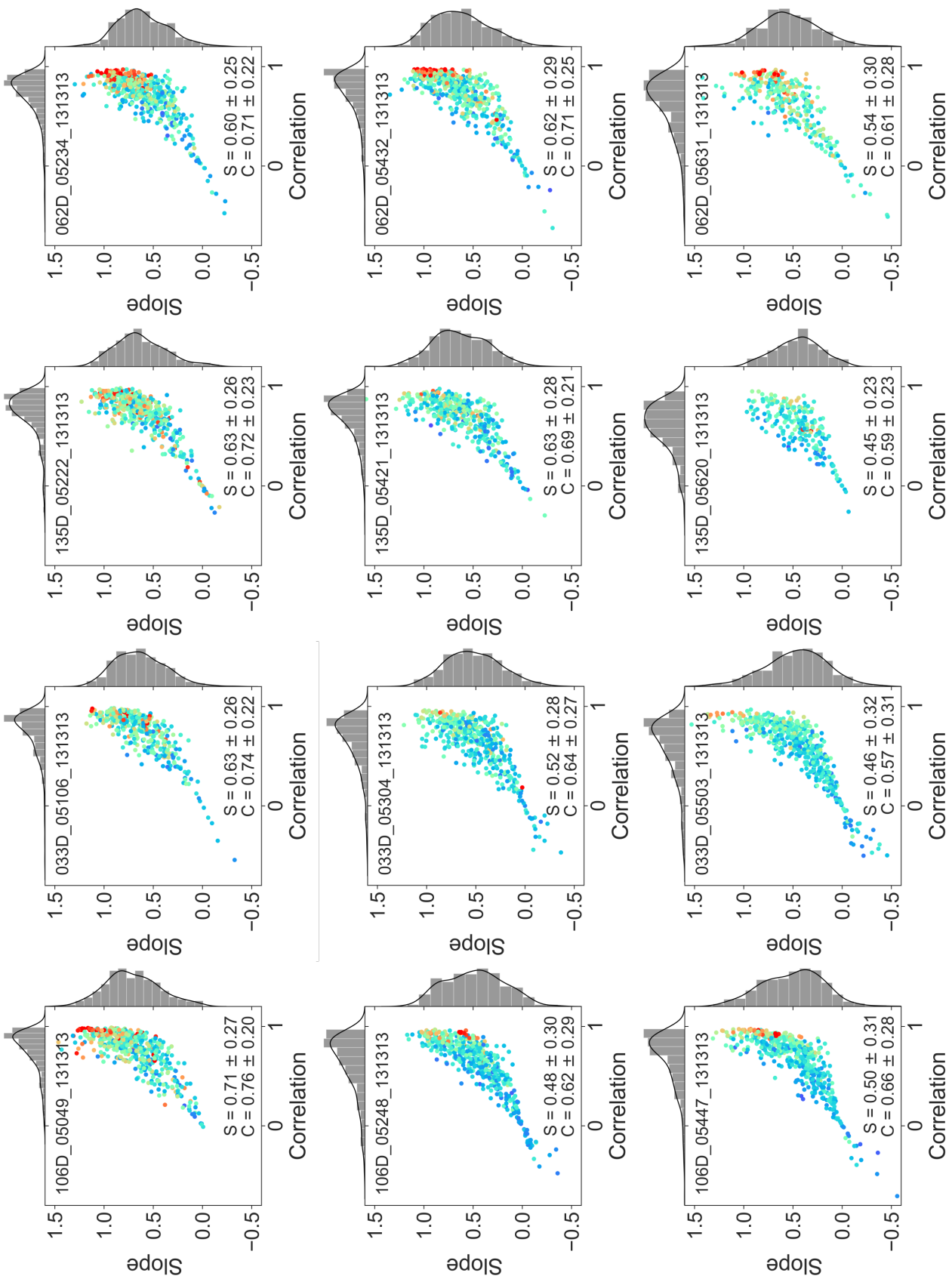

Figure S4. Same as in Fig S3 but for the rest of the descending frames.

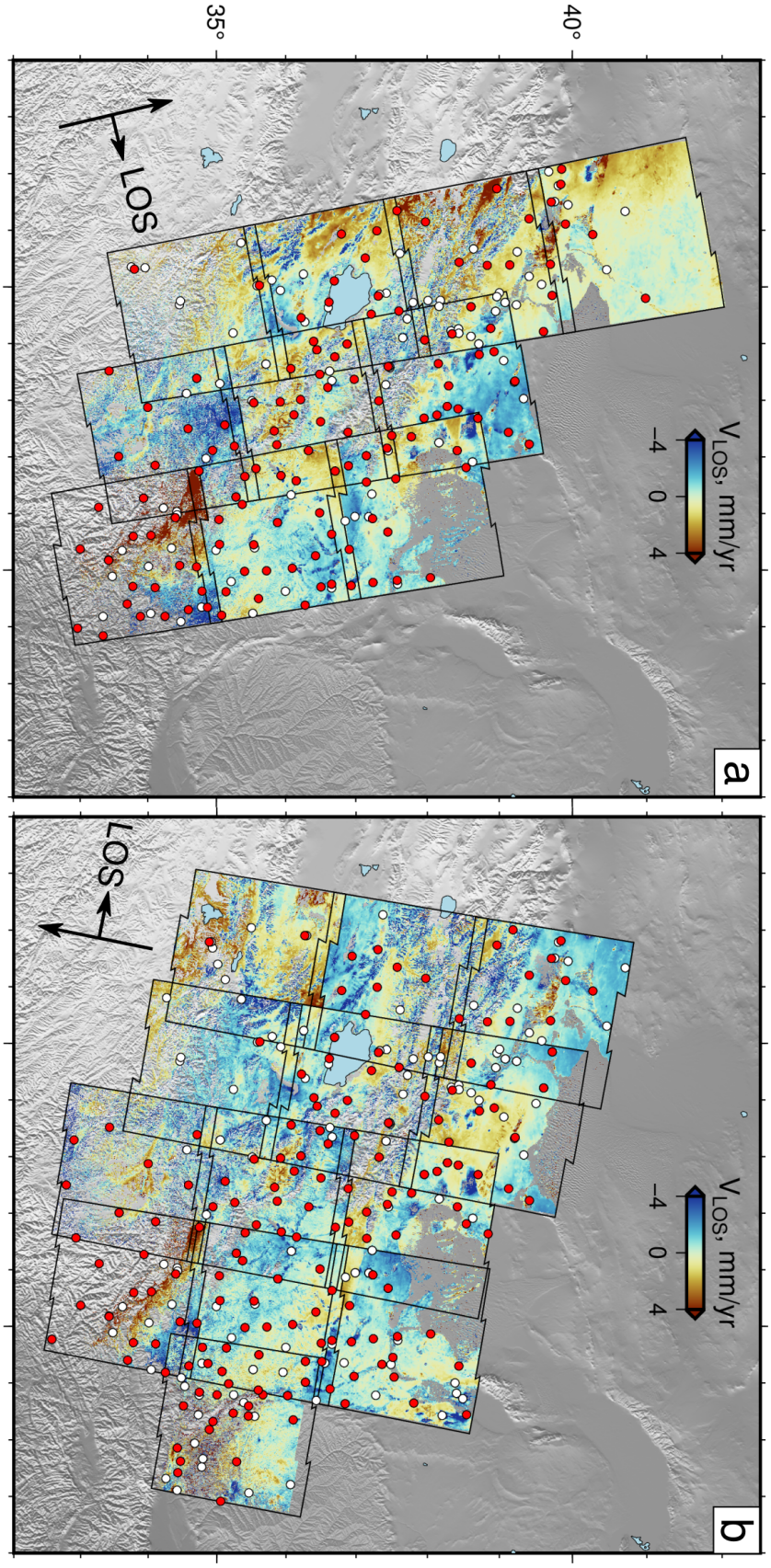

Figure S5. Internally referenced (a) ascending and (b) descending geocoded and cleaned LOS velocity maps merged by placing southern frames on top of northern frames and then eastern tracks on top of western tracks. Red dots are GNSS stations with both horizontal and vertical (3D) velocities and white dots are GNSS stations with horizontal (2D) velocities only. All horizontal GNSS velocities are taken from Wang and Shen (2020) and all vertical GNSS velocities are taken from Liang et al. (2013).

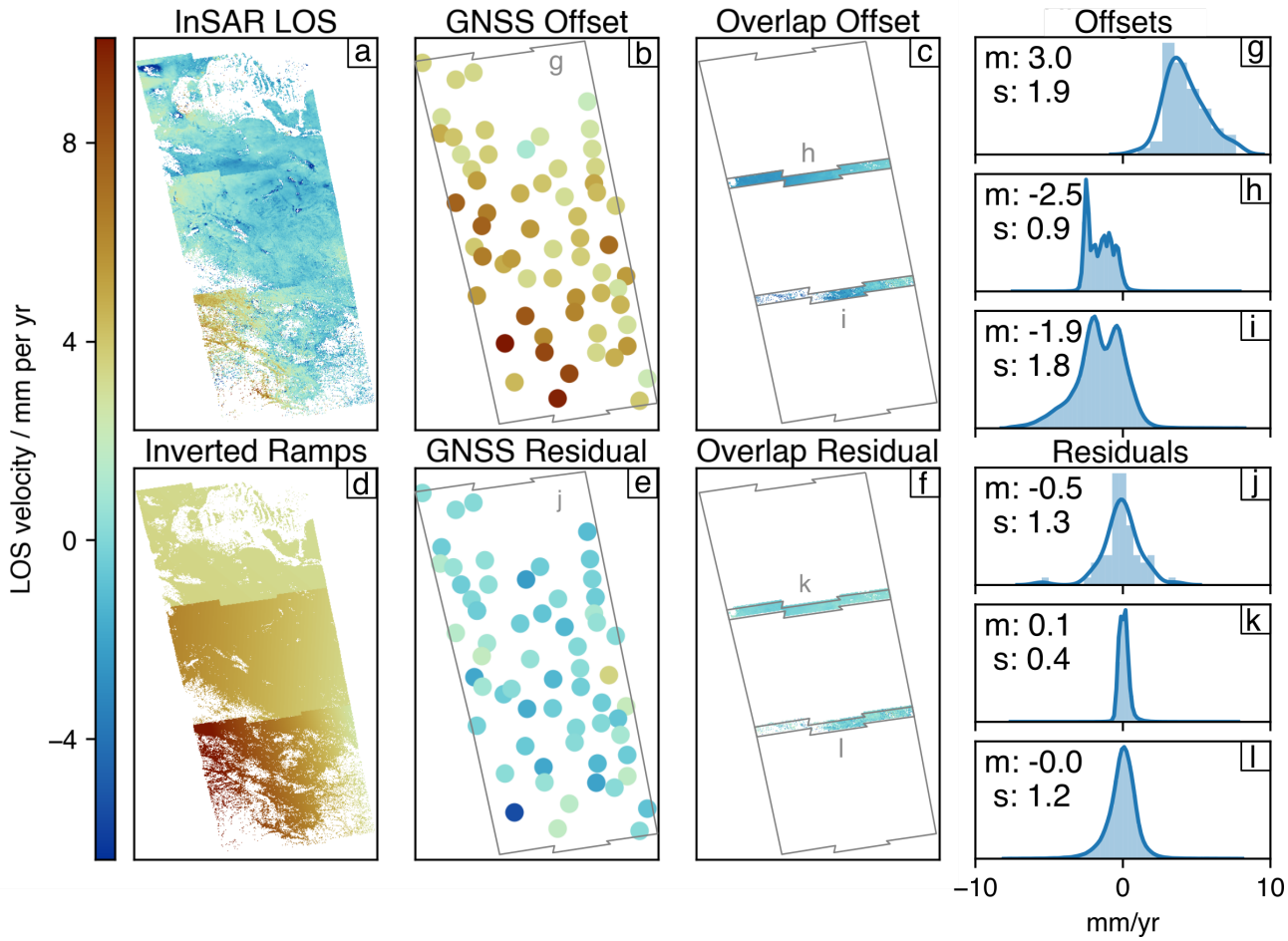

Figure S6. An example from track 055A to illustrate the results of the joint inversion method. (a) Individually referenced LOS velocity frames, same as the eastern track in Fig S5a. (b) Differences between GNSS LOS and the corresponding InSAR LOS in (a). (c) Differences in InSAR frame overlaps obtained by subtracting the southern frame from the northern frame. (d) Ramps inverted from the offsets in (b) and (c) to be subtracted from (a). (e,f) Model residuals after the InSAR LOS are adjusted by the inverted ramps in (d). (g-l) Histograms of the data labelled in panels b, c, e and f, with m = mode and s = standard deviation.

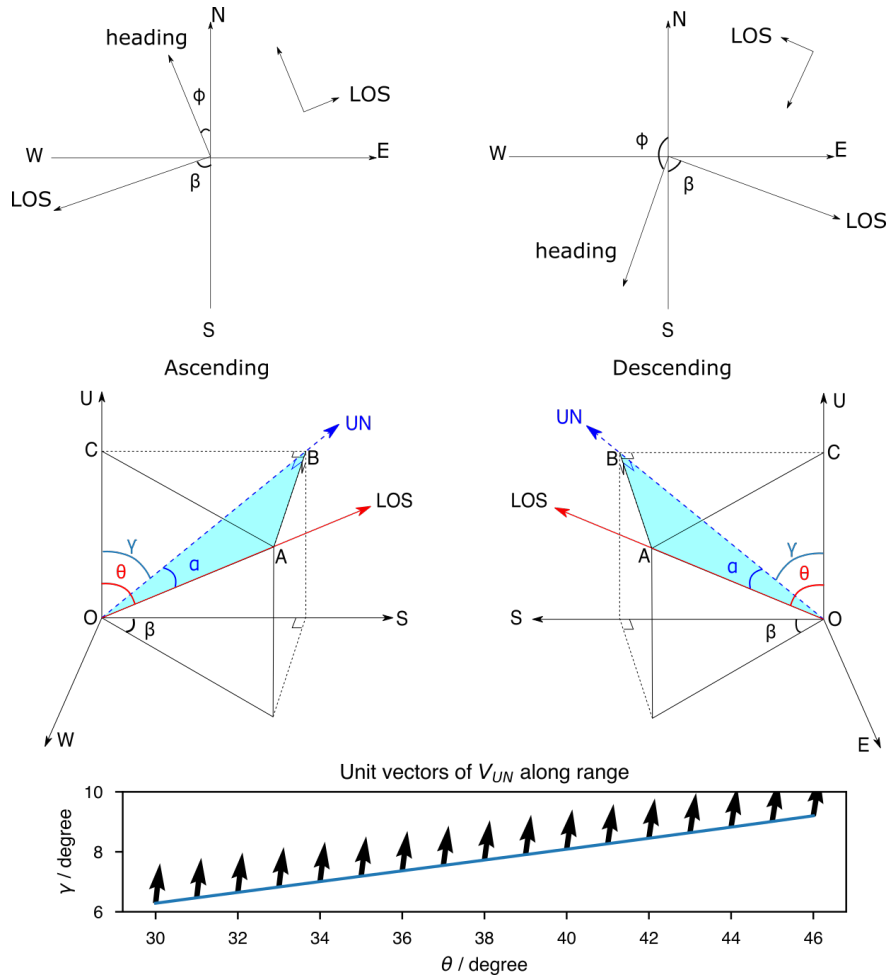

Ascending:
$\phi \sim -10$
$\beta = 180 - 90 + \phi = \phi + 90$
$\sin(\beta) = \sin(\phi+90) = \cos(\phi)$
$V_{LOS} = -V_E \cos(-\phi) \sin(\theta) + (-V_N)\sin(-\phi)\sin(\theta) + V_U \cos(\theta)$
$\quad = -V_E \cos(\phi) \sin(\theta) + V_N \sin(\phi)\sin(\theta) + V_U \cos(\theta)$

Descending:
$\phi \sim -170$
$\beta = 90 - (\phi + 180) = - (\phi + 90)$
$\sin(\beta) = -\sin(\phi+90) = -\cos(\phi)$
$V_{LOS} = V_E \cos(180+\phi) \sin(\theta) + (-V_N)\sin(180+\phi)\sin(\theta) + V_U \cos(\theta)$
$\quad = -V_E \cos(\phi) \sin(\theta) + V_N \sin(\phi)\sin(\theta) + V_U \cos(\theta)$

Geometry:
$AB = OA \sin(\alpha) = OA \sin(\theta) \sin(\beta)$
so, $\sin(\alpha) = \sin(\theta) \sin(\beta)$
$\cos(\alpha) = \mathrm{sqrt}(1 - \sin^2(\alpha))$
$\quad = \mathrm{sqrt}(1 - \sin^2(\theta) \sin^2(\beta))$
$\quad = \mathrm{sqrt}(1 - \sin^2(\theta) \cos^2(\phi))$

Decomposition:
$V_{LOS} = -V_E \cos(\phi) \sin(\theta) + V_N \sin(\phi) \sin(\theta) + V_U \cos(\theta)$
$\quad = -V_E \cos(\phi) \sin(\theta) + V_{UN} \cos(\alpha)$
$\quad = -V_E \cos(\phi) \sin(\theta) + V_{UN}\, \mathrm{sqrt}(1-\sin^2(\theta)\cos^2(\phi))$

so, $V_{UN} = (V_N \sin(\phi) \sin(\theta) + V_U \cos(\theta)) / \mathrm{sqrt}(1- \sin^2(\theta) \cos^2(\phi))$

Small variation in γ:
As $V_{UN} = -V_N \sin(\gamma) + V_U \cos(\gamma)$, we can evaluate γ through:
$\tan(\gamma) = \sin(\gamma) / \cos(\gamma) = -\sin(\phi) \sin(\theta) / \cos(\theta) = -\sin(\phi) \tan(\theta)$
so, $\gamma = \tan^{-1}(-\sin(\phi) \tan(\theta))$ as plotted

Figure S7. Geometry for calculating velocity components from LOS velocities. O=Ground pixel, N=North, E=East, S=South, W=West, U=Up, LOS=Line of sight direction from the point of observation to the satellite, UN=Projection of LOS to the north-up plane. OA=Combined LOS contributions from V_U and V_N. OB=Projection of OA onto the UN plane. ϕ=Negative (heading) angle anti-clockwise from N, θ=Positive (incidence) angle between LOS and U, α=Positive angle between LOS and UN, β=Positive angle between the projection of the LOS onto the horizontal plane and S, γ=Positive angle between UN and U. Arrows in the bottom panel show unit vectors of V_{UN} along range to visually show that variation in γ is negligible along range.

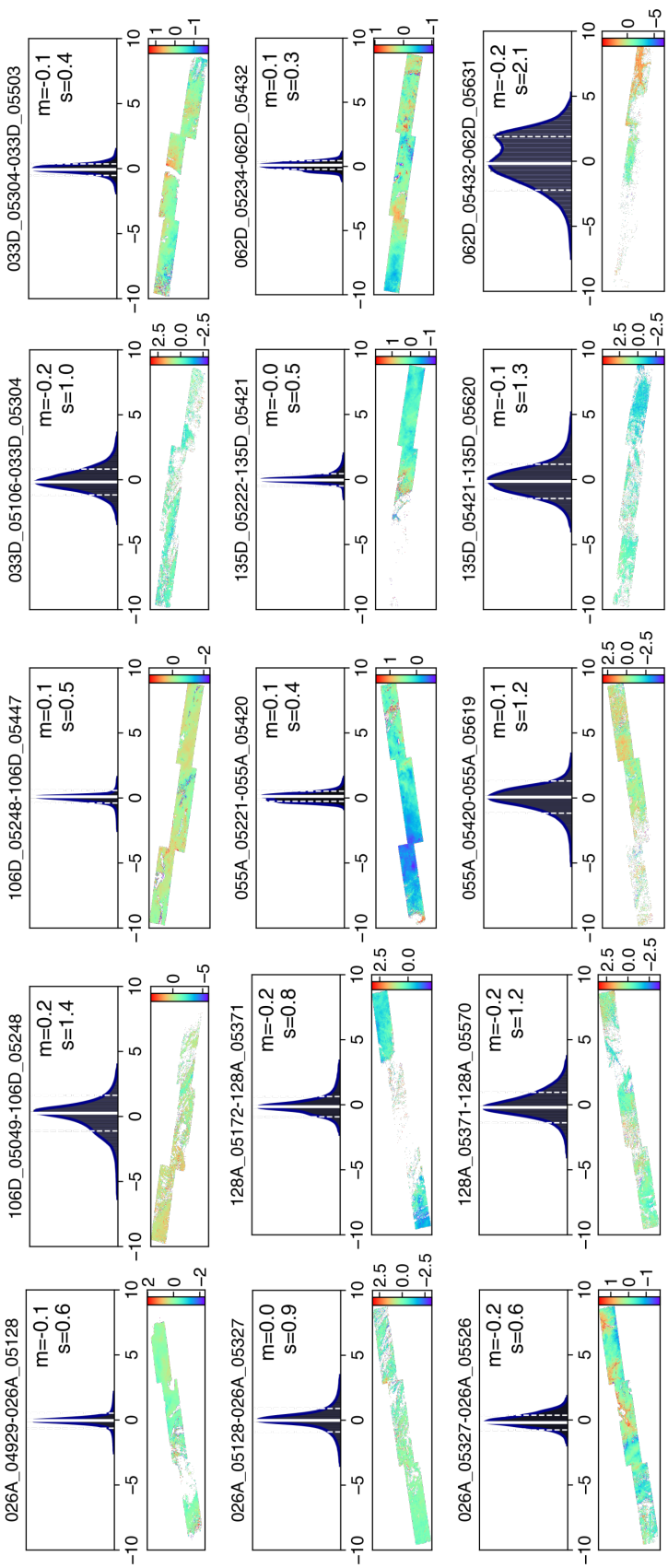

Figure S8. Histograms of pixel differences between frame overlaps along tracks after joint adjustment. m=mode, s=standard deviation.

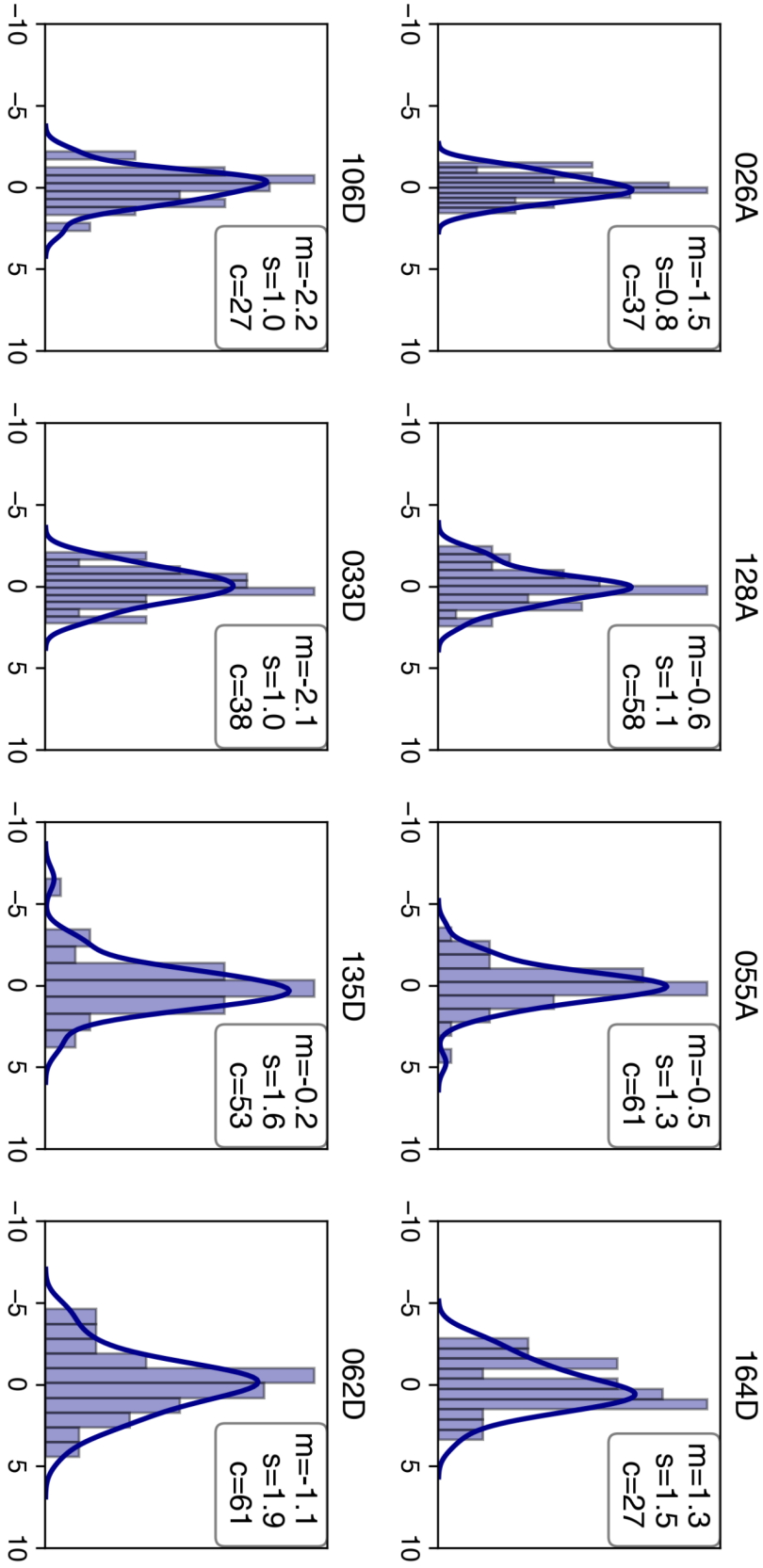

Figure S9. Histograms of residuals between GPS LOS and InSAR LOS in each track after joint adjustment. m=mode, s=standard deviation, c=count of 3D GNSS points in each track.

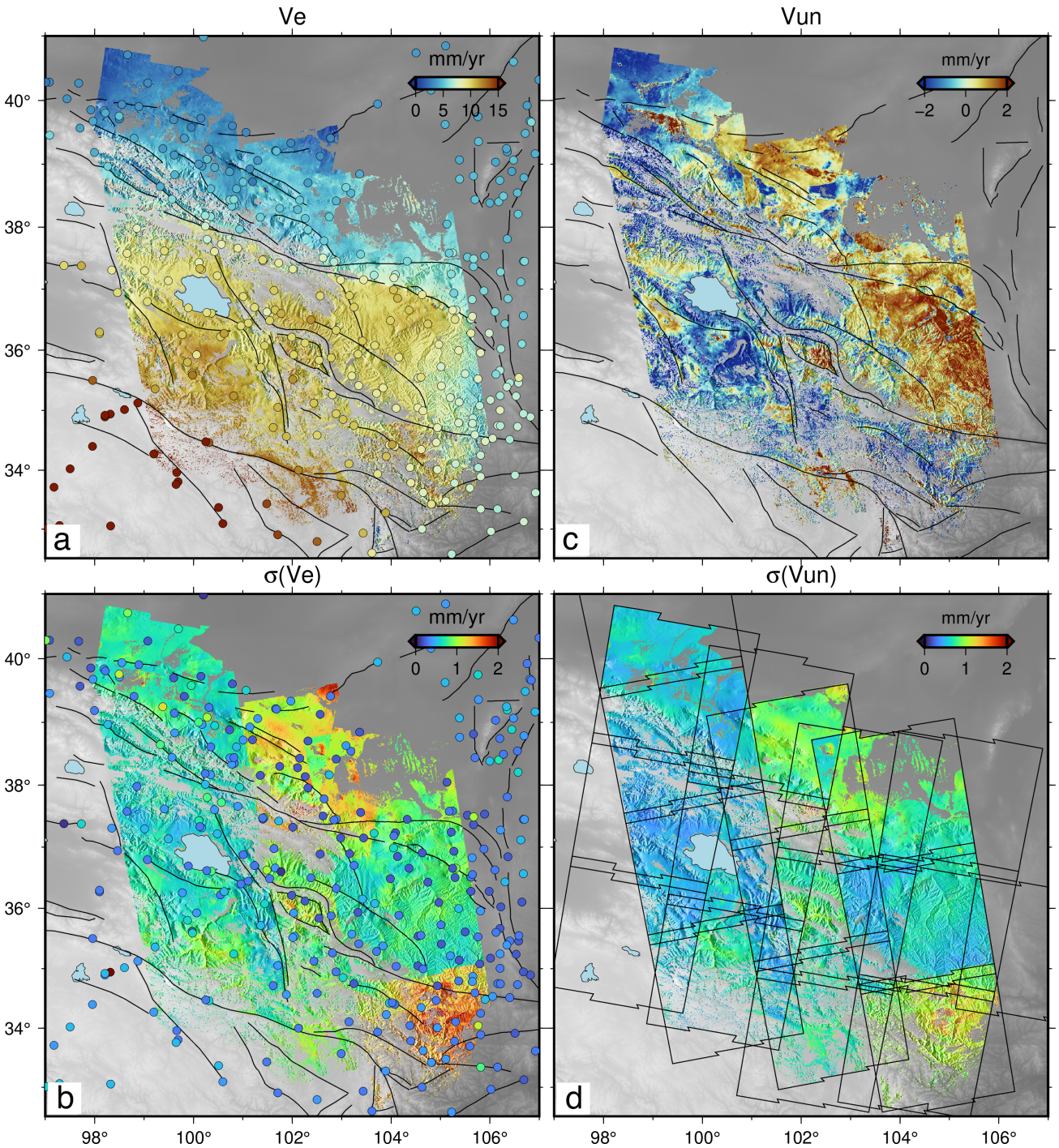

Figure S10. Maps of decomposed V_E and V_{UN} velocity and their associated uncertainty maps $\sigma(V_E)$ and $\sigma(V_{UN})$. Dots in (a-b) are the east component of GNSS velocities and their uncertainties from Wang and Shen (2020) plotted in the same colour map.

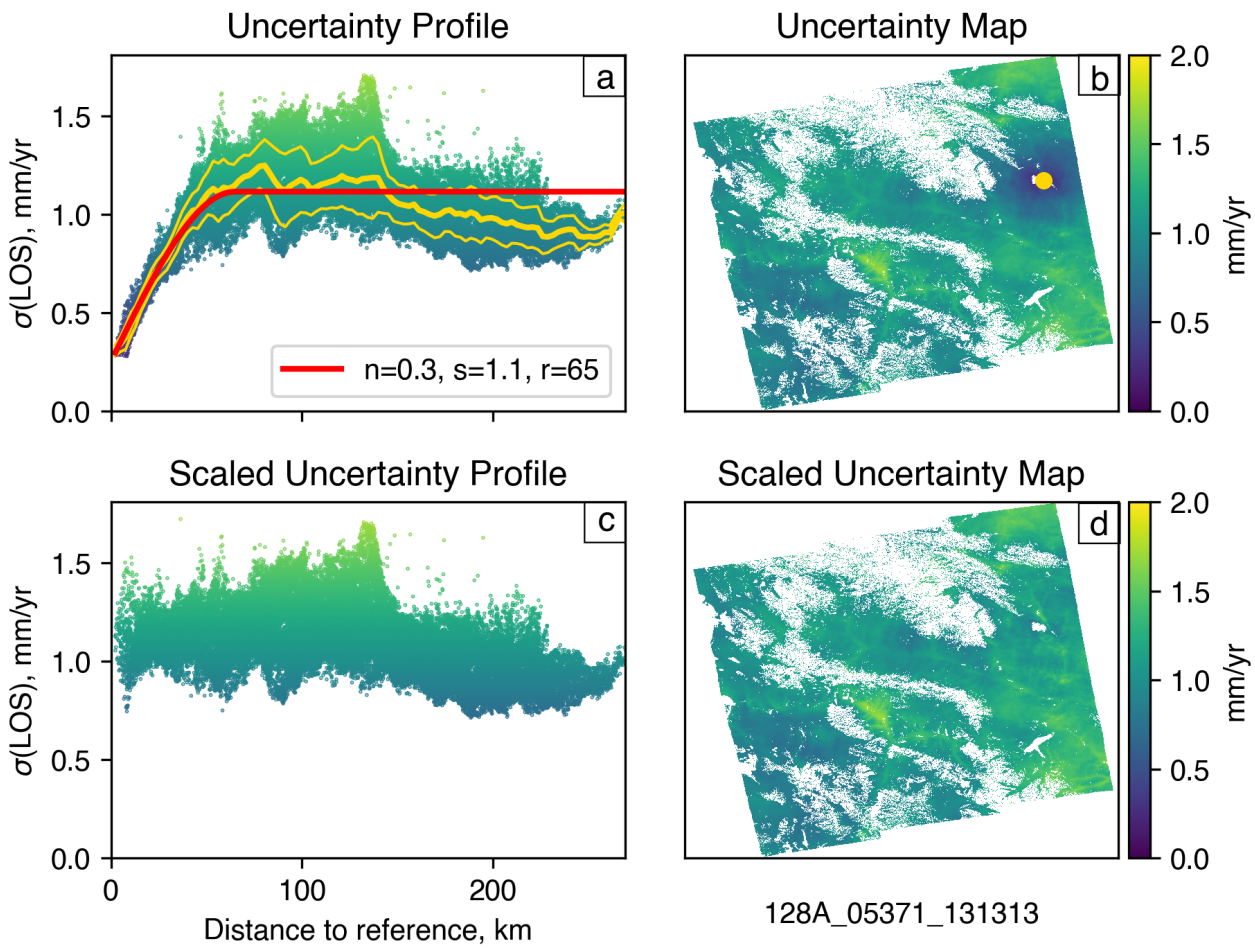

Figure S11. (a) $\sigma(LOS)$ profile against distance away from the reference point indicated by the yellow dot in the $\sigma(LOS)$ map in (b), determined as the median pixel location of pixels with the lowest 2 percent $\sigma(LOS)$ values. In (a), thick and thin yellow lines represent the median and standard deviation evaluated at 100 bin centers, which are used to fit the spherical model in red, with best-fit parameters nugget (n), sill (s) and range (r) labeled. (c) Adjust $\sigma(LOS)$ profile with each scatter point scaled by the ratio between the sill and the best-fit spherical model at given distance. (d) $\sigma(LOS)$ after scaling, with the dip in $\sigma(LOS)$ values removed.

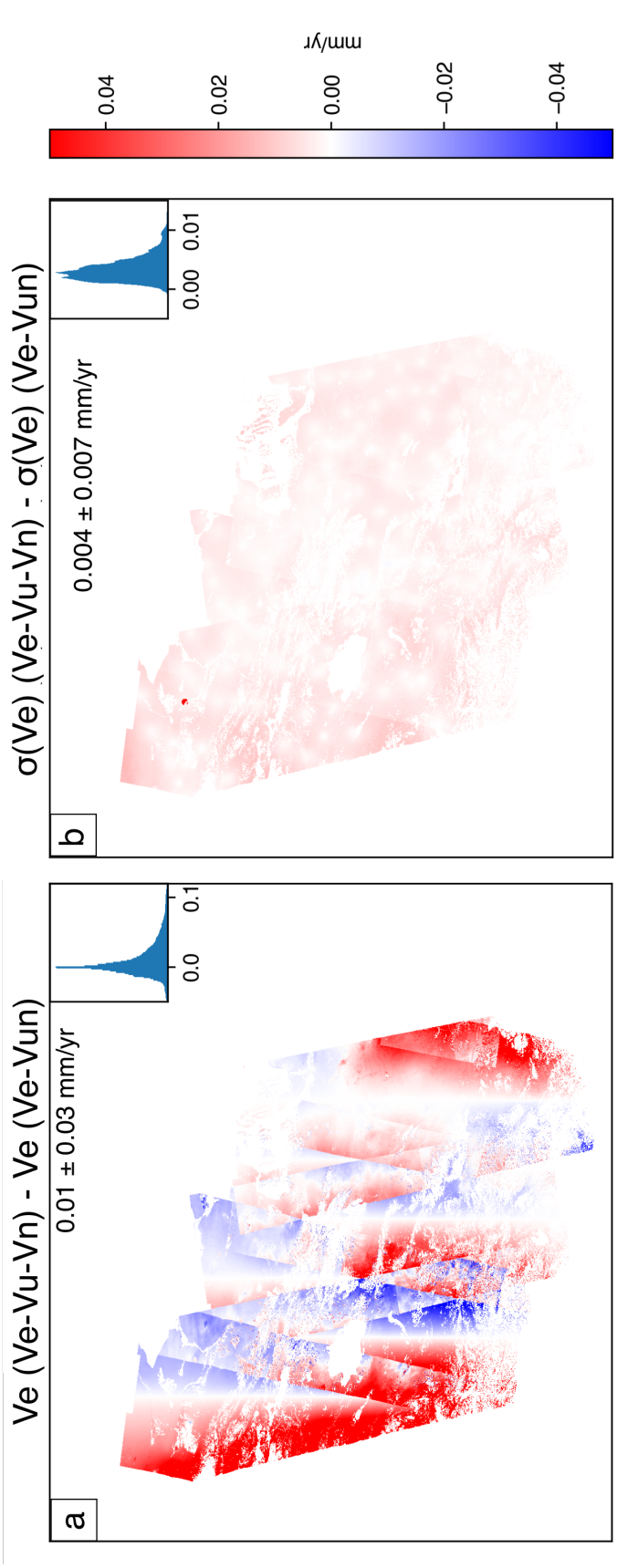

Figure S12. Difference maps and statistical analysis of the differences between the V_E and σV_E maps obtained from method described in Text S6 where the contribution from an interpolated GNSS V_N is first taken out of the LOS velocities to obtain V_E and V_{UN} together and those from the V_E V_{UN} decomposition as described in the main text. Mean and standard deviation of the differences are labeled in each panel.

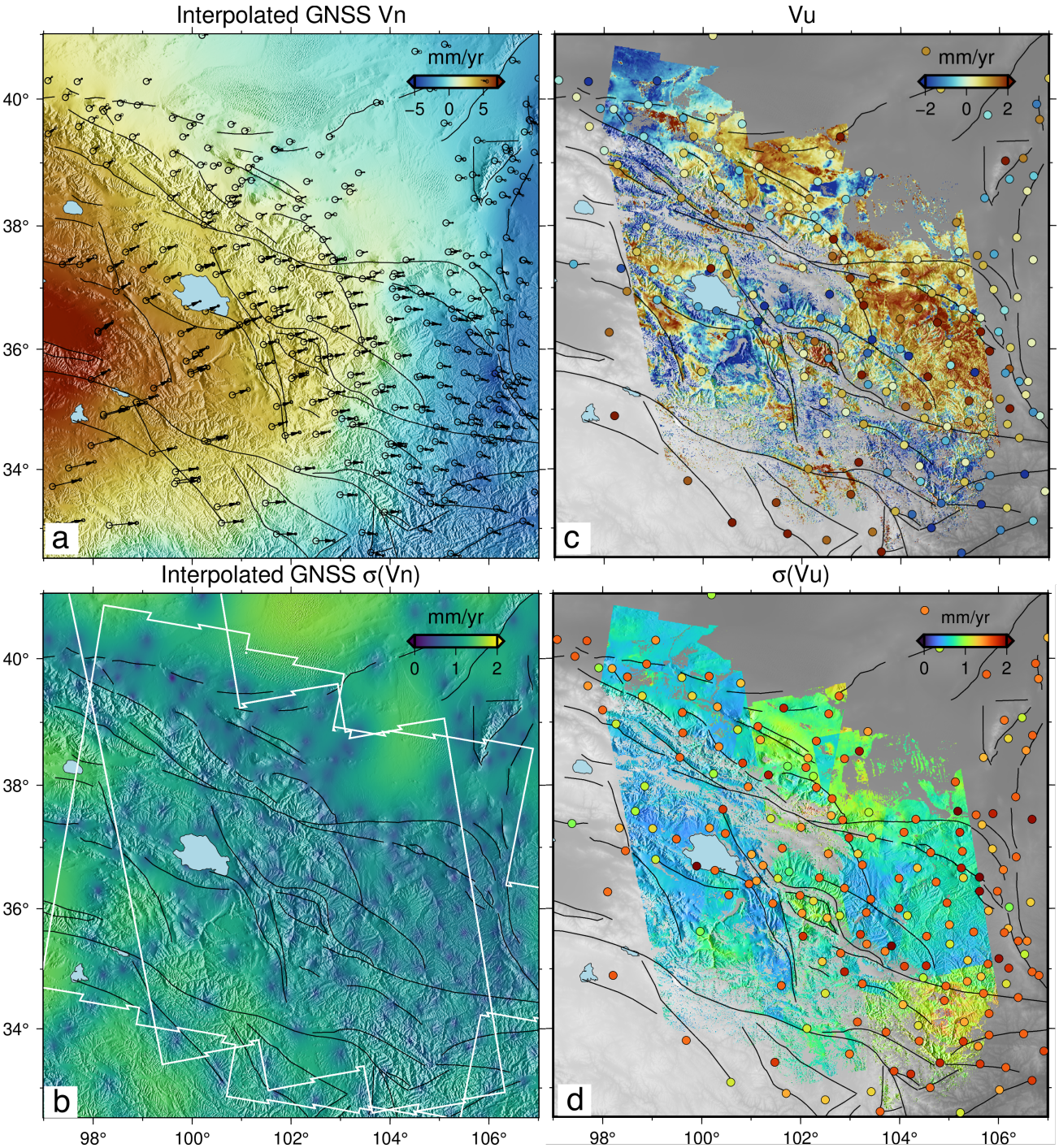

Figure S13. (a-b) Maps of V_N and $\sigma(V_N)$ as interpolated from the north component of the GNSS velocities from Wang and Shen (2020) shown in arrows. (c-d) Resolved maps of V_U and $\sigma(V_U)$, in comparison with the vertical component and uncertainties of the GNSS velocities from (Wang & Shen, 2020) shown as dots in the same colour map.

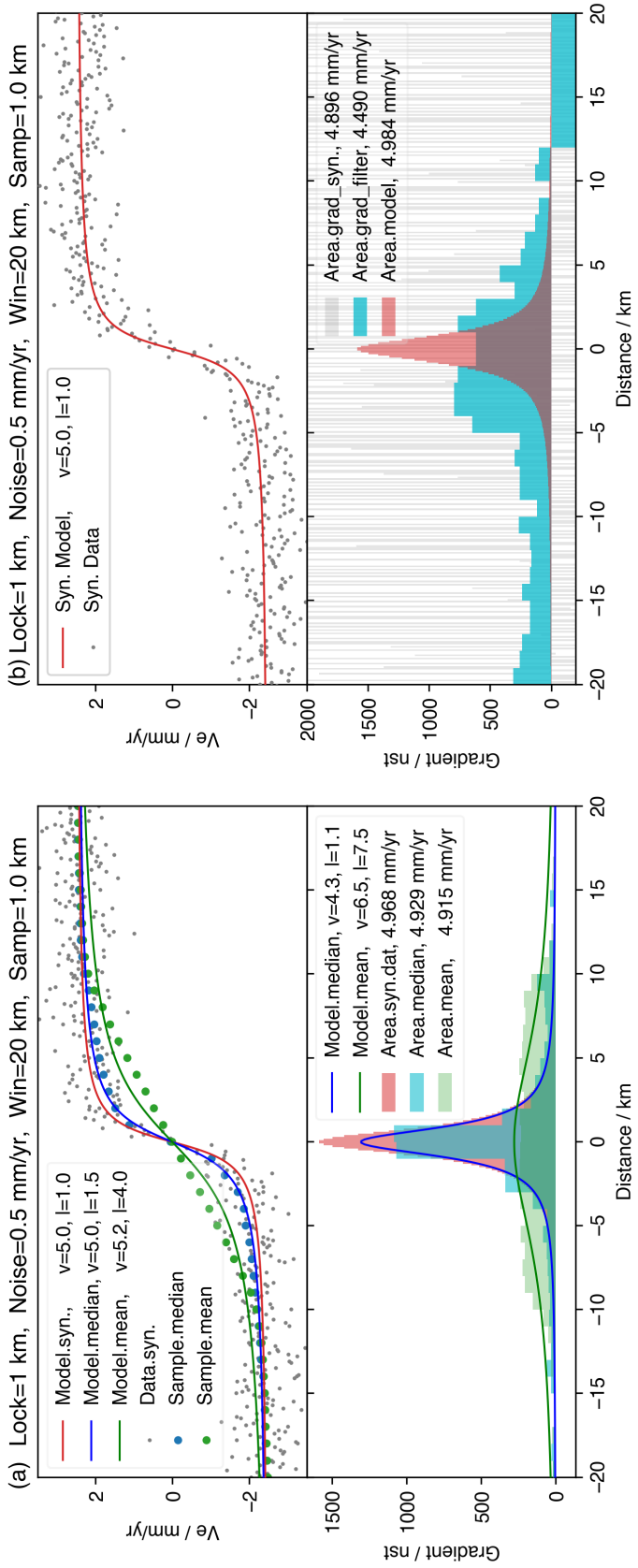

Figure S14. Synthetic test on a 40-km long shallow-locking profile, comparing the effects of (a) median versus mean filtering and of (b) median filtering the raw gradients instead of median filtering the velocity data. Red line is an arctangent dislocation model with locking depth of 1 km and velocity step of 5 mm/yr, sampled at 100 m resolution. Grey dots are synthetic data with random Gaussian noise at 0.5 mm/yr level added to the red line model. Blue and green dots are grey dots after median and mean filtering, respectively, at 1 km interval and with a 20 km wide filter window. Bar plots show numerically evaluated velocity gradients of the synthetic model (red), synthetic velocity data (grey), at 100 m resolution, and of the median (blue) and mean (green) filtered velocity data at 1 km resolution, labeled with summed bar areas in mm/yr. Blue and green lines are the best-fit velocity profiles and gradient profiles (derivative of arctangent), labeled with inverted velocity (v in mm/yr) and locking depth (l in km).

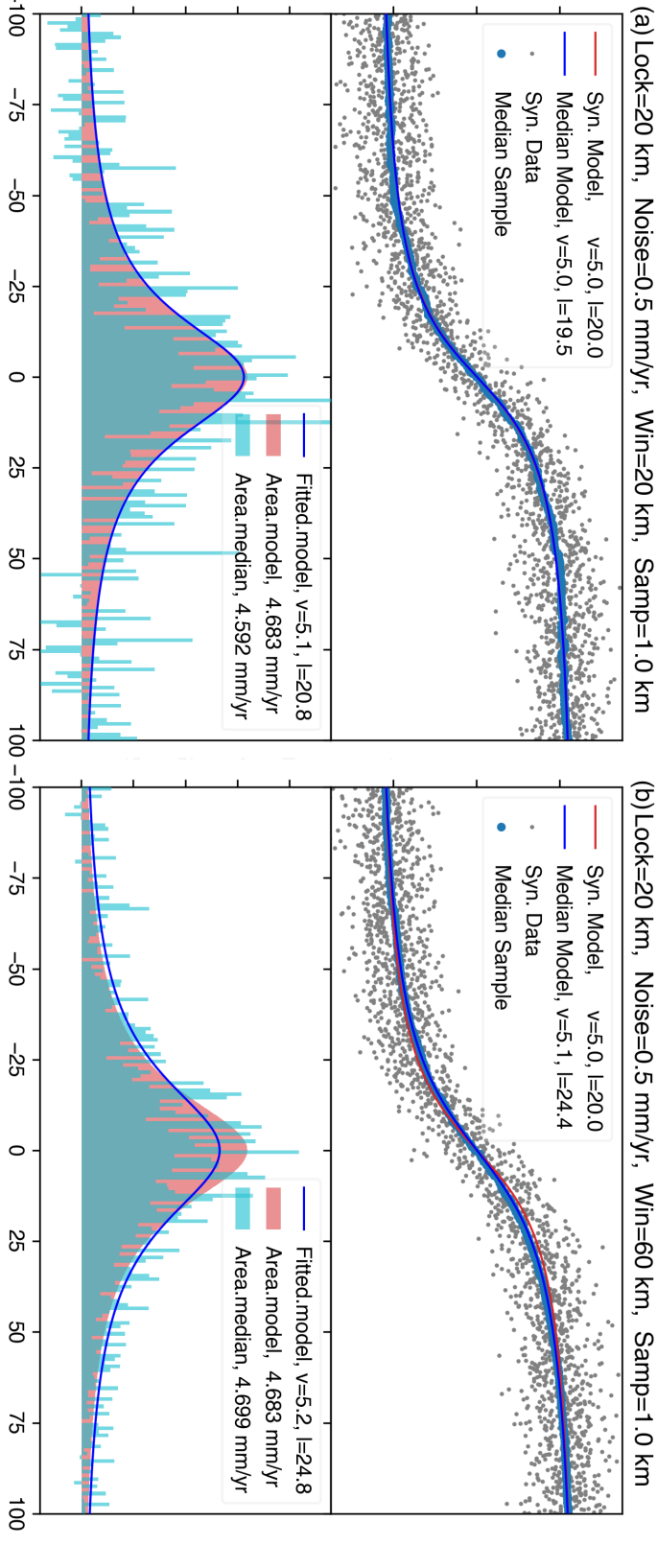

Figure S15. Applying median filters of (a) 20 km and (b) 60 km window sizes to a 200 km-long velocity profile with 20 km fault locking depth, with the same velocity step and noise level as in Fig S14. The longer wavelength of the velocity profile reduces the amplitude, hence the signal-to-noise ratio, of the velocity gradient profile. A 20 km median filter is insufficient to remove noise in the velocity gradient. The negative gradients, when squared, will overestimate the maximum shear and second invariant of the strain rates. A 60 km median filter removes most of the negative gradients, hence when squared, gives a fairer representation of the strain rates.

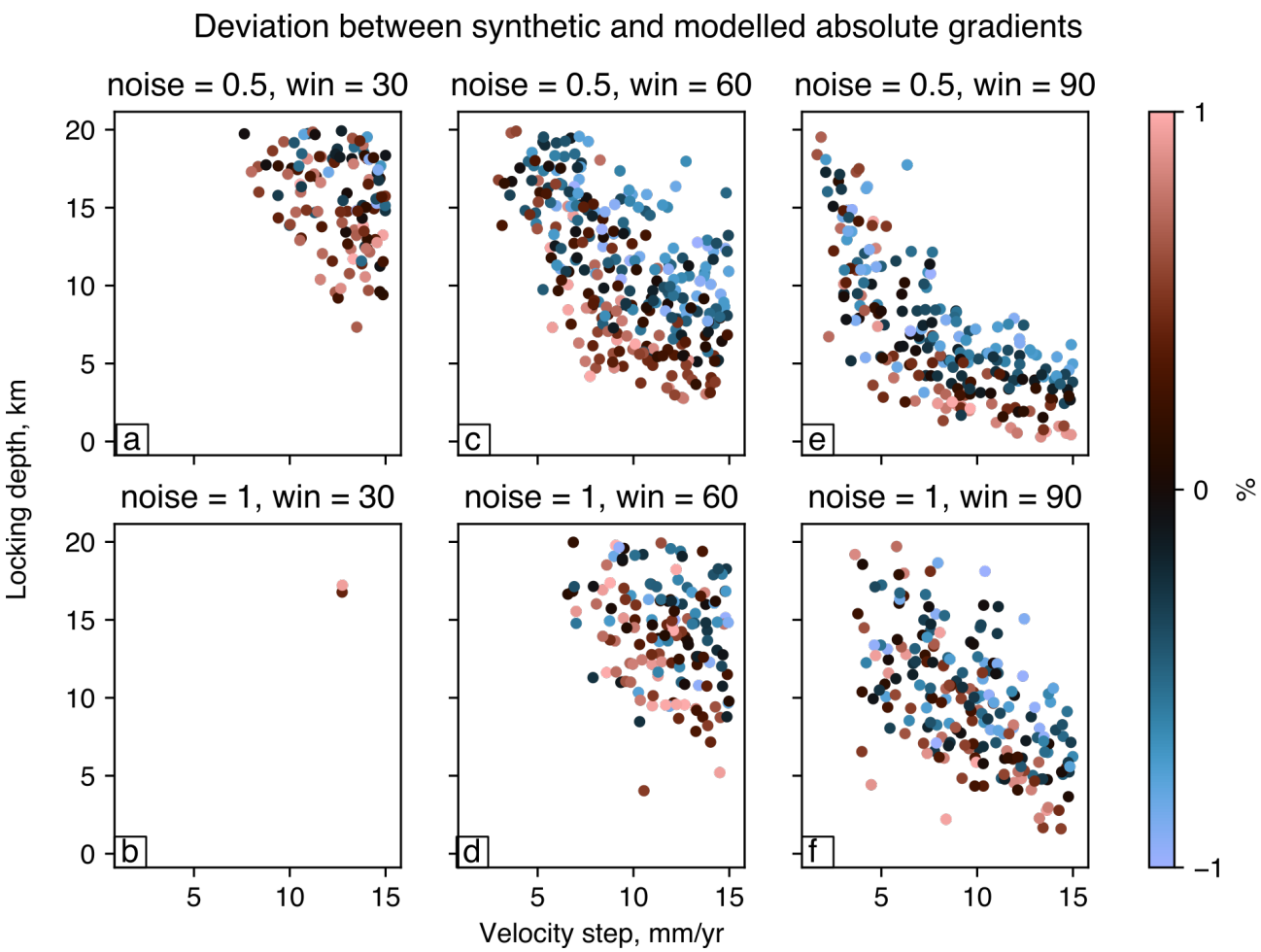

Figure S16. Synthetic tests for the suitability of median filter windows of (a-b) 30 km, (c-d) 60 km and (e-f) 90 km for smoothing synthetic velocity profiles with a range of velocity steps and locking depths simulated with noise levels of (a,c,e) 0.5 mm/yr and (b,d,f)1.0 mm/yr. For each panel, we ran 1000 simulations with random samples of velocity step drawn between 0–15 mm/yr and locking depth drawn between 0-20 km. The scatters only show velocity step and locking depth combinations where the summed absolute velocity gradients (blue bars in Fig S15) deviates from that of the model (red bars in Fig S15) by less than 1%. For typical interseismic locking depths of 13±6 km for Tibet (Wright et al., 2013), the 60 km filter window is suitable for our study region where the Haiyuan Fault is slipping at rates between 4-14 mm/yr (Chen et al., 2022, and references therein) and has InSAR $\sigma(V_E)$ ∼0.5 mm/yr (Fig S10b) and the East Kunlun Fault is slipping at rates between 2-13 mm/yr (Diao et al., 2019, and references therein) and has $\sigma(V_E)$ ∼1 mm/yr (Fig S10b).

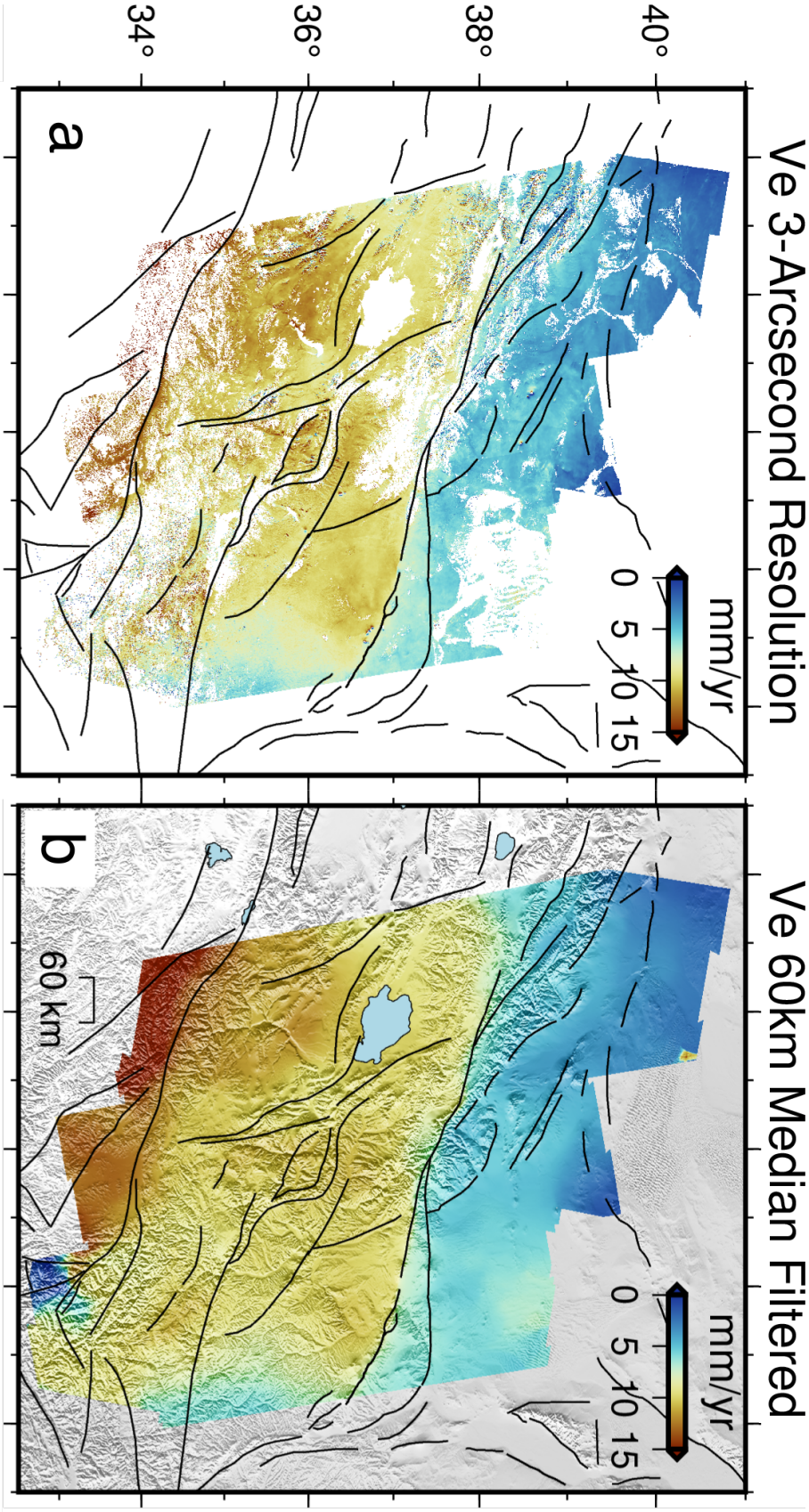

Figure S17. (a) V_E resampled to 3-arcsecond resolution from the original ∼100 resolution provided by the resolution of the LOS velocity maps. (b) Median-filtered V_E with a filter window of 60 km.

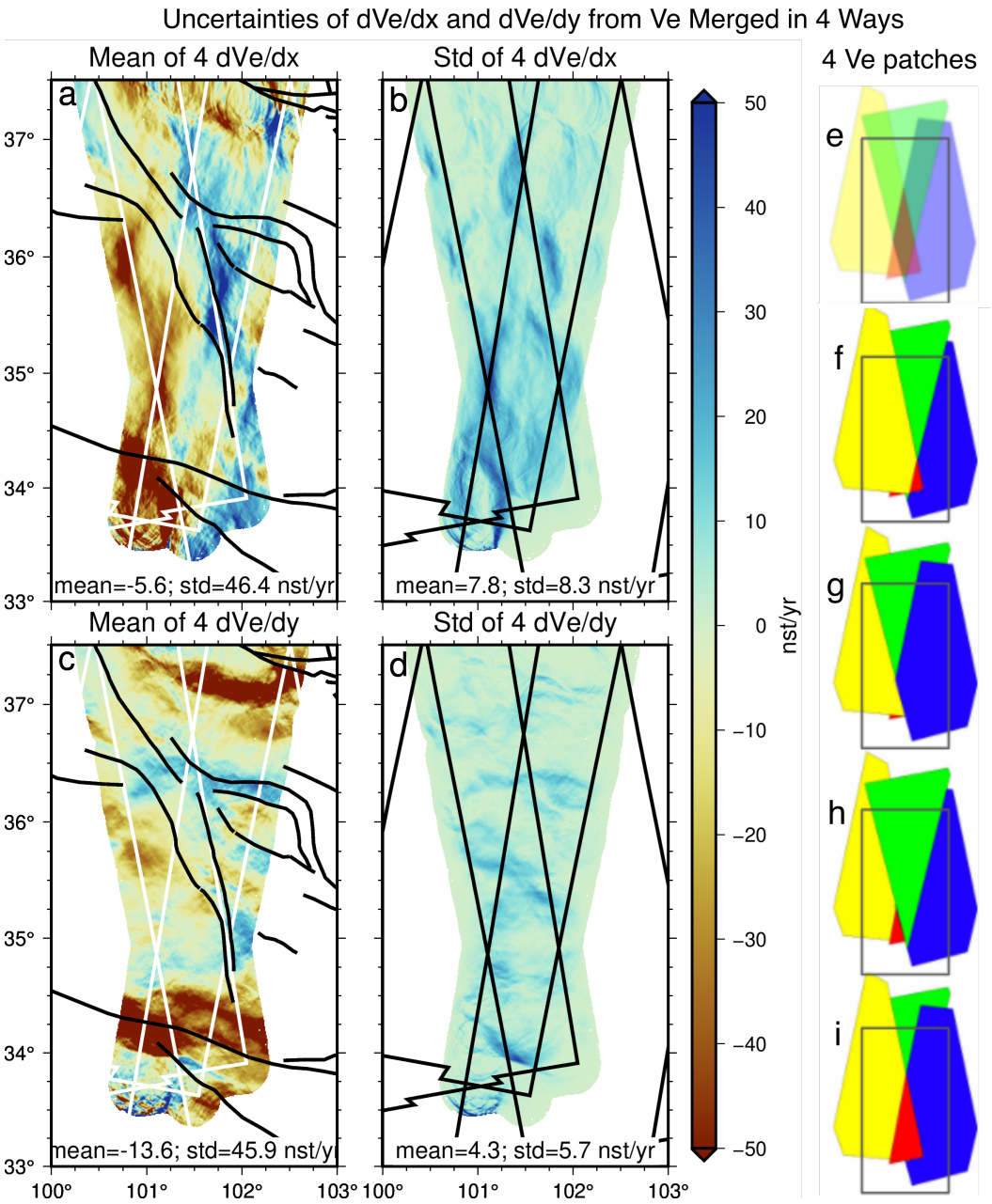

Figure S18. Uncertainties of V_E gradients estimated from four versions of V_E around a region overlapped by two ascending and two descending tracks (026A, 128A, 033D, 135D (Fig 1b,c)). (a, c) Averages of 4 V_E gradients, with faults in black and track boundaries in white. (b, d) Standard deviations of 4 V_E gradients with track boundaries in black. (a-d) only show pixels with changing V_E gradients. We first derived (e) four V_E patches of polygonal shape (yellow, red, green and blue), each obtained through $V_E - V_{UN}$ decomposition from one of the ascending and one of the descending tracks. We then produced four versions of merged V_E by stacking the four V_E patches in four different orders (f-i) which are then filtered before spatial gradients are taken. The grey boxes in (e-i) indicate the plotting region in (a-d).

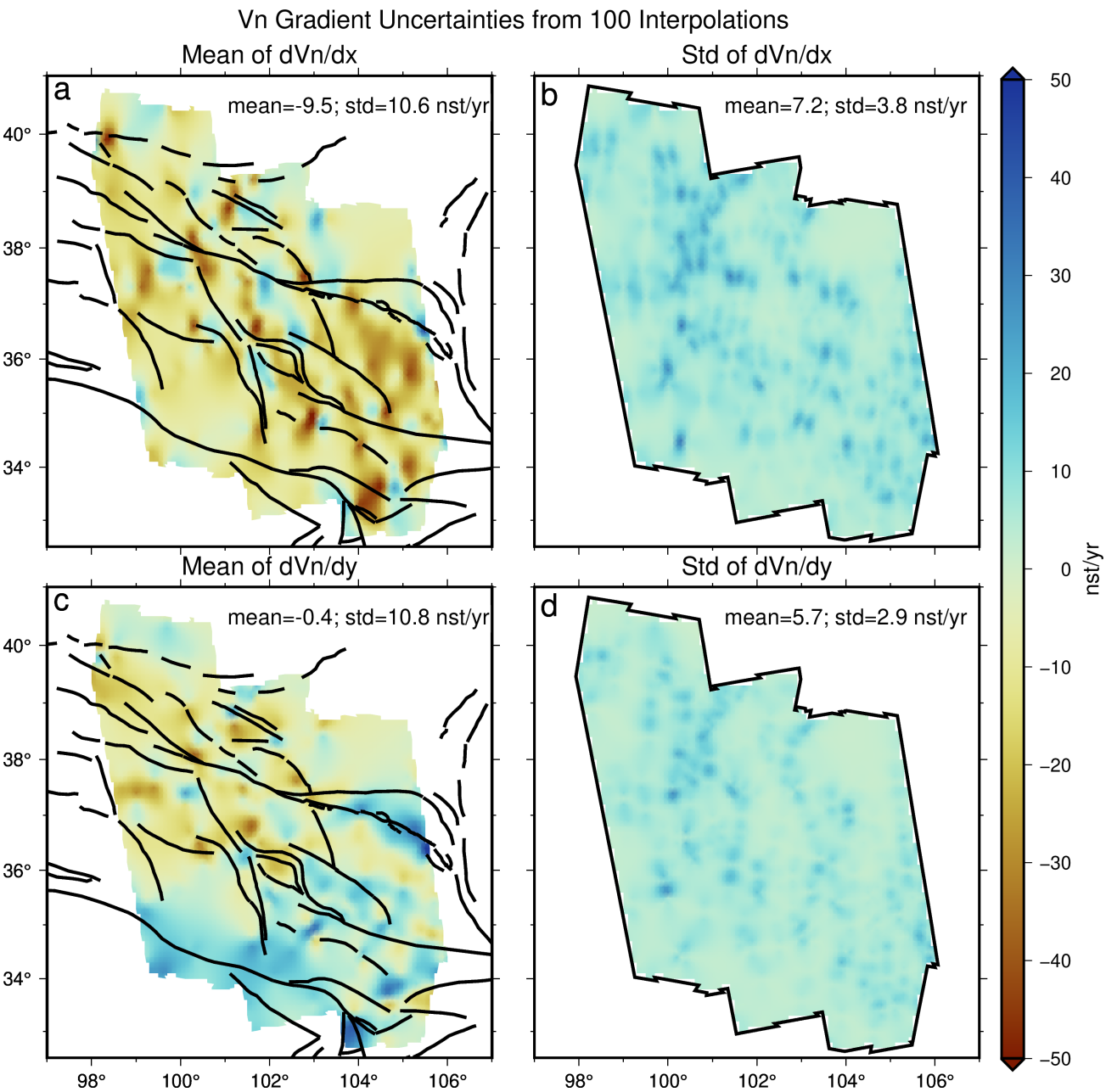

Figure S19. Uncertainties of V_N gradients estimated by interpolating 100 versions of GNSS V_N data sets generated using the Monte Carlo method, each time each GNSS V_N is perturbed by an amount randomly sampled from a Gaussian distribution with its associated σV_N. (a, c) Average of four V_N gradients, with faults in black. (b, d) Standard deviation of four V_N gradients. Pixel statistics labelled in (a-d) are based on pixels within the InSAR data coverage.

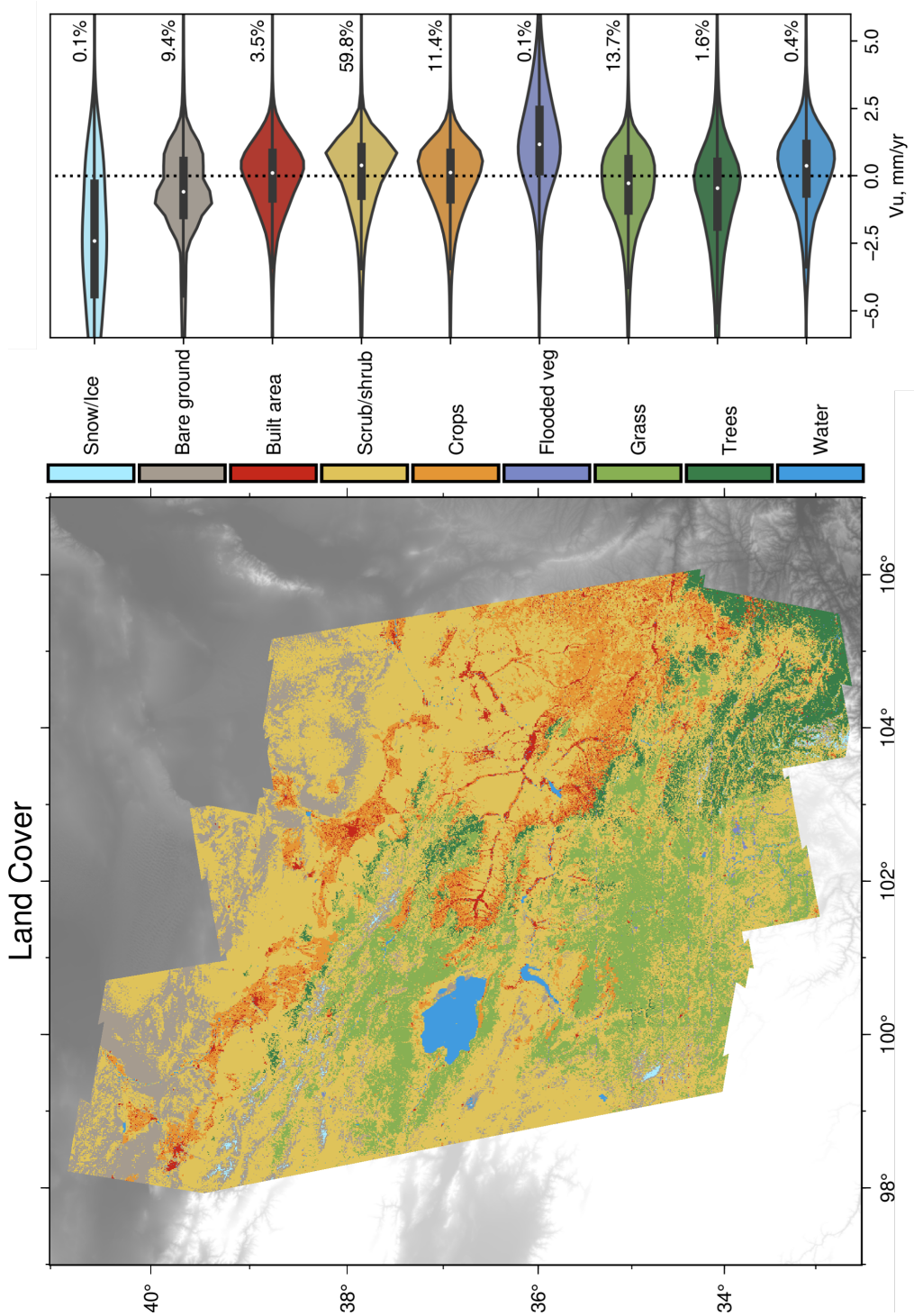

Figure S20. Map of ESRI's global land cover classification (Karra et al., 2021) over the study region, with violin plots between V_U and land cover showing a strong dependency of V_U with water-related land covers (Snow/Ice, Flooded vegetation and Water). The violin-shaped plots on the right show normalised probability density functions of V_U values in each land cover class. The black bars at the center of each violin show the 25-75% range of each distribution and the white dots indicate the median values. Percentage labels at the end of each violin plot show the proportions of V_U pixels of each class in all V_U pixels. SAR signals decorrelate over water surfaces, so most water pixels with V_U measurements are along river and lake banks.